

Multimode fiber optical imaging using wavefront control

THÈSE N° 7572 (2017)

PRÉSENTÉE LE 10 MARS 2017

À LA FACULTÉ DES SCIENCES ET TECHNIQUES DE L'INGÉNIEUR

LABORATOIRE D'OPTIQUE

PROGRAMME DOCTORAL EN PHOTONIQUE

ÉCOLE POLYTECHNIQUE FÉDÉRALE DE LAUSANNE

POUR L'OBTENTION DU GRADE DE DOCTEUR ÈS SCIENCES

PAR

Nicolino STASIO

acceptée sur proposition du jury:

Prof. L. Thévenaz, président du jury

Prof. D. Psaltis, directeur de thèse

Prof. E. Bossy, rapporteur

Prof. P. Ferraro, rapporteur

Prof. C. Moser, rapporteur



ÉCOLE POLYTECHNIQUE
FÉDÉRALE DE LAUSANNE

Suisse
2017

“Omnia vincit Amor”

Virgilio, Bucoliche X, 69

Acknowledgements

First of all, I would like to express my gratitude to my advisor Professor Demetri Psaltis, for giving me the great chance to do research in his laboratory in these past four years. Thank you for the passion, the support, the ideas, the insights and for believing I could complete this PhD thesis from the beginning.

I would like to thank the members of my thesis committee, Prof. Emmanuel Bossy, Prof. Pietro Ferraro, Prof. Christophe Moser and Prof. Luc Thévenaz for their time spent reading this thesis and for being part of the examination jury.

If I went through a PhD is also thanks to people that showed me that research is mainly about passion and is not just a regular job. Thanks to my previous advisors and mentors, because I have not forgotten where I came from: Prof. Domenico Caputo, Prof. Giampiero De Cesare, Prof. Daniela Iacoviello, Prof. Rita Asquini, Prof. Cesare Umeton, Prof. João Pedro Conde, Dr. Virginia Chu.

A big thanks goes to Prof. Emmanuel Bossy and Prof. Christophe Moser for all the ideas and suggestions they shared with me in these years.

Thank you to all the present and former members of the Laboratory of Optics, Ye Pu, Marcin Zielinski, Jae-Woo Choi, Julien Cuennet, Alexandre Goy, Jacob Staley, Fauzia Albertin, Xin Yang, Wuzhou Song, Thomas Lanvin, Marilisa Romito, Morteza Shoreh, Eirini Kakkava, Alexandre Burnand, Pooria Hadikhani, JooWon Lim and Giulia Panusa.

Thank you to Carole Berthet, who with her patience, efficiency, help and smile makes our everyday life much easier.

Thank you to all present and former members of the Laboratory of Applied Photonics Devices, it was a pleasure to have you as neighbors.

Thank you to Atsushi Shibukawa and Olivier Simandoux for the help with the photoacoustic experiment, Donald Conkey for the help with the two-photon imaging experiment (the image in Figure 5.6 was taken almost at 2 am, just to give an idea) and Gregoire Laporte for the SAX microscopy experiments. It was great to work with you.

Special thanks to Ioannis Papadopoulos, for his help since the first day, Salma Farahi for being Salma Farahi, Gregoire “Greg” Laporte for the time spent in and outside the lab, Mohammad Hashemi for the long talks, Miguel Modestino for showing me what a wedding in Venezuela looks like and that his Italian genes are still there. Thank you to the rest of the EPFL-Venezuelan crew, Claudia, the bride, Volker, Zahra, Manon, Clement and Cornelis.

Thank you to my two “step-laboratories”, LBNC and LANES, that adopted me in these years ... thanks to Dasha and Jacopo, Zoe and Adriano, Matt, Henrike, Francesco and Amanda, Ekaterina, Ivan, Nadanai, Kolyo, Dmitry, Dumitru, Saj, Simone ... all my gratitude to all the people that managed to make EPFL and Lausanne a better place. I’ve met so many people in these years that it would take too long to put all the names one after the other.

Thank you to the Vaghissimi Amici e ½.

I would like to thank my parents, Pasquale and Rosaria, my brother Marco, Mauro, Donatella and Claudia for their unconditional support throughout my life, *grazie*.

Finally, a huge thank you goes to Francesca, for being with me in the last nine years and still being with me even after these four years of PhD (©), thank you for your support and love, for the time we spent and the time we are going to spend together.

Lausanne, 14 February 2017

N.S.

Abstract

Optical microscopy enables us to observe at high resolution and with a large field of view objects otherwise invisible for the naked eye. This is why it is becoming a fundamental tool in biology and in diagnostics, where observation at cellular level can tell about the health status of a tissue. At visible wavelengths, light undergoes scattering when propagating through tissues, limiting the imaging depth to the first cellular layers of a biological sample. Endoscopic approaches allow the bypass of the scattering layers and move the accessible volume centimeters inside tissues, ideally keeping large field of view and high-resolution capabilities.

In this thesis we explore the combination of wavefront control and ultrathin multimode optical fibers to develop a new family of endoscopes able to generate images with micrometric resolution being, at the same time, minimally invasive. We demonstrate that a variety of imaging techniques can be implemented in optical fiber-based endoscopy, maximizing the amount of information that can be collected through a few hundreds of micrometers-thick probe.

Firstly, we describe digital phase conjugation (DPC), which is the utilized wavefront shaping technique to convert a multimode optical fiber in an ultrathin endoscope. The use of DPC in synergy with multimode optical fibers resulted in ultrathin probes able to perform fluorescence imaging, photoacoustic imaging, and multiphoton imaging. Moreover, we show that using saturation excitation of fluorescent samples we can beat the resolution limit imposed by the numerical aperture of the optical fiber and obtain optical sectioning. In the first part of the thesis we describe which steps have been performed towards the implementation of these techniques.

In the second part, we exploit coherent fiber bundles as imaging probes. This kind of fiber is typically utilized in endoscopy, but their resolution is limited by the distance between the fiber's cores. Here we show two techniques - one based on DPC and a second based on statistical properties of speckle patterns - to obtain images with a better resolution than the one imposed by the core-to-core spacing, both relying on a unique property of

multicore fibers: the memory effect. We also accomplished complex pattern transmission through multicore fibers with high resolution.

Overall, the presented work provides new insights in imaging through optical fibers based on wavefront shaping techniques, opening up pathways for addressing current issues in this research field.

Keywords: Endoscopy, Digital Phase Conjugation, Fiber imaging, Multimode fibers, Multicore fibers, Capillary waveguides, Photoacoustic imaging, Two-photon imaging, Fluorescence imaging, Saturated excitation microscopy.

Riassunto

La microscopia ottica permette di osservare ad alta risoluzione e con un campo di vista esteso oggetti altrimenti invisibili a occhio nudo. Per questa ragione sta diventando sempre più uno strumento di fondamentale importanza in biologia e in diagnostica, dove osservazioni a livello cellulare permettono di determinare lo stato di salute di un tessuto. Nello spettro del visibile la luce, propagandosi attraverso tessuti biologici, viene diffusa limitando così la profondità di *imaging* ai primi strati del campione biologico. L'endoscopia permette di bypassare gli strati di tessuto e andare a investigare otticamente un volume posto diversi centimetri all'interno di tessuti biologici preservando alta risoluzione e campo di vista.

In questa tesi verrà indagata la combinazione di modulazione di fronti d'onda (*wavefront shaping*) e di fibre ottiche multimodali ultrasottili al fine di ottenere una nuova famiglia di endoscopi minimamente invasivi in grado di generare immagini ad altissima risoluzione .

Verrà dimostrata che questa modalità di imaging attraverso fibre ottiche multimodali è compatibile con una grande varietà di tecniche di microscopia permettendo di massimizzare la quantità di informazioni acquisite attraverso una sonda spesso poche centinaia di micrometri.

Inizialmente verrà descritta la tecnica di wavefront shaping utilizzata: la coniugazione di fase digitale (DPC). La combinazione di DPC e fibre ottiche ha permesso di sviluppare sonde ultrasottili in grado di eseguire imaging a fluorescenza, a fotoacustica e a due fotoni. Verrà dimostrato inoltre come la saturazione della fluorescenza in campioni visualizzati attraverso la nostra sonda endoscopica ha permesso di ottenere una risoluzione migliore rispetto a quella dettata dall'apertura numerica delle fibre ottiche utilizzate. Nella prima parte della tesi verranno discussi i passi necessari all'implementazione di queste tecniche di microscopia attraverso fibre ottiche multimodali ultrasottili.

Nella seconda parte della tesi verrà analizzato l'uso di fibre ottiche costituite da nuclei (*core*) multipli come sonde endoscopiche . Questo tipo di fibre ottiche è comunemente utilizzato in endoscopia ma la loro risoluzione è limitata dalla distanza che intercorre tra un

core e un altro. Verranno mostrate due tecniche - una basata su DPC e una seconda basata sulle proprietà statistiche degli *speckle pattern* - in grado di eseguire imaging con una risoluzione superiore a quella dettata distanza tra i core. Entrambe queste tecniche si basano su una proprietà presente nelle fibre ottiche a core multipli: l'effetto di memoria. Verrà dimostrato inoltre, che attraverso queste fibre è possibile trasmettere pattern ad alta risoluzione.

Nel complesso, il lavoro presentato in questa tesi fornisce nuove conoscenze su endoscopia basata su wavefront shaping e suggerisce nuove metodologie atte a risolvere alcuni dei problemi presenti in quest'ambito di ricerca.

Parole chiave: Endoscopia, Coniugazione Digitale di Fase, Imaging a fibra ottica, Fibre ottiche multimodali, Fibre ottiche multicore, Fibre ottiche capillari, Imaging a fotoacustica, Imaging a due fotoni, Imaging a fluorescenza, Microscopia a eccitazione saturata.

Résumé

La microscopie optique permet l'observation d'objets invisibles à l'œil nu, en haute résolution et avec un large champ de vision. C'est la raison pour laquelle elle est devenue un outil essentiel dans les domaines de la recherche en biologie et des diagnostics, où l'observation au niveau cellulaire fournit de nombreuses informations sur l'état de santé d'un tissu biologique ou d'un patient. Dans les longueurs d'ondes du visible, la lumière est sujette à la diffusion lorsqu'elle se propage dans des tissus biologiques, ce qui limite la profondeur à laquelle l'imagerie est possible aux couches cellulaires les plus superficielles d'un échantillon biologique. Les approches endoscopiques permettent de contourner cette limitation et d'atteindre des volumes à imager plusieurs centimètres sous la surface, tout en gardant, dans l'idéal, les bénéfices de haute résolution et de large champ de vision.

Dans la présente thèse, nous explorons l'utilisation combinée de la modulation de front d'onde et de fibres optiques multimodes ultrafines afin de développer une nouvelle famille d'endoscopes à même de générer des images avec une résolution micrométrique, tout en restant peu invasifs. Nous démontrons qu'une variété de techniques d'imagerie peut être implémentée dans des endoscopes basés sur des fibres optiques, maximisant la quantité d'information obtenue au travers d'une sonde de quelques micromètres de diamètre.

Premièrement, nous décrivons la conjugaison de phase numérique (DPC), qui est la méthode de modulation de front d'onde utilisée afin de convertir une fibre multimode en endoscope. L'utilisation de DPC en synergie avec des fibres multimodes aboutie à la création de sondes ultrafines pouvant servir en imagerie par fluorescence, imagerie acoustique, ou imagerie multi-photons. De plus, nous démontrons que la saturation d'excitation d'échantillons fluorescents permet de dépasser les limites de résolution imposées par l'ouverture numérique d'une fibre optique et d'obtenir un sectionnement optique. Dans la première partie de cette thèse nous décrivons quelles étapes doivent être réalisées afin de mener à bien l'implémentation de ces techniques.

Dans la seconde partie, nous utilisons des faisceaux de fibres cohérents comme sondes d'imagerie. Ce type de fibres est régulièrement utilisé en endoscopie, mais leur résolution est

limitée par la distance entre les cœurs de la fibre. Nous démontrons ici deux techniques – la première basée sur la DPC, la seconde sur les propriétés statistiques de la granularité laser – afin d’obtenir des images avec une meilleure résolution que celle imposée par la distance entre les cœurs, dépendant toutes deux d’une propriété unique des fibres multi-cœurs : l’effet de mémoire. Nous réalisons aussi la transmission de motifs complexes au travers de fibre multi-cœurs avec une haute résolution.

Pris dans son ensemble, le travail décrit dans cette thèse présente de nouvelles approches relatives à l’imagerie au travers de fibres optiques basées sur la modulation de front d’onde, ouvrant la voie vers de nouvelles solutions dans ce domaine.

Mots-clefs: Endoscopie, Conjugaison de phase numérique, Imagerie par fibre, Fibres multimodes, Fibres multi-cœurs, Guides d’onde capillaires, Imagerie photo-acoustique, Imagerie deux-photons, Imagerie par fluorescence, Microscopie par saturation d’excitation.

Contents

Chapter 1 - Introduction	1
1.1 - Imaging in complex media	2
1.2 - Imaging through optical fibers using wavefront shaping	3
1.3 - Summary of the thesis.....	5
Chapter 2 - Guided propagation in optical fibers and digital phase conjugation	11
2.1 - Light propagation in optical fibers.....	11
2.2 - Modes in optical fibers	13
2.3 - Imaging with multimode waveguides	15
2.4 - Optical phase conjugation and Digital phase conjugation	17
2.5 - Digital hologram reconstruction and DPC implementation	22
2.6 - DPC of ultrashort pulses	25
2.7 - DPC through different multimode waveguides	28
Chapter 3 - Fluorescence and optical-resolution photoacoustic imaging through capillary waveguides using digital phase conjugation	33
3.1 - Introduction.....	34
3.2 - Materials and methods	35
3.2.1 - Digital phase conjugation through capillary waveguide characterization.....	39
3.3 - Results and Discussion	42
3.3.1 - Fluorescence imaging	42
3.3.2 - Photoacoustic imaging.....	44
3.4 - Conclusions	47
Chapter 4 - Enhanced resolution in a multimode fiber imaging system	51
4.1 - Introduction.....	51
4.2 - Working principle	52
4.3 - Experimental setup	55

4.4 - Results	57
4.5 - Conclusions	60
Chapter 5 - Lensless two-photon imaging through a multicore fiber with coherence-gated digital phase conjugation	65
5.1 - Introduction	66
5.2 - Coherence-gated digital phase conjugation	67
5.3 - Characterization of DPC focused ultrashort pulses	70
5.3.1 - Focal spot contrast and size	70
5.3.2 - Modal contribution to focus spot	71
5.3.3 - Pulse length	72
5.4 - Digital scanning and field of view	72
5.5 - Two-photon imaging	74
5.6 - Conclusions	76
Chapter 6 - Light control in a multicore fiber using the memory effect	81
6.1 - Introduction	82
6.2 - Experimental setup	83
6.3 - Digital phase conjugation focus characterization	84
6.4 - Using the memory effect in a multicore fiber	85
6.4.1 - Transverse scanning with the MCF	85
6.4.2 - Axial scanning with MCF	88
6.4.3 - No coupling scan range	89
6.4.4 - Scanning limitations imposed by core-to-core coupling	90
6.5 - Single calibration pattern projection	92
6.5.1 - Pattern projection encoding amplitude and phase on the SLM: Gerchberg-Saxton algorithm	98
6.5.2 - Pattern projection encoding amplitude and phase on the SLM: J.A. Davis encoding	100
6.6 - Focus spot preservation in a bent fiber	103
6.7 - Conclusions	104
Chapter 7 - Calibration-free imaging through a multicore fiber using speckle scanning microscopy	109
7.1 - Introduction	109
7.2 - Working principle	110
7.3 - Speckle Scanning Microscopy in MCFs	112
7.4 - Experimental results	114
7.5 - Conclusions	118
Chapter 8 - Conclusions and outlook	121
Curriculum vitae	127

List of figures

Figure 1.1: Blurred vision.....	2
Figure 1.2: Optical fiber-based endoscopy.....	4
Figure 2.1: Step-index optical fiber.....	12
Figure 2.2: Numerical computation of modes in step-index fiber.....	15
Figure 2.3: Light propagation in multimode fibers.....	16
Figure 2.4: Optical Phase conjugation.....	21
Figure 2.5: Optical phase conjugation using holography.....	21
Figure 2.6: Simplified digital phase conjugation setup.....	22
Figure 2.7: Digital hologram of the output of a multimode fiber.....	24
Figure 2.8: Digital phase conjugation of ultrashort pulses.....	28
Figure 2.9: Comparison between different kinds of optical fibers.....	29
Figure 3.1: Capillary waveguides.....	36
Figure 3.2: Experimental optical setup for endoscopy through capillary waveguides.....	38
Figure 3.3: Experimental setup for photoacoustic imaging.....	39
Figure 3.4: Digital phase conjugation through capillary waveguides.....	41
Figure 3.5: Digital phase conjugation through capillary waveguides: simulation.....	42
Figure 3.6: Demonstration of high-resolution fluorescence imaging through capillary waveguides.....	43
Figure 3.7: Collection efficiency of the capillary waveguide as a function of the working distance.....	44
Figure 3.8: Phase conjugated spot size in water as a function of the working distance.....	45
Figure 3.9: Characterization of photoacoustic signal collection using the capillary waveguide.....	46
Figure 3.10: Optical resolution photoacoustic imaging through capillary waveguides.....	47

Figure 4.1: Resolution improvement and optical sectioning in saturated excitation microscopy	54
Figure 4.2: Edge responses for a 0.39 NA scanning imaging system	55
Figure 4.3: Schematic of the imaging setup for saturated excitation endoscopy	56
Figure 4.4: Demodulated fluorescence signal intensity from nanodiamonds	58
Figure 4.5: Point spread function narrowing with saturated excitation endoscopy	58
Figure 4.6: Fluorescence images of nanodiamonds immobilized on a glass slide	59
Figure 4.7: Sectioning properties of saturated excitation microscopy	60
Figure 5.1: The optical apparatus for coherence-gated digital phase conjugation with a multicore fiber	69
Figure 5.2: The temporal profile of the total power of the coherence-gated output from the multicore fiber	70
Figure 5.3: Phase conjugated beam through multicore fiber	71
Figure 5.4: Temporal profile of the phase conjugated beam through multicore fiber	72
Figure 5.5: Intensity of phase conjugated beam as function of position: simulation and experiment	74
Figure 5.6: Two-photon fluorescent image of 1 μm polystyrene beads stained with Rhodamine 6G dispersed in PDMS	75
Figure 5.7: Two-photon images of stained cells through multicore fiber	76
Figure 6.1: Experimental optical setup	83
Figure 6.2: Digital phase conjugated focus spot characterization	85
Figure 6.3: Digital scanning of the focus spot using a single calibration hologram	86
Figure 6.4: Memory effect in multicore fibers: mode dependence	87
Figure 6.5: Imaging using digital phase conjugation in combination with memory effect ...	88
Figure 6.6: Axial shifting of the digital phase conjugated focus spot using a single calibration hologram	89
Figure 6.7: Focusing through a waveguide array in no-coupling and coupling conditions ...	91
Figure 6.8: Scanning range in a waveguide array using digital phase conjugation: coupling dependence	92
Figure 6.9: Pattern projection using a single calibration hologram	93
Figure 6.10: Beam Propagation Method simulation: focusing using a multicore fiber	94
Figure 6.11: Beam Propagation Method simulation: projection of cross pattern using a multicore fiber (phase only modulation)	95
Figure 6.12: Beam Propagation Method simulation: projection of cross pattern using a multicore fiber (phase and amplitude modulation)	96
Figure 6.13: Beam Propagation Method simulation: projection of a line using a multicore fiber (phase only modulation)	97
Figure 6.14: Beam Propagation Method simulation: projection of a square pattern using a multicore fiber (phase only modulation)	97
Figure 6.15: Multiple spots projection using a multicore fiber	99
Figure 6.16: Pattern projection using a multicore fiber: GS algorithm.	100

Figure 6.17: Amplitude modulation: diffraction efficiency into different orders.	101
Figure 6.18: Pattern projection through a multicore fiber: line projection (amplitude and phase modulation).....	102
Figure 6.19: Pattern projection through a multicore fiber: single characters (amplitude and phase modulation).....	102
Figure 6.20: Pattern projection through a multicore fiber: complex patterns (amplitude and phase modulation).....	103
Figure 6.21: Bending of a multicore fiber during digital phase conjugation	104
Figure 7.1: Experimental optical setup for speckle scanning microscopy through a multicore fiber.....	113
Figure 7.2: Generation of uncorrelated speckles in a multicore fiber for speckle scanning microscopy.....	114
Figure 7.3: Speckle scanning microscopy through a multicore fiber: characterization	115
Figure 7.4: Speckle scanning microscopy imaging through a multicore fiber: 1951 USAF target	116
Figure 7.5: Speckle scanning microscopy imaging through a multicore fiber: 1 μm fluorescent beads deposited on a glass slide	117
Figure 7.6: Speckle scanning microscopy imaging through a multicore fiber: 1 μm fluorescent beads deposited on a glass slide	118

Chapter 1

Introduction

Every day we employ imaging systems, maybe even without realizing it. Reading this thesis, for example, you are utilizing an imaging system: your eyes and, perhaps, a pair of glasses or contact lenses are part of an imaging system that enables vision.

As we know from basic optics, a single lens can perform imaging. A light field propagating in free space between two spatial positions is affected by optical diffraction that can be described by the Helmholtz equation. The optical wave (that we will describe using the term *optical wavefront*) coming from an object of interest undergoes a linear transformation. This transformation can be “undone” using a lens to retrieve the shape of the object (this is exactly what happens with our eyes when we observe an object). This inversion is possible when the propagation happens in free space. In the case that something perturbs the linear transformation, a lens might not be enough to retrieve the shape of the object. This is what happens, for example, when fog or a frosted piece of glass is introduced between an observer and an object.

Figure 1.1 shows a picture taken from a cliff-overlook at Torrey Pines State Reserve in La Jolla, California. In the image we can discriminate three regimes. On the left side of the picture, in the foreground, is a cliff which is completely visible without any loss of information. Behind it, the fog partially covers some cliffs and completely obscures the Pacific Ocean in the background. In the first case the photons have retained their initial trajectory passing through the medium, only air in this case. These photons are known as ballistic photons. In the fog, composed of small water droplets suspended in air, the photons deviate in a non-predictable way. In this case lens-based imaging can provide a blurred image (weak scattering, as in the partially obscured cliffs, behind the foreground) or fails trying to retrieve the image (strong scattering, as in the case of the ocean, far from the viewer).



Figure 1.1: **Blurred vision.** Different scattering regimes can be observed in the picture: on the left side, the image appears to be clear and sharp, thanks to the ballistic photons reaching the camera objective. A weakly scattering regime can be observed at the center of the picture, where the badland are barely visible through the fog. Strong scattering regime can be observed on the right side, where the fog prevents the view of the ocean on the background.

1.1 - Imaging in complex media

The same scenario is also present at an extremely small scale, for example when dealing with biological tissues. Optical imaging is an extremely important tool for diagnostic purposes, but the imaging depth is limited to less than 1 millimeter due to the optical diffusion limit [1]. Just as small water droplets in fog obscured our view of the ocean in Figure 1.1, optical waves in the visible spectrum are scattered by index inhomogeneities in tissues, preventing imaging at a cellular level deep inside tissue.

Recently, many different approaches have been conceived to focus light [2]–[10] and image through scattering media [11]–[15], showing that by shaping dynamically the optical wavefront of the incident beam on a scattering medium, it is possible to control the light transmission through it. For example, in 2007, I. Vellekoop and A. Mosk published a pioneering work [2] that aroused attention by demonstrating the ability of focusing light through extremely complex media, such as paint, egg shells etc. When coherent light propagates through a complex medium, scattering and interference produce a random pattern (a speckle pattern) totally uncorrelated to the input field. Although uncorrelated the speckle pattern still carries information about the input. The authors were able to pre-shape the incident coherent light on the scattering material and focus behind it. In order to construct what they called the “inverse diffusion wavefront,” the authors used a spatial light modulator (SLM), a device that can spatially modify the phase of a laser beam.

If a laser beam (let us assume a plane wave) is sent to the SLM and then redirected towards the turbid layer, if no phase modulation is applied, a speckle pattern is generated behind the scatterer. If we divide the SLM into N segments, the field in a specific point of the speckle pattern, E_m , is a linear combination of the N fields emerging from the segment of the SLM, weighed by the scattering process:

$$E_m = \sum_{n=1}^N t_{mn} A_n e^{j\phi_n}. \quad (1.1)$$

The scattering process can be modeled as a random amplitude and phase, specific for each of the N fields, t_{mn} in the previous equation. The phase of each segment of the SLM is set to a value such that the random phases introduced by the scattering material are compensated, and all N contributions to the field in the specific location behind the scatterer are in phase and constructively interfere to dramatically increase the intensity of that speckle grain.

The authors searched for the best phase for each SLM segments by sequentially assigning phase values ranging from 0 to 2π to one segment and measuring with a camera which phase gave the highest intensity at one specific location, then storing the intensity maximizing phase value. Once the measurement has been accomplished for all the SLM segments, each segment's phase is set to the stored phase value, which yielded a focus spot behind the scattering medium. The amount of light that can be focused in a single spot (the enhancement) depends on the number of segments that are used to modulate the incident field.

Nevertheless, the scattering severely limits the collection of the generated signal (i.e. fluorescence), thus restricting the imaging depth even in case of focusing.

1.2 - Imaging through optical fibers using wavefront shaping

A valid alternative to these techniques is to use optical fiber-based endoscopes, which bypass the scattering tissue and image well beyond the mean free path. An endoscope can be seen as a way to move deep inside the body to access the targeted volume. Desirable features of an endoscope are minimal invasiveness, high resolution and large field of view. Moreover, an ideal endoscope should also be versatile and capable of implementing different imaging techniques.

Fiber-based endoscopes are typically made out of multicore fibers (MCF, or fiber bundles) equipped with a GRIN lens in front. Otherwise, they comprise a single-mode fiber (SMF), a lens, and an actuation system to scan a focused spot. The former approach has its effective resolution limited by the core-to-core distance and pixelation artifacts. The resolution is in general around 3 to 5 μm , unless the MCFs are equipped with lenses in front, which improves the resolution, at the expense of field of view and invasiveness. The latter can have a higher resolution but at the cost of an actuation housing in the millimeter diameter range ([16], [17]).

The possibility of using spatial light modulators (SLMs) together with techniques to focus through scattering materials, opened the path to endoscopy using multimode fibers

(MMFs, [18]–[24]). These kinds of fibers are normally not used in endoscopy even if they can have high numerical aperture and a very limited diameter. A light field entering a MMF, in fact, couples to different modes of the fiber and becomes spatially scrambled during propagation, resulting in a quasi-random intensity pattern (speckle pattern). Considering a MMF as a linear system, it is possible, after a calibration step, to determine which input field will create a given output (this will be described in detail in **Chapter 2**). Light can be shaped using a SLM and sent into the MMF in order to focus and scan light at the distal end of the fiber. Thus, *wavefront shaping* can turn a MMF into a focusing and scanning lens, which can be used as an ultra-thin and minimally invasive endoscope (Figure 1.2). Focusing through the fiber can be achieved using the same approach described before for scattering media [2]. Over the years several methodologies have been developed.

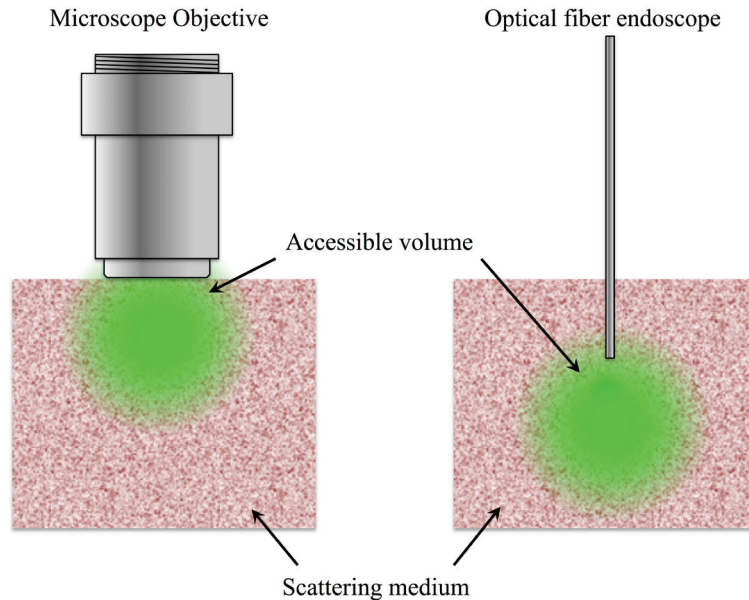


Figure 1.2: **Optical fiber-based endoscopy.** Optical fiber endoscopes are able to move the accessible imaging volume deep inside a scattering medium. Wavefront shaping, at the same time, allows obtaining a minimally invasive footprint attaining, at the same time, high-resolution.

A first wavefront shaping approach in MMFs based on SLMs was proposed by R. Di Leonardo and S. Bianchi in 2011 [18], where a phase only liquid crystal SLM was used to shape the light beam. A direct search algorithm was utilized to find the best phase pattern to focus light in a specific location in front of the MMF facet. The procedure, which in the specific case had a duration of 10 minutes, had to be repeated to focus light in a different location. Other groups implemented iterative algorithms to focus light through multimode fibers ([25], [26]).

The transmission matrix approach [5] was also utilized in order to image through MMFs. In this case the optical system from the SLM to the imaging plane at the tip of the fiber is

considered to be a linear system. Choosing a set of modes as inputs and measuring the corresponding complex fields at the output, the linear system can be characterized. The outputs are linked to the inputs by the transmission matrix, which can be calculated. The inversion of such a matrix allows to calculate the phase pattern able to maximize the intensity on a target location at the output facet of the fiber, focusing light. Once the transmission matrix is known, this technique also allows retrieving a complex input pattern measuring the complex field on the other side of the MMF.

Using transmission matrix approaches fluorescence microscopy was obtained in references [20], [21], [27], dark field microscopy in reference [20] and widefield imaging in [20], [23].

In this thesis, we use as wavefront shaping technique the digital version of Optical Phase Conjugation ([28]–[30]), Digital Phase Conjugation (DPC). The general idea behind this technique is that the photons emerging from the scattering medium can be reversed and propagated backwards to undo the scattering process. This can be done, for example, by holographically recording onto a photographic plate the field coming from an object and passing through a diffuser. Illuminating the hologram with the conjugate of the used reference beam, the conjugate of the field is formed and propagated back exactly through the same path experienced before, reconstructing an image of the object in the original position. This approach can be adapted to perform point-scanning microscopy.

Recording holograms corresponding to fields coming from focused spots behind a scatterer, would allow scanning a light spot behind a turbid medium using Optical Phase Conjugation. In this case, instead of a static hologram, we would need a set of prerecorded holograms and use them sequentially to raster scan a focus spot. This is achieved by implementing the concept of Digital Phase Conjugation ([31], [32]) where digital holograms are recorded using a CCD camera and the conjugate of the calculated is assigned on a SLM.

The same concepts can be used for MMFs. A calibration focus spot is raster scanned in front of the distal side of the MMF and digital holograms of the output fields are recorded at the proximal side. A phase lookup table is calculated and assigned on the SLM, the DPC process undoes the mode coupling and allows for the focusing and scanning of light at the proximal end of the MMF.

Papadopoulos et al., in our group, were able to demonstrate lensless fluorescence microscopy through MMF with no optical sensors, scanners or lenses at the distal end of the fiber during imaging [33]. A first demonstration of optical resolution photoacoustic imaging was demonstrated in [34], this time placing an ultrasound sensor at the distal MMF's end.

1.3 - Summary of the thesis

The high resolution and the reduced footprint come with some drawbacks. First, even if the resolution is high compared to other kinds of endoscopic approaches, the numerical aperture (*NA*) of MMFs usually does not exceed 0.5. This, in principle, places a hard limit on the maximum attainable resolution. Second, this kind of technology does not tolerate conformation changes (i.e. bending) of the fiber between the calibration step and the imaging step. In the case of bending, a new calibration would be needed. This implies the necessity

of access to both sides of the MMF endoscope and the acquisition of a digital hologram for every scanning position.

Starting from these last two statements, the main objective of the thesis is to demonstrate that compared to previous works, image quality can be improved implementing different imaging techniques and improving the attainable resolution. Another objective is to minimize the amount of information required for the calibration step in order to face the bending problem.

After this introductory chapter, **Chapter 2** gives an insight about light propagation through optical waveguides and digital phase conjugation, describing the theoretical basis of the techniques used in the carried out experiments.

In **Chapter 3** we show that optical-resolution photoacoustic and fluorescence imaging are possible through the same optical waveguide, when a capillary waveguide is used. Compared to previous works, this eliminates the need of any optics or sensors at the distal end of the endoscope. The combination of fluorescence and photoacoustic imaging can be very important when complementary information about the sample needs to be collected. We exploited the optical guiding properties of the silica annular core, showing that it is possible to focus and scan a nanosecond pulsed laser using DPC. In the case of fluorescent samples, the emitted light was collected through the silica part. In the case of absorbing samples, the emitted photoacoustic waves were collected using the water-filled core as an acoustic waveguide.

In **Chapter 4** we demonstrate optical sectioning and enhanced resolution in MMF imaging using saturated excitation and temporal modulation [35]. A laser beam is temporally sinusoidally modulated and focused through a MMF on a fluorescent sample. The fluorescent signal collected back through the fiber is a temporal sinusoid with the same frequency ω . By increasing the beam intensity, the fluorescent response saturates, so that the fluorescent signal becomes a saturated sinusoid, which contains harmonics at 2ω , 3ω , etc., depending on the saturation level. It is shown that the n^{th} harmonics is proportional to the n^{th} power of the laser intensity. This nonlinear effect reduced the equivalent point spread function of the imaging system and introduced rejection of out of focus light. The resolution of the MMF imaging system was improved by a factor close to 1.7, beating the hard limit given by the fiber NA .

In **Chapter 5** we show multi-photon imaging through MCFs. Although MCFs usually offer low resolution because of the core-to-core spacing, we demonstrated near diffraction limited two-photon fluorescence imaging through a lensless, commercially available MCF endoscope, by utilizing coherence gated DPC.

Normally, imaging using MCFs is performed by illuminating one core at a time, limiting the resolution to the core-to-core spacing. Here, by illuminating all the cores on the proximal side of the MCF, we generate a random optical field (speckle pattern), at the distal end, with the maximum frequency content given by the NA of the MCF's cores. Focusing of an ultrafast pulse through a MCF with DPC allows for an imaging resolution value better than the MCF core-to-core spacing, limited by the core NA and not by the core spacing. The lensless approach eliminates the increase in size of the endoscope and the reduced field of

view. We construct TPF images by digitally scanning the phase conjugated focus on the target object and collecting the emitted fluorescence through the MCF. We demonstrated images of stained cells and optical sectioning by imaging a 3D distribution of fluorescent beads.

In the **Chapter 6** of the thesis we reduce the amount of information needed during the calibration procedure in order to scan a high-resolution focus spot in a regular grid. We calibrate our system to focus at the center of the field of view, acquiring one single digital hologram and performing DPC. We demonstrate that with this single hologram it is possible to steer the focus spot through a significant scan range, thanks to the memory effect present in this kind of optical fiber. We observed, in fact, that as in thin scattering media, phase gradients are conserved within a certain range when coherent light is propagated through MCFs, resulting in a translational memory effect. This effect is not present in MMFs. This feature enables the use of a single real time feedback mechanism to create a scannable focus spot, which could potentially be steered with high-speed galvanometric mirrors. Another clear advantage of the proposed implementation is that the calibration is extremely fast, since it requires only a single hologram. This presents the possibility of recalibrating the endoscope during bending using a light beacon created by a hologram deposited at the tip of the fiber, as in reference [36]. We also show in the same chapter, that the single hologram is sufficient to project extended high-resolution patterns through the same MCF.

As described before, an SLM can be used to properly shape the light to focus through a MMF or a MCF. Instead, if we send a plane wave in a MMF, this will couple into the modes of the optical fiber and generate a speckle pattern at the output. If the cores of a MCF are too close, we have core-to-core coupling. So if we send a plane wave into a MCF, because of coupling and variations between cores, light will exit each core with a slightly different phase delay. All these light beams will interfere coherently generating again a speckle pattern. Since by tilting the input we can transversally shift the output of the MCF, this speckle pattern can be scanned unchanged in the x and y direction within a certain range thanks to the memory effect. Inspired by the work of Bertolotti and coauthors [11], we demonstrate in **Chapter 7** that, without any calibration, scanning the speckle pattern in x and y , we could obtain images of fluorescent samples with a resolution higher than the core-to-core spacing.

During the years in which we performed this work, many other groups were active in the field of imaging through optical fibers. Published works exploited different imaging techniques such as two-photon imaging through MMFs and MCFs ([37]–[40]), confocal microscopy through MMFs ([41], [42]), studied symmetry properties of the modes in MMFs ([26], [43]), provided better understanding and models of the light propagation in MMFs ([44], [45]), and exploited wavefront shaping through high numerical aperture photonic crystal fibers [46]. Work has also focused in exploiting imaging by using the memory effect in specialty MCFs ([47], [48]).

Bibliography

- [1] V. Ntziachristos, “Going deeper than microscopy: the optical imaging frontier in biology,” *Nat. Methods*, vol. 7, no. 8, pp. 603–614, Aug. 2010.
- [2] I. M. Vellekoop and A. P. Mosk, “Focusing coherent light through opaque strongly scattering media,” *Opt. Lett.*, vol. 32, no. 16, pp. 2309–2311, Aug. 2007.
- [3] Z. Yaqoob, D. Psaltis, M. S. Feld, and C. Yang, “Optical phase conjugation for turbidity suppression in biological samples,” *Nat. Photonics*, vol. 2, no. 2, pp. 110–115, Feb. 2008.
- [4] I. M. Vellekoop, A. Lagendijk, and A. P. Mosk, “Exploiting disorder for perfect focusing,” *Nat. Photonics*, vol. 4, no. 5, pp. 320–322, May 2010.
- [5] S. M. Popoff, G. Lerosey, M. Fink, A. C. Boccarda, and S. Gigan, “Controlling light through optical disordered media: transmission matrix approach,” *New J. Phys.*, vol. 13, no. 12, p. 123021, Dec. 2011.
- [6] X. Xu, H. Liu, and L. V. Wang, “Time-reversed ultrasonically encoded optical focusing into scattering media,” *Nat. Photonics*, vol. 5, no. 3, pp. 154–157, Mar. 2011.
- [7] O. Katz, E. Small, and Y. Silberberg, “Looking around corners and through thin turbid layers in real time with scattered incoherent light,” *Nat. Photonics*, vol. 6, no. 8, pp. 549–553, Aug. 2012.
- [8] K. Si, R. Fiolka, and M. Cui, “Fluorescence imaging beyond the ballistic regime by ultrasound-pulse-guided digital phase conjugation,” *Nat. Photonics*, vol. 6, no. 10, pp. 657–661, Oct. 2012.
- [9] B. Judkewitz, Y. M. Wang, R. Horstmeyer, A. Mathy, and C. Yang, “Speckle-scale focusing in the diffusive regime with time reversal of variance-encoded light (TROVE),” *Nat. Photonics*, vol. 7, no. 4, pp. 300–305, Apr. 2013.
- [10] T. Chaigne, O. Katz, A. C. Boccarda, M. Fink, E. Bossy, and S. Gigan, “Controlling light in scattering media non-invasively using the photoacoustic transmission matrix,” *Nat. Photonics*, vol. 8, no. 1, pp. 58–64, Jan. 2014.
- [11] J. Bertolotti, E. G. van Putten, C. Blum, A. Lagendijk, W. L. Vos, and A. P. Mosk, “Non-invasive imaging through opaque scattering layers,” *Nature*, vol. 491, no. 7423, pp. 232–234, Nov. 2012.
- [12] V. Bianco, M. Paturzo, O. Gennari, A. Finizio, and P. Ferraro, “Imaging through scattering microfluidic channels by digital holography for information recovery in lab on chip,” *Opt. Express*, vol. 21, no. 20, pp. 23985–23996, Oct. 2013.
- [13] M. Locatelli *et al.*, “Imaging live humans through smoke and flames using far-infrared digital holography,” *Opt. Express*, vol. 21, no. 5, pp. 5379–5390, Mar. 2013.
- [14] X. Yang, Y. Pu, and D. Psaltis, “Imaging blood cells through scattering biological tissue using speckle scanning microscopy,” *Opt. Express*, vol. 22, no. 3, p. 3405, Feb. 2014.
- [15] S. Kang *et al.*, “Imaging deep within a scattering medium using collective accumulation of single-scattered waves,” *Nat. Photonics*, vol. 9, no. 4, pp. 253–258, Apr. 2015.
- [16] B. A. Flusberg, E. D. Cocker, W. Piyawattanametha, J. C. Jung, E. L. M. Cheung, and M. J. Schnitzer, “Fiber-optic fluorescence imaging,” *Nat. Methods*, vol. 2, no. 12, pp. 941–950, Dec. 2005.
- [17] G. Oh, E. Chung, and S. H. Yun, “Optical fibers for high-resolution in vivo microendoscopic fluorescence imaging,” *Opt. Fiber Technol.*, vol. 19, no. 6, Part B, pp. 760–771, Dec. 2013.

-
- [18] R. Di Leonardo and S. Bianchi, “Hologram transmission through multi-mode optical fibers,” *Opt. Express*, vol. 19, no. 1, pp. 247–254, Jan. 2011.
- [19] T. Čižmár and K. Dholakia, “Shaping the light transmission through a multimode optical fibre: complex transformation analysis and applications in biophotonics,” *Opt. Express*, vol. 19, no. 20, pp. 18871–18884, Sep. 2011.
- [20] T. Čižmár and K. Dholakia, “Exploiting multimode waveguides for pure fibre-based imaging,” *Nat. Commun.*, vol. 3, p. 1027, Aug. 2012.
- [21] S. Bianchi and R. D. Leonardo, “A multi-mode fiber probe for holographic micromanipulation and microscopy,” *Lab. Chip*, vol. 12, no. 3, pp. 635–639, Jan. 2012.
- [22] I. N. Papadopoulos, S. Farahi, C. Moser, and D. Psaltis, “Focusing and scanning light through a multimode optical fiber using digital phase conjugation,” *Opt. Express*, vol. 20, no. 10, p. 10583, May 2012.
- [23] Y. Choi *et al.*, “Scanner-Free and Wide-Field Endoscopic Imaging by Using a Single Multimode Optical Fiber,” *Phys. Rev. Lett.*, vol. 109, no. 20, p. 203901, Nov. 2012.
- [24] R. N. Mahalati, D. Askarov, J. P. Wilde, and J. M. Kahn, “Adaptive control of input field to achieve desired output intensity profile in multimode fiber with random mode coupling,” *Opt. Express*, vol. 20, no. 13, pp. 14321–14337, Jun. 2012.
- [25] A. M. Caravaca-Aguirre, E. Niv, D. B. Conkey, and R. Piestun, “Real-time resilient focusing through a bending multimode fiber,” *Opt. Express*, vol. 21, no. 10, pp. 12881–12887, May 2013.
- [26] S. Rosen, D. Gilboa, O. Katz, and Y. Silberberg, “Focusing and Scanning through Flexible Multimode Fibers without Access to the Distal End,” *ArXiv150608586 Phys.*, Jun. 2015.
- [27] D. Kim *et al.*, “Toward a miniature endomicroscope: pixelation-free and diffraction-limited imaging through a fiber bundle,” *Opt. Lett.*, vol. 39, no. 7, pp. 1921–1924, Apr. 2014.
- [28] J. W. Goodman, W. H. J. Huntley, D. W. Jackson, and M. Lehmann, “Wavefront-Reconstruction imaging through random media,” *Appl. Phys. Lett.*, vol. 8, no. 12, pp. 311–313, Jun. 1966.
- [29] E. N. Leith and J. Upatnieks, “Holographic Imagery Through Diffusing Media,” *J. Opt. Soc. Am.*, vol. 56, no. 4, pp. 523–523, Apr. 1966.
- [30] H. Kogelnik and K. S. Pennington, “Holographic Imaging Through a Random Medium,” *J. Opt. Soc. Am.*, vol. 58, no. 2, pp. 273–274, Feb. 1968.
- [31] M. Cui and C. Yang, “Implementation of a digital optical phase conjugation system and its application to study the robustness of turbidity suppression by phase conjugation,” *Opt. Express*, vol. 18, no. 4, pp. 3444–3455, Feb. 2010.
- [32] C.-L. Hsieh, Y. Pu, R. Grange, and D. Psaltis, “Digital phase conjugation of second harmonic radiation emitted by nanoparticles in turbid media,” *Opt. Express*, vol. 18, no. 12, pp. 12283–12290, Jun. 2010.
- [33] I. N. Papadopoulos, S. Farahi, C. Moser, and D. Psaltis, “High-resolution, lensless endoscope based on digital scanning through a multimode optical fiber,” *Biomed. Opt. Express*, vol. 4, no. 2, p. 260, Feb. 2013.
- [34] I. N. Papadopoulos *et al.*, “Optical-resolution photoacoustic microscopy by use of a multimode fiber,” *Appl. Phys. Lett.*, vol. 102, no. 21, p. 211106, May 2013.
- [35] K. Fujita, M. Kobayashi, S. Kawano, M. Yamanaka, and S. Kawata, “High-Resolution Confocal Microscopy by Saturated Excitation of Fluorescence,” *Phys. Rev. Lett.*, vol. 99, no. 22, p. 228105, Nov. 2007.

- [36] S. Farahi, D. Ziegler, I. N. Papadopoulos, D. Psaltis, and C. Moser, “Dynamic bending compensation while focusing through a multimode fiber,” *Opt. Express*, vol. 21, no. 19, pp. 22504–22514, Sep. 2013.
- [37] E. R. Andresen, G. Bouwmans, S. Monneret, and H. Rigneault, “Two-photon lensless endoscope,” *Opt. Express*, vol. 21, no. 18, pp. 20713–20721, Sep. 2013.
- [38] E. E. Morales-Delgado, S. Farahi, I. N. Papadopoulos, D. Psaltis, and C. Moser, “Delivery of focused short pulses through a multimode fiber,” *Opt. Express*, vol. 23, no. 7, p. 9109, Apr. 2015.
- [39] E. E. Morales-Delgado, D. Psaltis, and C. Moser, “Two-photon imaging through a multimode fiber,” *Opt. Express*, vol. 23, no. 25, pp. 32158–32170, Dec. 2015.
- [40] S. Sivankutty, E. R. Andresen, R. Cossart, G. Bouwmans, S. Monneret, and H. Rigneault, “Ultra-thin rigid endoscope: two-photon imaging through a graded-index multi-mode fiber,” *Opt. Express*, vol. 24, no. 2, pp. 825–841, Jan. 2016.
- [41] D. Loterie, S. Farahi, I. Papadopoulos, A. Goy, D. Psaltis, and C. Moser, “Digital confocal microscopy through a multimode fiber,” *ArXiv150204172 Phys.*, Feb. 2015.
- [42] D. Loterie, S. A. Goorden, D. Psaltis, and C. Moser, “Confocal microscopy through a multimode fiber using optical correlation,” *Opt. Lett.*, vol. 40, no. 24, pp. 5754–5757, Dec. 2015.
- [43] L. V. Amitonova, A. P. Mosk, and P. W. H. Pinkse, “Rotational memory effect of a multimode fiber,” *Opt. Express*, vol. 23, no. 16, pp. 20569–20575, Aug. 2015.
- [44] M. Plöschner, T. Tyc, and T. Čížmár, “Seeing through chaos in multimode fibres,” *Nat. Photonics*, vol. 9, no. 8, pp. 529–535, Aug. 2015.
- [45] A. Descloux, L. V. Amitonova, and P. W. H. Pinkse, “Aberrations of the point spread function of a multimode fiber due to partial mode excitation,” *Opt. Express*, vol. 24, no. 16, pp. 18501–18512, Aug. 2016.
- [46] L. V. Amitonova *et al.*, “High-resolution wavefront shaping with a photonic crystal fiber for multimode fiber imaging,” *Opt. Lett.*, vol. 41, no. 3, pp. 497–500, Feb. 2016.
- [47] A. Porat, E. R. Andresen, H. Rigneault, D. Oron, S. Gigan, and O. Katz, “Widefield lensless imaging through a fiber bundle via speckle correlations,” *Opt. Express*, vol. 24, no. 15, pp. 16835–16855, Jul. 2016.
- [48] S. Sivankutty *et al.*, “Extended field-of-view in a lensless endoscope using an aperiodic multicore fiber,” *Opt. Lett.*, vol. 41, no. 15, pp. 3531–3534, Aug. 2016.

Chapter 2

Guided propagation in optical fibers and digital phase conjugation

In this chapter we are going to give a brief overview of the theoretical background of light propagation in optical fibers necessary to understand why we need wavefront shaping techniques (digital phase conjugation in our case) to use multimode fibers as imaging elements. We will also recall the basic concepts of digital holography and digital phase conjugation using continuous wave and pulsed lasers. Most of the content of this chapter can be found in references [1]–[4].

2.1 - Light propagation in optical fibers

Optical fibers are made out of a cylindrical dielectric material, usually silica glass, and they include a high refractive index (n_1) core surrounded by a lower refractive index (n_0) cladding (see Figure 2.1). Light is guided with very low losses thanks to total internal reflection (TIR). If, for the sake of simplicity, we consider rays propagating in the optical fiber, the condition of TIR at the core-cladding interface is given by angles θ higher than a critical angle $\theta_c = \arcsin(n_0/n_1)$.

If we call α the angle relative to the fiber axis for a meridional ray, then the maximum angle that a guided ray can have in the core is $\alpha_{MAX} = \pi/2 - \theta_c$. Assuming the fiber is surrounded by air, with refractive index $n_a = 1$, it is possible, applying Snell's law, to calculate its numerical aperture (NA):

$$NA = n_a \sin \theta_a = n_1 \sin \alpha_{MAX} = n_1 \sqrt{1 - \cos^2 \alpha_{MAX}} = n_1 \sqrt{1 - \left(\frac{n_0}{n_1}\right)^2} = \sqrt{n_1^2 - n_0^2}. \quad (2.1)$$

The maximum acceptance angle is therefore:

$$\theta_a = \arcsin\left(\sqrt{n_1^2 - n_0^2}\right). \quad (2.2)$$

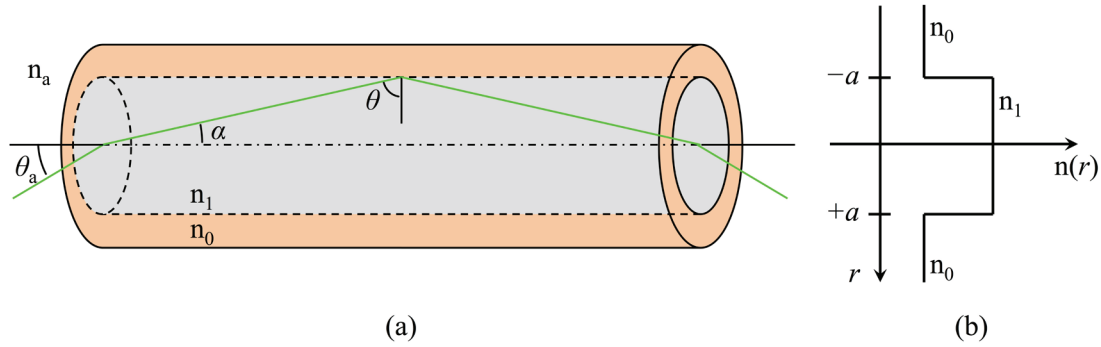


Figure 2.1: **Step-index optical fiber.** (a) An optical fiber is comprised of a high refractive index core and a lower refractive index surrounding cladding. A ray launched in such a fiber will be totally internally reflected if the angle at the core-cladding interface exceeds a critical angle θ_c . (b) Refractive index distribution as a function of the radial direction.

Rays entering the fiber with angles larger than θ_a are partially reflected into the core and refracted into the cladding, resulting in light guiding for only a short distance. The angle θ_a determines the cone of angles such that all the light can be totally internal reflected and guided to the other end of the fiber. Although, even if a ray enters the fiber with an angle less than θ_a , it will not necessarily propagate. Instead, a discrete set of angles is allowed to guide in the optical fiber. It can be shown that the propagation angles have to satisfy a phase matching condition given by [2]:

$$\tan\left(k_0 n_1 a \sin \alpha - \frac{m\pi}{2}\right) = \sqrt{\frac{n_1^2 - n_0^2}{n_1^2} \frac{1}{\sin^2 \alpha} - 1}, \quad (2.3)$$

where $k_0 = 2\pi/\lambda$ is the wavenumber in vacuum and λ is the wavelength of the light source. The equation shows that the propagation angles α that satisfy the phase matching condition are discrete and they depend on the fiber structure (in particular on its radius a , on the core refractive index n_1 and on the relative refractive index between core and cladding). The optical field distributions that satisfy the phase matching condition in equation 2.3, are called *modes*. The mode associated with the angle α calculated for $m=0$ is called the fundamental mode. Modes associated with $m \geq 1$ are called high-order modes. The allowed propagation constant $\beta = k n_1 \cos \alpha$, associated with each propagation angle (and with each mode), is also discrete and is an eigenvalue for the system. The modes are eigenfunctions for the system.

2.2 - Modes in optical fibers

To calculate the optical modes propagating in an optical fiber, an electromagnetic analysis is necessary. We need to solve Maxwell's equations in cylindrical coordinates with appropriate boundary conditions between core and cladding. Let us consider the optical fiber described in Figure 2.1 and let us introduce a reference system where r , ϕ and z are the polar, the azimuthal and the axial coordinate, respectively. The refractive index distribution in a step-index optical fiber can be described as $n(r) = n_1$ for $r \leq a$ (in the core region) and $n(r) = n_0$ for $r > a$ (in the cladding region). For this analysis we assume we are in a weakly guiding fiber, where $n_1 \approx n_0$. Assuming monochromatic light, each component of the electromagnetic field follows the Helmholtz equation, which in cylindrical coordinates is given by:

$$\frac{\partial^2 A}{\partial r^2} + \frac{1}{r} \frac{\partial A}{\partial r} + \frac{1}{r^2} \frac{\partial^2 A}{\partial \phi^2} + \frac{\partial^2 A}{\partial z^2} + n^2 k_0^2 A = 0. \quad (2.4)$$

From Maxwell's equations we know that the electromagnetic scalar field A must be continuous, and so must be its derivative $\partial A / \partial r$. Solutions of equation 2.4 in the core ($r \leq a$) are given by:

$$A(r, \phi, z) = J_l(k_T r) e^{-j l \phi} e^{-j \beta z} \quad \text{with} \quad k_T^2 = n_1^2 k_0^2 - \beta^2, \quad (2.5)$$

where J_l is the Bessel function of first kind and order l , with l being an integer number. The solution in the cladding ($r > a$) is given by:

$$A(r, \phi, z) = K_l(\gamma r) e^{-j l \phi} e^{-j \beta z} \quad \text{with} \quad \gamma^2 = \beta^2 - n_0^2 k_0^2, \quad (2.6)$$

where K_l is the modified Bessel function of the second kind. As explained before, the modes are waves propagating in the fiber with a propagation constant β , this explains the dependence of the form $e^{-j \beta z}$ in the z -direction. The $e^{-j l \phi}$ behavior in the ϕ direction is explained by the fact that the modes are periodic functions in ϕ with period 2π , with l integer number.

The continuity of the field A and its derivative $\partial A / \partial r$ in $r = a$ dictates the choice of the values of k_T and γ . In order to satisfy these two conditions, the following expression must be satisfied:

$$X \frac{J_l'(X)}{J_l(X)} = Y \frac{K_l'(Y)}{K_l(Y)}, \quad (2.7)$$

where $X = k_T a$, $Y = \gamma a$, and the symbol ' indicates the first derivative. Using the properties of the derivative of the Bessel functions [1], the equation can be rewritten as:

$$X \frac{J_{l \pm 1}(X)}{J_l(X)} = \pm Y \frac{K_{l \pm 1}(Y)}{K_l(Y)}. \quad (2.8)$$

It can be observed that if the illumination wavelength and the fiber parameters are known, equation 2.8 has only one unknown variable. In fact:

$$X^2 + Y^2 = a^2 k_T^2 + a^2 \gamma^2 = a^2 (n_1^2 k_0^2 - \beta^2 + \beta^2 - n_0^2 k_0^2) = a^2 k_0^2 (n_1^2 - n_0^2) = V^2, \quad (2.9)$$

where V is called the V parameter and it is a constant that depends on the fiber parameters a, n_1, n_0 and on the wavenumber $k_0 = 2\pi/\lambda$. The V parameter can be rewritten as:

$$V = ak_0 \sqrt{n_1^2 - n_0^2} = a \frac{2\pi}{\lambda} NA. \quad (2.10)$$

Noticing that $Y = \sqrt{V^2 - X^2}$, the only unknown is X , and the equation 2.8, called the *characteristic equation*, can be solved. The solutions of the characteristic equation can be found, for example, graphically, by looking for the intersections of the plot of the left hand side and right hand side of the equation. If we take into consideration only real values for k_T and γ (neglecting evanescent waves), the intersections have to be considered only for $X = k_T a < V$. The roots of the characteristic equation can be used to calculate the values of k_T and γ , which, when substituted into equations 2.5 and 2.6, give the spatial distribution of a fiber mode. For each l we have M_l intersections, identified by m , integer numbers between 1 and M_l . Each pair (l, m) identifies one linearly polarized mode $LP_{l,m}$. Equation 2.8 has to be solved for l varying from 1 to a value l_{MAX} , for which $M_l = 0$. Solving the characteristic equation for $l = 0$, it can be noticed that one solution always exists, for every value of V . This mode is the fundamental mode ($LP_{0,1}$). A second root can be found if the parameter V exceeds the value 2.405. This value is a cut-off parameter such that if exceeded, the optical fiber is multimode (MMF). For values of V below the cut-off, the fiber supports only one mode, and is called single mode fiber (SMF). Figure 2.2 shows the calculated intensity of a few LP modes in a fiber with $V = 60$.

The total number of modes that the step-index fiber can support is strictly related to the fiber characteristics, and in particular to the V parameter. It can be shown that, with good approximation, the number of modes N is given by [1]:

$$N \approx \frac{4}{\pi^2} V^2. \quad (2.11)$$

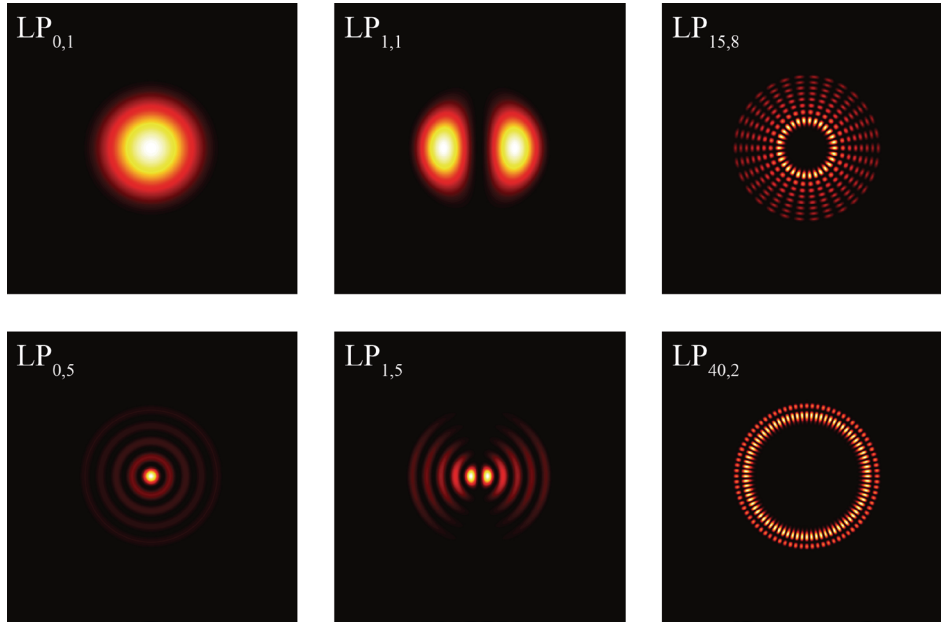


Figure 2.2: Numerical computation of modes in step-index fiber. V parameter used for the calculation is 60. Only the real part of the modes is shown.

2.3 - Imaging with multimode waveguides

As said in the introductory chapter, MMFs are not normally utilized for imaging. They do not act as a relay optical element, which makes their use for focusing and imaging impractical. In fact, an arbitrary optical field $O(r, \phi)$, entering a MMF, couples into multiple supported modes. At the output of the optical fiber, we obtain a scrambled version of the input field $O(r, \phi)$. For simplicity, the expression of the distribution of the n^{th} mode in the core, shown in equation 2.5, can be rewritten as:

$$A_n(r, \phi, z) = J_l(k_{T,n}r) e^{-j\phi} e^{-j\beta_n z} = \Gamma_n(r, \phi) e^{-j\beta_n z}. \quad (2.12)$$

The amount of coupling in each mode depends on the overlap integral between the input field $O(r, \phi)$ and the specific mode. At the entrance of the fiber, the coupling coefficient between the input and the supported n^{th} mode is:

$$\alpha_n(z=0) = \iint O(r, \phi) \Gamma_n^*(r, \phi) dr d\phi, \quad (2.13)$$

where the symbol * at the exponent indicates the complex conjugate. If the fiber is perfect and no coupling is present between modes, the amplitude of each mode remains constant along the whole length of the fiber, so the optical field, at every distance z in the fiber, can be rewritten as a linear combination of the modes weighed by the coupling coefficients:

$$\bar{O}(r, \phi, z) = \sum_{n=1}^N \alpha_n \Gamma_n(r, \phi) e^{-j\beta_n z}. \quad (2.14)$$

Considering an example of commercially available multimode fiber with a 50 μm core, $NA = 0.22$, the refractive indices for the core and the cladding are respectively $n_1 = 1.4607$ and $n_0 = 1.4440$ (Thorlabs, FG050UGA). Assuming an illumination wavelength of 532 nm and knowing that $k_0 n_0 < \beta_n < k_0 n_1$, the phase shift between the mode with the lowest propagation constant and the highest in a 1 cm fiber is of the order of 10^3 radians. This means that for a relatively long fiber, the term $e^{-j\beta_n z}$ in equation 2.14 can be considered as a random phase term. The superposition of the modes multiplied by this random phase term, scrambles the input image into a speckle pattern as the length of the fiber increases. Figure 2.3 shows a simulation of propagation of patterns through a MMF, calculated using the equation 2.14. The scrambling effect due to phase terms is clear after a few hundred micrometers.

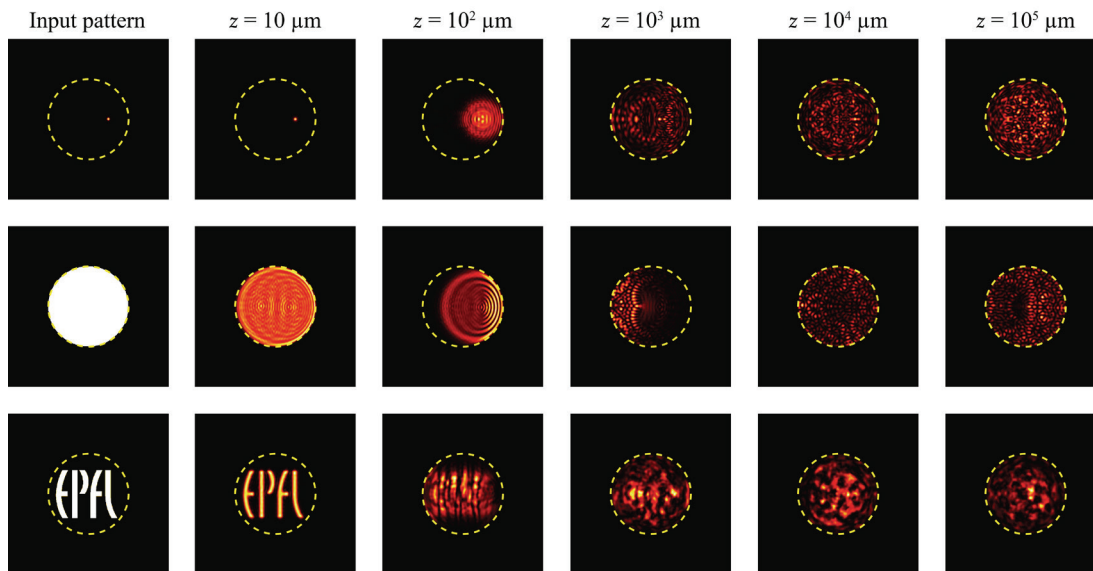


Figure 2.3: **Light propagation in multimode fibers.** Different input patterns are coupled into a MMF. The simulated step-index fiber has $NA = 0.22$, 50 μm core, $n_1=1.4607$ and $n_0=1.4440$. The dashed yellow line shows the position of the fiber. Each column shows the intensity of the field in the MMF at different fiber lengths. The first row shows the propagation of a spot focused at the input facet, positioned off-center. The second row shows the propagation of a plane wave incoming on the fiber facet with an angle along the x-direction. The third row shows the EPFL logo propagating through the same MMF. The illumination wavelength was $\lambda = 532$ nm.

The simulation shown in Figure 2.3 does not take into account coupling between modes, considering the coupling coefficient α_n being constant along the whole length of the optical fiber. In principle, the ability to perfectly model the transmission through an optical fiber would allow imaging through MMFs. As stated before, the output field of the MMF is a linear combination of the supported mode propagating for a given length. Knowing the

length of the fiber, the modes supported by the MMF and their propagation constants, we could retrieve the input of the fiber for a given output.

A better explanation can be given using linear system theory. The modes of the fiber form an orthogonal basis for the fiber, which can be considered, indeed, a linear system. If for each input (mode), the output can be calculated, the transfer function of the linear system can be constructed. At this point an unknown input can be retrieved, knowing the output of the system and the transfer function.

In reality, mechanical deformations of the fiber, surface roughness, bending and temperature variations can be responsible for mode-to-mode coupling and changes in the fiber refractive index, which makes the calculation of the transfer matrix more complex than the calculation of the theoretically supported modes. The ability of directly calculating the transfer matrix is still possible when all these parameters are known with extreme precision [5].

In any case, the transfer matrix of a MMF can be measured, since even when mode-to-mode coupling is present, we are still dealing with a linear system. Techniques developed in the context of imaging and pattern transmission through scattering materials [6]–[8], have been utilized for imaging through multimode fibers. The transmission matrix (TM) of the MMF can be calculated by illuminating the fiber with elements of an orthogonal basis and storing the corresponding output complex fields. Notably, in this case no knowledge of the fiber characteristics are needed, but only the inputs and the associated outputs. Once the TM is known, an input field of the MMF can be reconstructed [9]. At the same time, the TM opens the possibility to control the light field distribution at the output of the MMF using spatial light modulators (SLMs). This can be used for pattern projection or light focusing, opening possibilities in imaging and optical manipulation [10]–[13]. In fact the ability to form and to scan in a regular grid a focused spot, makes MMFs able to operate as a scanning-based imaging system.

In this thesis we used a slightly different approach. The knowledge of the transfer function of a linear system requires as many input-output measurements as the number of modes supported by the linear system. This means that in TM approaches, the ability to project *one* focused spot in *one* specific position relies on the knowledge of the whole transfer function, i.e. a number of input-output measurement equal to the number of modes of the optical fiber. For a lower number of measurements, the system will underperform in terms of focusing efficiency. However, the ability of focusing through a MMF can also be achieved also with *one* single measurement, by using the digital version of optical phase conjugation (D-OPC or DPC).

2.4 - Optical phase conjugation and Digital phase conjugation

The propagation of an electromagnetic field through an inhomogeneous medium, such as a MMF, can be described using the wave equation:

$$\nabla^2 E(x,y,z,t) - \frac{\epsilon(x,y,z)}{\epsilon_0 c^2} \frac{\partial^2 E(x,y,z,t)}{\partial t^2} = 0, \quad (2.15)$$

where $\varepsilon(x, y, z)$ is the permittivity, c is the speed of light and the medium is assumed to be nonmagnetic. A solution of the wave equation can be written as:

$$E(x, y, z, t) = A(x, y, z) e^{-jkz} e^{j\omega t}, \quad (2.16)$$

where $A(x, y, z)$ is the complex amplitude. Plugging this solution into the wave equation we obtain:

$$\nabla_T^2 A(x, y, z) + \frac{\partial^2 A(x, y, z)}{\partial z^2} - 2jk \frac{\partial A(x, y, z)}{\partial z} + \left(\frac{\omega^2 \varepsilon(x, y, z)}{\varepsilon_0 c^2} - k^2 \right) A(x, y, z) = 0, \quad (2.17)$$

where $\nabla_T^2 = (\partial^2/\partial x^2 + \partial^2/\partial y^2)$ is the transverse Laplacian operator. The previous expression, under the paraxial approximation ($|\partial^2 A/\partial z^2| \ll |2jk \partial A/\partial z|$) becomes:

$$\nabla_T^2 A(x, y, z) - 2jk \frac{\partial A(x, y, z)}{\partial z} + \left(\frac{\omega^2 \varepsilon(x, y, z)}{\varepsilon_0 c^2} - k^2 \right) A(x, y, z) = 0. \quad (2.18)$$

The complex conjugate of the last equation is:

$$\nabla_T^2 A^*(x, y, z) + 2jk \frac{\partial A^*(x, y, z)}{\partial z} + \left(\frac{\omega^2 \varepsilon(x, y, z)}{\varepsilon_0 c^2} - k^2 \right) A^*(x, y, z) = 0. \quad (2.19)$$

This means that a field $E_{OPC}(x, y, z, t) = A^*(x, y, z) e^{jkz} e^{j\omega t}$ is also solution of the wave equation. The two optical fields $E(x, y, z, t)$ and $E_{OPC}(x, y, z, t)$ represent a pair of phase conjugated fields, where the respective complex amplitudes are conjugated in the phase factors everywhere in space. Note that this derivation also holds in the non-paraxial case.

One simple example of a phase conjugated wave is the field reflected by a planar mirror when a perfect plane wave is normally incident on it (see Figure 2.4). In this case the plane wave can be expressed as:

$$E(x, y, z, t) = a(x, y, z) e^{-jkz} e^{j\omega t}. \quad (2.20)$$

The mirror in this case, changing the sign of the term e^{-jkz} , actually performs phase conjugation. If the same input plane wave is perturbed before reaching the mirror by an inhomogeneous medium, its flat wavefront gets altered. In this case, since the whole phase factor of the input optical field has to be conjugated, a regular mirror cannot perform optical phase conjugation. Assuming the inhomogeneous medium introduces a phase delay $\psi(x, y, z)$, the field at the output of the disturbing medium can be expressed by

$$E'(x, y, z, t) = a(x, y, z) e^{j[\psi(x, y, z) - kz]} e^{j\omega t}. \quad (2.21)$$

If we neglect diffraction, the wave reflected by a phase conjugating mirror (PCM) will be:

$$E'_{OPC}(x, y, z, t) = a(x, y, z) e^{-j[\psi(x, y, z) - kz]} e^{j\omega t}. \quad (2.22)$$

This wave passes through the same inhomogeneous medium and comes back at the original location as:

$$E''_{OPC}(x, y, z, t) = a(x, y, z) e^{-j[\psi(x, y, z) - kz]} e^{j\psi(x, y, z)} e^{j\omega t} = a(x, y, z) e^{jkz} e^{j\omega t}. \quad (2.23)$$

The last equation represents an ideal plane wave identical to the input one, but propagating in the opposite direction. If a regular mirror replaces the PCM, the distortion $\psi(x, y, z)$ introduced by the inhomogeneous medium does not get canceled, but its effect is doubled. The field in the original position is:

$$E''(x, y, z, t) = a(x, y, z) e^{j[\psi(x, y, z) + kz]} e^{j\psi(x, y, z)} e^{j\omega t} = a(x, y, z) e^{j2\psi(x, y, z)} e^{jkz} e^{j\omega t}. \quad (2.24)$$

We conclude that OPC can be used to cancel out distortions introduced by an inhomogeneous medium, i.e. a multimode optical fiber.

Here we are going to focus on holographic approaches in order to produce phase conjugated waves. The first demonstrations of OPC, in fact, were obtained using holographic plates to record wavefronts of optical fields passing through random media and to phase conjugate [14]–[16]. These experiments, with slight variations among each other, consist in two steps (Figure 2.5). During the first step, a partially transmissive sample is illuminated with a laser beam. The light field first passes through a thin diffuser and then impinges a holographic plate, where a hologram can be recorded by interfering the field with a reference beam. The second step reads-out the hologram using the conjugate of the reference beam used during the recording step. The generated phase conjugated beam travels back through the thin diffuser, compensates for the phase randomization and recreates the exact same input field at the object plane.

The same approach was utilized to project the image of a test pattern through a MMF in 1967 [17], which is, to the best of our knowledge, the first demonstration of OPC in MMFs. From the 1970s OPC has been used in combination with MMFs exploiting four-wave mixing and photorefractive crystals based phase conjugating mirrors [18]–[21].

The development of image sensors, the increase in computational power of computers and the development of spatial light modulators (SLMs), paved the way for the digital implementation of OPC (DPC). DPC was first demonstrated by Yaqoob et al. in tissue in [22] and implemented for turbidity suppression in a scattering medium in [23] and for coherent fiber combining in fiber laser amplifiers [24].

In DPC, the PCM is replaced by the combination of a charge-coupled device (CCD) and a SLM. DPC is implemented in two steps. In a first step, as for OPC, a hologram has to be recorded. In DPC the hologram is digital in the sense that the field of interest and the reference beam interfere on the CCD sensor instead of on the holographic plate. The digital hologram is stored on a computer and used to calculate the amplitude and the phase of the field.

The second step exploits phase conjugation. The conjugate of the calculated phase is assigned to the SLM that shapes a light beam in order to recreate the exact phase conjugated field of the one recorded on the CCD.

As anticipated in the previous chapter, DPC has been used in combination with MMFs to focus and scan light [25], [26]. A calibration focus spot is raster scanned on one facet of the MMF and digital holograms of the fields exiting the fiber are recorded on a CCD. A phase lookup table is calculated and assigned on the SLM. A beam is sent to the SLM, where its wavefront is modulated, and directed back to the fiber through the original path. The phase conjugation process undoes the scrambling caused by the multimodal nature of the fiber and allows the focusing and scanning of light at the proximal end of the MMF. During the calibration step, access to both sides of the fiber is needed. The side from which we calibrate the MMF imaging system with a focus is the same side where the sample will be placed. After the calibration step the fiber can be brought to the sample to perform imaging. The SLM sequentially phase conjugates focus spots in a regular grid in front of the MMF. The interaction light-sample generates a signal that is collected through the same fiber. In case of fluorescence, for example, the collected signal is integrated and displayed as a function of the focus position, forming an image.

Compared to scattering media, where the sample side might be not accessible, the use of MMFs represents a clear advantage. It is still possible to use DPC in scattering media when a “guide star” can be placed inside the medium, functioning as a point source to phase conjugate [27]–[30].

In the next section we present how we implement digital holography and DPC for imaging through MMFs.

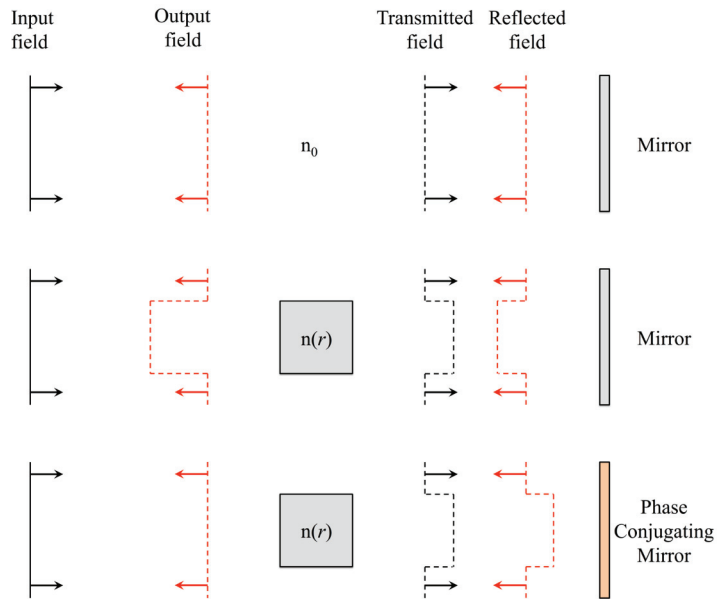


Figure 2.4: **Optical Phase conjugation.** The first row shows a special case in which an ordinary mirror can perform optical phase conjugation. In a homogeneous medium, in case of a plane wave normally incident on the mirror, the reflected wave is, in fact, the phase conjugate of the input wave. If an inhomogeneous medium is present, the ordinary mirror reflects the distorted wave that, passing through the same medium for a second time, gets distorted a second time. In case of a phase conjugating mirror, the phase conjugate of the distorted wave is sent back to the medium. This will retrace the same path experienced in the forward direction and exit the medium as the phase conjugate of the input plane wave.

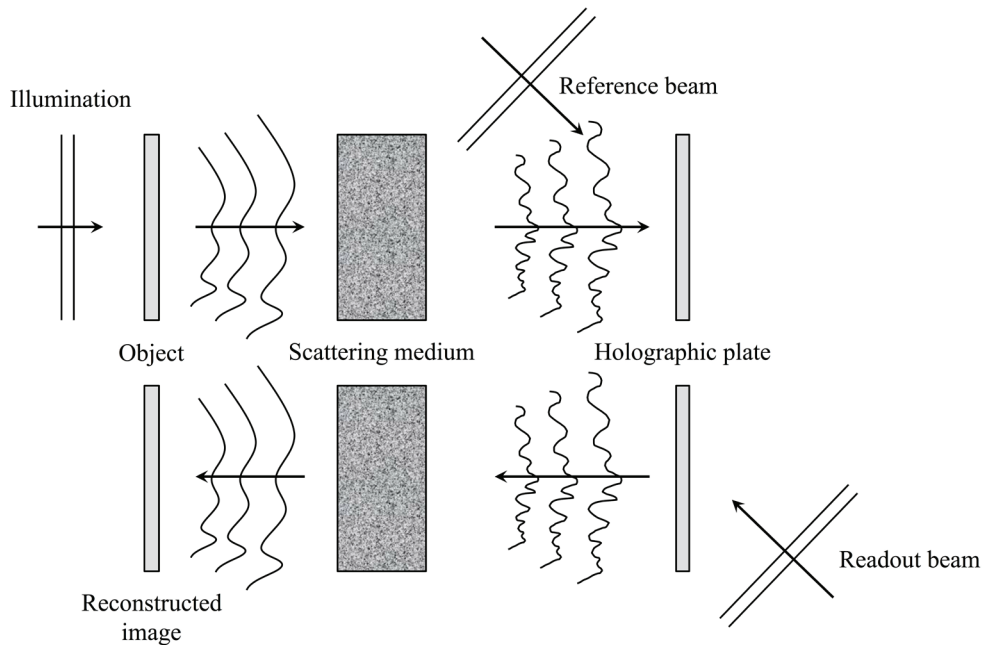


Figure 2.5: **Optical phase conjugation using holography.** The holographic plate, in this case, acts as a phase conjugating mirror. A reconstruction of the field coming from the object is recreated in its original position.

2.5 - Digital hologram reconstruction and DPC implementation

During the calibration step, the phase of the field emerging from the MMFs is measured by digital holography. In all the experiments we performed, we implemented off-axis digital holography [3]. The setup used in the experiments is illustrated in a simplified version in Figure 2.6. A calibration beam is focused in front of the MMF, on the facet we call *distal* end of the fiber. The distal end is the side of the fiber where the sample is going to be placed during the imaging step. The focused beam couples to the modes of the MMF and exits the other side of the fiber, the *proximal* end, as a speckle pattern. The proximal end of the fiber is imaged by a 4f system on a CCD camera. Thanks to the 4f imaging system, the amplitude and the phase of the field emerging from the fiber are replicated in the imaging plane. A reference beam (ideally a plane wave) is directed by a beam splitter towards the CCD, where it arrives with an angle $\theta = (\theta_x, \theta_y)$ between its propagation direction and the optical axis of the imaging system. The interference pattern generated by the superposition of the two fields is recorded and stored on a personal computer. A SLM is positioned such that also its plane represents an imaging plane of the MMF facet (see Figure 2.6).

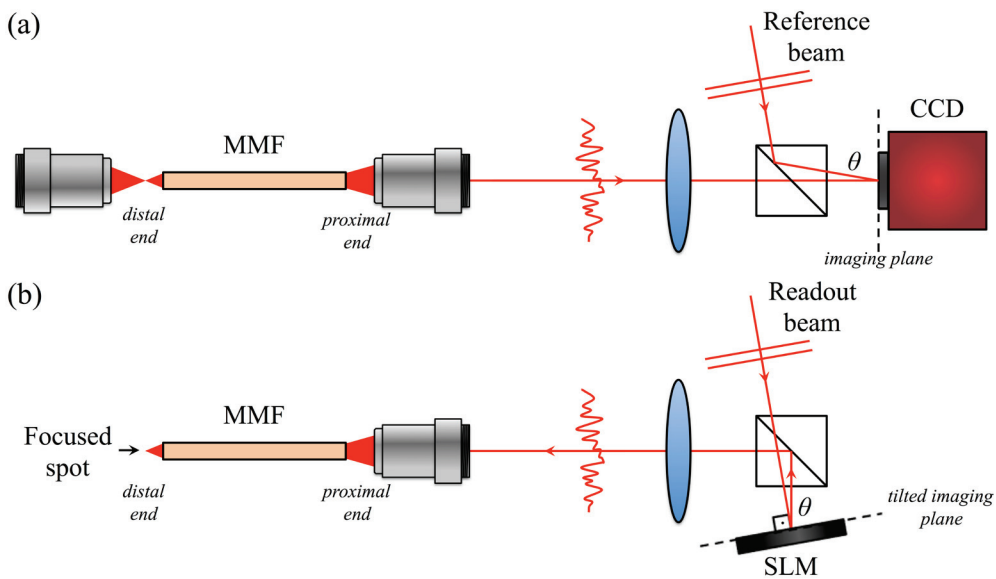


Figure 2.6: **Simplified digital phase conjugation setup.** (a) During a calibration step, light is focused in front of the multimode fiber (MMF). The field emerging from the MMF is imaged by a 4f system on the CCD camera, where it interferes with a flat reference beam creating an off-axis digital hologram. (b) The phase extracted from the digital hologram is conjugated and assigned to the spatial light modulator. The readout beam impinging the SLM picks the assigned phase and is sent back to the MMF by the beam splitter. The phase conjugated beam travels backwards and forms a focus spot at the calibration location.

If we indicate with $S(x,y)$ and $R(x,y)$ the wavefront emerging from the MMF (the signal) and the reference beam, respectively, the two fields on imaging plane can be written as:

$$\begin{aligned} S(x,y) &= |S(x,y)| e^{j\phi_s(x,y)} \\ R(x,y) &= |R(x,y)| e^{-j(K_x x + K_y y)} = |R| e^{-j(K_x x + K_y y)}, \end{aligned} \quad (2.25)$$

Where K_x and K_y are the components of the wavevector of the reference beam projected on the camera plane, and R is the constant amplitude of the plane wave. The intensity on the CCD is given by:

$$\begin{aligned} I &= |S + R|^2 = (S + R)(S + R)^* = |S|^2 + |R|^2 + SR^* + S^*R \\ &= |S|^2 + |R|^2 + S|R| e^{+j(K_x x + K_y y)} + S^*|R| e^{-j(K_x x + K_y y)}, \end{aligned} \quad (2.26)$$

where the dependence on (x,y) has been omitted for simplicity. The intensity I , our digital hologram, is recorder and stored on the computer. At this point, we can digitally retrieve the phase and the amplitude of the signal $S(x,y)$. The Fourier Transform of the digital hologram I , $FT\{I\}$, is given by:

$$\begin{aligned} FT\{I\} &= FT\{|S|^2 + |R|^2\} + |R| FT\{S\} * \delta(k_x - K_x, k_y - K_y) \\ &\quad + |R| FT\{S\}^* * \delta(k_x + K_x, k_y + K_y). \end{aligned} \quad (2.27)$$

From equation 2.27 we can discriminate three terms, or orders. The first term, called zero-order or DC term, placed at the center of the Fourier space, is proportional to the sum of autocorrelations of the signal and the reference. The off-axis configuration of digital holography produces two extra orders, shifted in the Fourier space by an amount dictated by the angle between the reference beam and the signal emerging from the MMF. The +1 order (the second term in equation 2.27) contains the information about the amplitude and the phase of the signal $S(x,y)$. The -1 order, instead, carries the information about the conjugate of the signal, $S^*(x,y)$. The three orders are spatially separated in the frequency space, so it is easy to isolate the term carrying information about the signal of interest applying a spatial filter in the Fourier domain. The inverse Fourier transform of the +1 order only is:

$$H(x,y) = IFT\{|R| FT\{S\} * \delta(k_x - K_x, k_y - K_y)\} = |R| S(x,y) e^{+j(K_x x + K_y y)}. \quad (2.28)$$

As in classical holography, the object can be reconstructed using as read-out beam the reference beam. In this case, this operation is performed digitally, multiplying $H(x,y)$ by the reference beam:

$$R(x,y)H(x,y) = |R|^2 S(x,y) e^{+j(K_x x + K_y y)} e^{-j(K_x x + K_y y)} = |R|^2 S(x,y), \quad (2.29)$$

which is directly proportional to the signal $S(x,y)$. The exact amplitude of $S(x,y)$ can be obtained dividing last expression by the intensity of the reference beam, which can be pre-measured using the CCD. The phase of $S(x,y)$, $\phi_s(x,y)$, is extracted calculating the argument of $S(x,y)$.

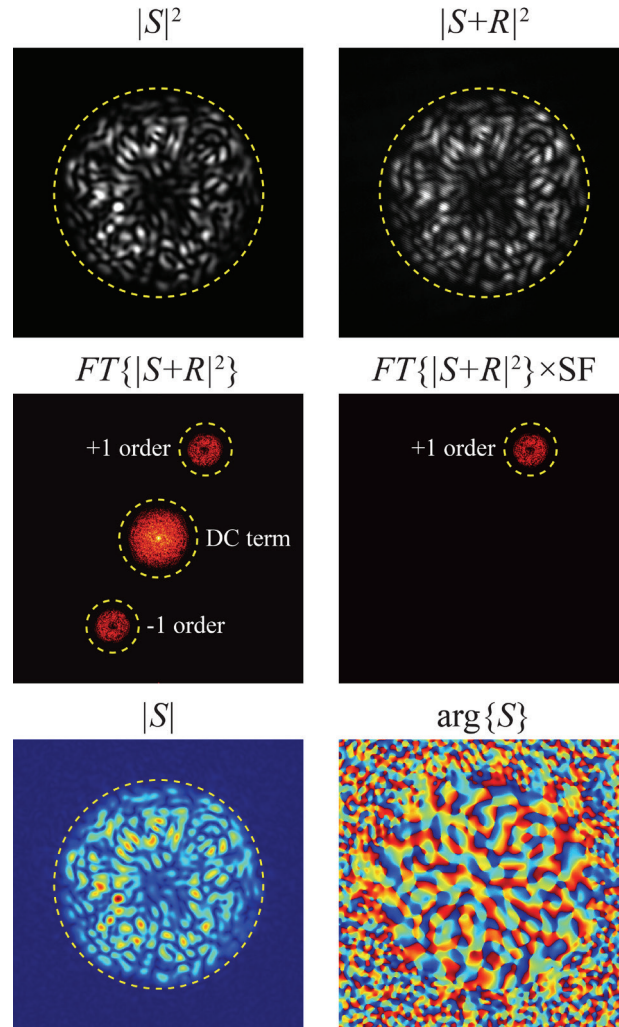


Figure 2.7: **Digital hologram of the output of a multimode fiber.** The first row shows the intensity of the field emerging from the MMF and its interference with the reference beam. The second row shows the spectrum of the hologram and the +1 order isolated by using a spatial filter (SF) in the Fourier domain. From the +1 order it is possible to extract the amplitude and the phase of the field emerging from the fiber, shown in the third row.

At this point DPC can be performed. The phase $\phi_s(x,y)$ is conjugated and assigned to the SLM. The calibration beam is blocked and only the reference beam is used. For our

experiments we use a reflective SLM. The reference beam is sent through the same beam splitter to the SLM. The flat reference beam picks the phase assigned on the SLM and is back-reflected towards the fiber by the beam splitter (see Figure 2.6(b)).

Part of the light that hits the SLM is directly reflected without being modulated. In order to separate this direct reflection from the phase conjugated signal, we introduced a carrier frequency on the SLM of the form of a tilted phase shift, such that the direct reflections are filtered out by the optical system and only the phase conjugated beam reaches the MMF facet, retracing the exact same path experienced during the calibration step [31]. If the alignment between the field $S(x,y)$ and the projected field $S^*(x,y)$ is perfect, a focus spot is formed exactly at the calibration position.

As for a classical objective in microscopy, the minimum size of the focus spot that can be formed using a MMF, depends on the maximum angle that can be transmitted. Or, in other words, the maximum spatial frequency that can be projected is given by the highest spatial frequency the fiber can support. This frequency depends on the NA of the fiber. The maximum resolution attainable is then given by:

$$r \approx 0.61 \frac{\lambda}{NA}. \quad (2.30)$$

This is true when all the modes supported by the MMF are excited during the calibration. In case not all the modes are excited, the resolution will be given by the highest spatial frequency of the highest spatial mode excited during the calibration step.

Interestingly, when all the modes are excited, the average speckle size produced, defined as the average radius of the speckles, is given by $\langle r \rangle \approx 0.61 \lambda / NA$ ([32]). Considering again equation 2.11, describing the number of supported modes in a MMF, and rewriting it in terms of wavelength and NA , we obtain:

$$N \approx \frac{4}{\pi^2} V^2 = \frac{4}{\pi^2} \left[\left(\frac{2\pi}{\lambda} \right) a NA \right]^2 = 16 \left(\frac{a NA}{\lambda} \right)^2 \propto \frac{a^2}{r^2}. \quad (2.31)$$

This means that the number of modes is roughly proportional to the number of resolution spots (or speckles) that “fit” the core area.

The field of view of an imaging system based on MMF is given by the size of the core, a . In fact, the requirement to phase conjugate a spot is that the calibration focus couples to the modes supported by the MMF and no information is lost. If the calibration spot is focused on the facet of the MMF within the core, all the light reaches the proximal end of the MMF by total internal reflection, is holographically detected and can be phase conjugated.

2.6 - DPC of ultrashort pulses

So far we have assumed the optical field introduced in the optical fiber being monochromatic and time independent. When the laser light that is coupled into an optical fiber is pulsed, because of the dispersive nature of silica, the pulse undergoes temporal broadening. If we neglect nonlinear effects, the propagation of the pulse is affected only by

group velocity dispersion (GVD), and a combination of material and waveguide dispersion [1], [2]. We will not enter specifically in the physical explanation of the phenomena causing dispersion, but we will give here a qualitative description, in order to understand how we have dealt with femtosecond pulses through optical fiber to perform two-photon imaging.

Material dispersion is a time delay introduced by the fact that the refractive index of glass material changes as a function of frequency [2]. The waveguide dispersion is mainly caused by the mode confinement in the waveguide and the difference in speed between the core and the cladding [2]. For what concerns GVD we need to introduce some definitions first. Let us start considering a complex wavefunction $E(\vec{r}, t)$. Since we are interested in the temporal properties only, we will consider from now on only its time dependence, $E(t)$. A pulsed plane wave can be described as:

$$E(t) = p(t)e^{j\omega_0 t}, \quad (2.32)$$

where $p(t)$ is the complex pulse envelope and $\omega_0 = 2\pi\nu_0$ is the central angular frequency. When a pulse travels in a lossless dispersive medium with a refractive index $n(\omega)$, the velocity at which the envelope $p(t)$ propagates through space is called group velocity (v_g) and is defined as:

$$\frac{1}{v_g} = \left. \frac{\partial \beta}{\partial \omega} \right|_{\omega=\omega_0}, \quad (2.33)$$

where $\beta = \omega n(\omega)/c_0$ is the frequency dependent propagation constant. The group velocity is also often frequency dependent, so each frequency component of the pulse, propagating for the same distance L in the same material, experiences different time delays, $\tau_d(\omega) = L/v_g(\omega)$. This phenomenon is what is called GVD and causes pulse time broadening. This effect happens for single mode fibers, and is even more dramatic for MMFs. In fact each mode has its own propagation constant and, as a consequence is own group velocity. Neglecting mode-to-mode coupling, sending a pulsed plane wave in a MMF, each mode is going to exit the proximal end at a different time, dictated by the length of the fiber and the group velocity. This effect is called multimode dispersion. The energy of the initial pulse is spread in each mode, in an overall longer pulse. In principle, if we are able to detect only one of the modes at the output of the fiber and phase conjugate it back, this mode will only be spread by the material characteristics of the fiber and would not be influenced by the multimode dispersion.

As suggested in previous works ([33], [34]), it is possible to record different time slots of the output pulse by using coherence gated digital holography. A pulse is split in two arms: one arm is sent in the MMF and the other is used as a known reference field.

The output of the MMF and the reference pulsed beam are recombined with a beam splitter, and a digital off-axis hologram is recorded on a CCD. The short duration of the reference pulse time-gates the recording process of the digital hologram. Delaying the arrival

time of the reference pulse with respect to the field that emerges from the MMF by a time delay τ , it is possible to time-sample the signal of interest.

As for the continuous wave case, let us try to express what is the expression of the intensity captured by the CCD camera sensor. The signal optical field from the MMF and the reference pulse are respectively:

$$\begin{aligned} S(\vec{r}, t) &= |S(\vec{r}, t)| e^{j\omega_0 t} e^{j\phi_s(\vec{r}, t)} e^{-j\vec{k}_1 \vec{r}} \\ R(\vec{r}, t) &= |p(\vec{r}, t + \tau)| e^{j\omega_0(t+\tau)} e^{-j\vec{k}_2 \vec{r}}, \end{aligned} \quad (2.34)$$

The intensity on the camera is given by:

$$\begin{aligned} I(\vec{r}, t) &= \int_0^T |S(\vec{r}, t) + R(\vec{r}, t)|^2 dt = \\ &= \int_0^T |S(x, y, t)|^2 + |p(x, y, t + \tau)|^2 + S(x, y, t)R(x, y, t)^* + S(x, y, t)^* R(x, y, t) dt \\ &= \int_0^T |S(x, y, t)|^2 + |p(x, y, t + \tau)|^2 \\ &\quad + S(x, y, t)|p(x, y, t + \tau)| e^{j\omega_0(t+\tau)} e^{+j(K_x x + K_y y)} \\ &\quad + S(x, y, t)^* |p(x, y, t + \tau)| e^{j\omega_0(t+\tau)} e^{-j(K_x x + K_y y)} dt, \end{aligned} \quad (2.35)$$

where T is the integration time of the camera and where the z component has been omitted placing the camera in $z=0$. If we follow the same procedure described before to estimate the field emerging from the fiber, we can rewrite equation 2.28 for the time dependent case as:

$$H(x, y, t) = \int_0^T S(x, y, t) |p(x, y, t + \tau)| e^{j\omega_0(t+\tau)} e^{+j(K_x x + K_y y)} dt. \quad (2.36)$$

If we assume that the duration of the envelope $p(x, y, t + \tau)$ is much shorter than the broad pulse coming from the MMF, we can assume the reference pulse being a delta function in time. The convolution integral in equation 2.36 becomes:

$$H(x, y, \tau) = S(x, y, \tau) e^{j\omega_0 \tau} e^{+j(K_x x + K_y y)} = |S(x, y, \tau)| e^{j\phi_s(x, y, \tau)} e^{j\omega_0 \tau} e^{+j(K_x x + K_y y)}. \quad (2.37)$$

This means that we can extract the amplitude and the phase of $S(\vec{r}, t)$ at a given time τ .

If the time separation of the modes is larger than the duration of the reference pulse, the field of each mode can be separately holographically recorded. Delaying the arrival time of the reference pulse, it is possible to record a different mode. If the separation is not long enough, the coherence gated hologram will record the superposition of a subset of modes with similar group velocities.

Morales et al. showed in reference [35] that capturing a digital hologram of a subset of the modes exiting a 30 cm MMF, they were able to phase conjugate a pulse with a duration

of approximately $1/30^{\text{th}}$ of the duration obtained exciting all the modes supported by the fiber. Moreover, the spatial control given by the SLM, still allows to combine the modes in space in order to spatially focus. This opens possibilities for multi-photon point scanning imaging as it will be shown in **Chapter 5**.

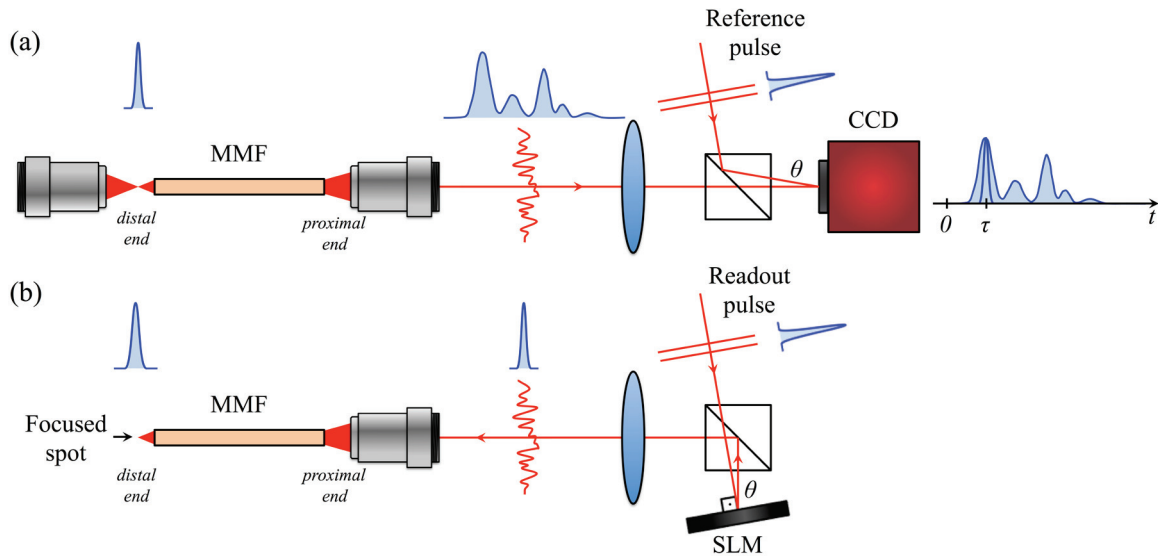


Figure 2.8: **Digital phase conjugation of ultrashort pulses.** (a) During the calibration step, an ultrashort pulse is spatially focused in front of the multimode fiber (MMF). The field emerging from the MMF is spatially scrambled by the coupling in different modes and is spread in time because of dispersion. The field is imaged by the 4f system on the CCD camera, where it interferes with a reference ultrashort reference pulse. The reference pulse time-gates the holographic process, resulting in the measurement of the phase of a specific time slot of the signal emerging from the MMF. A different subset of modes can be measured time delaying the reference pulse compared to the signal. The time delay is τ . (b) The phase extracted from the digital hologram is conjugated and assigned to the spatial light modulator. The measured phase corresponds to a subset of modes with similar propagation constants. Phase conjugating these modes, we can spatially focus light. The dispersion of the phase conjugated pulse at the distal end will be mainly due to chromatic dispersion in the MMF.

2.7 - DPC through different multimode waveguides

What we have described so far in the case of MMF, still applies for other kind of optical fibers that can support many modes. In **Chapter 3**, for example, we exploit capillary waveguides (CWG) as optical fibers instead of MMFs. The reason for that, as will be extensively discussed in **Chapter 3**, is to create a physical access between the distal and the proximal side of the endoscope. A CWG is basically a MMF that comprises a low refractive index cladding and presents a hollow core at the center of the high refractive index silica core. The guiding mechanism, also in this case, is total internal reflection in the high refractive index core. The modes supported by CWG will have different shapes compared to the one on a MMF, but the same wavefront shaping process can still be applied.

From **Chapter 5**, we will use as optical fibers coherent fiber bundles, also known as multicore fibers (MCFs). A MCF is a collection of single mode (or few modes) fibers sharing a common low refractive index cladding, arranged in a periodic or quasi-periodic matrix. In this case each mode supported in each core represents one spatial degree of freedom. The number of degrees of freedom coincides with the number of individual cores when the cores are single mode fibers. In case of few modes fibers, the total number of degrees of freedom is given by the number of supported modes in each core times the number of cores. In usual imaging through MCF, each core represents one pixel of the final image. In our case, introducing a working distance such that all the modes from the cores interfere with each other, we can use the same wavefront shaping techniques mentioned before to focus light. In the specific case of DPC, in order to use all the degrees of freedom supported by the MCF, the calibration spot is placed at a distance from the MCF such that it gets coupled to all the cores (see **Chapter 6** for details). Cross-talk between cores, which usually represents a problem in MCFs, during the DPC process is seen as coupling between modes in MMFs. This means that core-to-core coupling does not affect the focusing process. Figure 2.9 illustrates the difference between MMF, CWG and MCF.

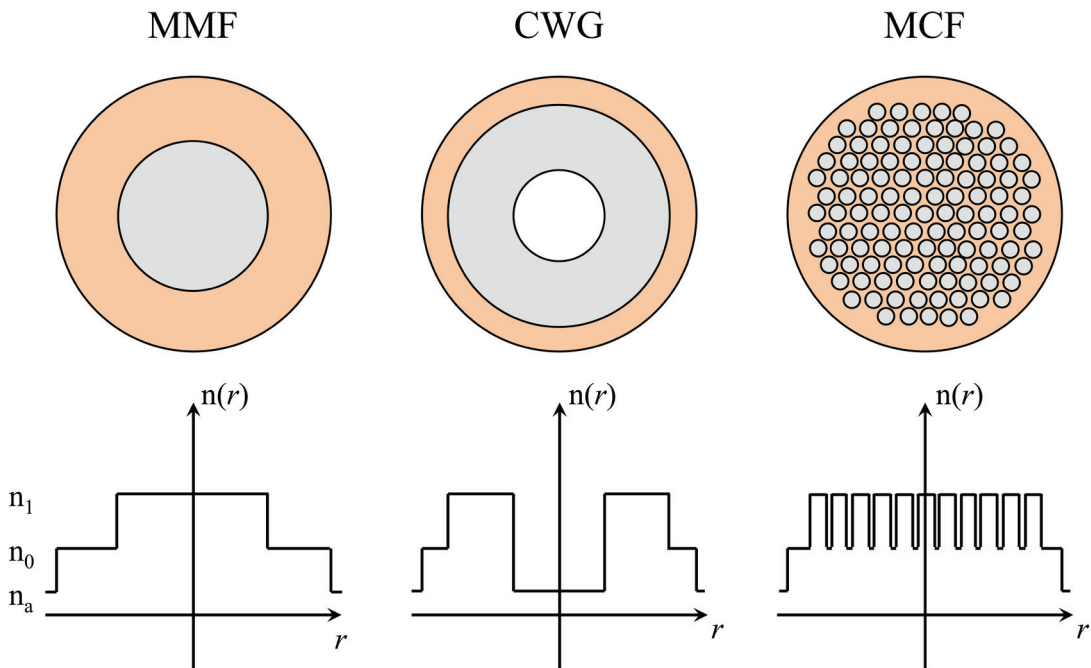


Figure 2.9: **Comparison between different kinds of optical fibers.** The first row shows the spatial arrangement of core and cladding of a multimode fiber (MMF), a capillary waveguide (CWG) and a multicore fiber (MCF). The second row shows the index distribution as a function of the optical fiber radius (n_1 = core refractive index, n_0 = cladding refractive index, n_a = surrounding medium refractive index.)

Bibliography

- [1] B. E. A. Saleh and M. C. Teich, *Fundamentals of Photonics*. Wiley, 2013.
- [2] K. Okamoto, *Fundamentals of Optical Waveguides*. Academic Press, 2010.
- [3] J. W. Goodman, *Introduction to Fourier Optics*. Roberts and Company Publishers, 2005.
- [4] A. Yariv and P. Yeh, *Photonics: Optical Electronics in Modern Communications*. Oxford University Press, 2007.
- [5] M. Plöschner, T. Tyc, and T. Čižmár, “Seeing through chaos in multimode fibres,” *Nat. Photonics*, vol. 9, no. 8, pp. 529–535, Aug. 2015.
- [6] I. M. Vellekoop and A. P. Mosk, “Universal Optimal Transmission of Light Through Disordered Materials,” *Phys. Rev. Lett.*, vol. 101, no. 12, p. 120601, Sep. 2008.
- [7] S. M. Popoff, G. Lerosey, R. Carminati, M. Fink, A. C. Boccara, and S. Gigan, “Measuring the Transmission Matrix in Optics: An Approach to the Study and Control of Light Propagation in Disordered Media,” *Phys. Rev. Lett.*, vol. 104, no. 10, p. 100601, Mar. 2010.
- [8] S. M. Popoff, G. Lerosey, M. Fink, A. C. Boccara, and S. Gigan, “Controlling light through optical disordered media: transmission matrix approach,” *New J. Phys.*, vol. 13, no. 12, p. 123021, Dec. 2011.
- [9] Y. Choi *et al.*, “Scanner-Free and Wide-Field Endoscopic Imaging by Using a Single Multimode Optical Fiber,” *Phys. Rev. Lett.*, vol. 109, no. 20, p. 203901, Nov. 2012.
- [10] R. Di Leonardo and S. Bianchi, “Hologram transmission through multi-mode optical fibers,” *Opt. Express*, vol. 19, no. 1, pp. 247–254, Jan. 2011.
- [11] T. Čižmár and K. Dholakia, “Shaping the light transmission through a multimode optical fibre: complex transformation analysis and applications in biophotonics,” *Opt. Express*, vol. 19, no. 20, pp. 18871–18884, Sep. 2011.
- [12] T. Čižmár and K. Dholakia, “Exploiting multimode waveguides for pure fibre-based imaging,” *Nat. Commun.*, vol. 3, p. 1027, Aug. 2012.
- [13] S. Bianchi and R. D. Leonardo, “A multi-mode fiber probe for holographic micromanipulation and microscopy,” *Lab. Chip*, vol. 12, no. 3, pp. 635–639, Jan. 2012.
- [14] J. W. Goodman, W. H. J. Huntley, D. W. Jackson, and M. Lehmann, “Wavefront-Reconstruction imaging through random media,” *Appl. Phys. Lett.*, vol. 8, no. 12, pp. 311–313, Jun. 1966.
- [15] E. N. Leith and J. Upatnieks, “Holographic Imagery Through Diffusing Media,” *J. Opt. Soc. Am.*, vol. 56, no. 4, pp. 523–523, Apr. 1966.
- [16] H. Kogelnik and K. S. Pennington, “Holographic Imaging Through a Random Medium,” *J. Opt. Soc. Am.*, vol. 58, no. 2, pp. 273–274, Feb. 1968.
- [17] E. Spitz and A. Werts, “Transmission des images à travers une fibre optique,” *Comptes Rendus Hebd Séances Académie Sci Sér B 264*, vol. 4, pp. 1015–1018, 1967.
- [18] A. Yariv, “Three-dimensional pictorial transmission in optical fibers,” *Appl. Phys. Lett.*, vol. 28, no. 2, pp. 88–89, Jan. 1976.
- [19] A. Gover, C. P. Lee, and A. Yariv, “Direct transmission of pictorial information in multimode optical fibers*,” *JOSA*, vol. 66, no. 4, pp. 306–311, Apr. 1976.
- [20] G. J. Dunning and R. C. Lind, “Demonstration of image transmission through fibers by optical phase conjugation,” *Opt. Lett.*, vol. 7, no. 11, pp. 558–560, Nov. 1982.

- [21] T. Ogasawara, M. Ohno, and K. Karaki, “One-way image transmission with a pair of multimode optical fibers and a phase-conjugate mirror,” *Opt. Lett.*, vol. 20, no. 23, pp. 2435–2437, Dec. 1995.
- [22] Z. Yaqoob, D. Psaltis, M. S. Feld, and C. Yang, “Optical phase conjugation for turbidity suppression in biological samples,” *Nat. Photonics*, vol. 2, no. 2, pp. 110–115, Feb. 2008.
- [23] M. Cui and C. Yang, “Implementation of a digital optical phase conjugation system and its application to study the robustness of turbidity suppression by phase conjugation,” *Opt. Express*, vol. 18, no. 4, pp. 3444–3455, Feb. 2010.
- [24] C. Bellanger, A. Brignon, J. Colineau, and J. P. Huignard, “Coherent fiber combining by digital holography,” *Opt. Lett.*, vol. 33, no. 24, pp. 2937–2939, Dec. 2008.
- [25] I. N. Papadopoulos, S. Farahi, C. Moser, and D. Psaltis, “Focusing and scanning light through a multimode optical fiber using digital phase conjugation,” *Opt. Express*, vol. 20, no. 10, p. 10583, May 2012.
- [26] I. N. Papadopoulos, S. Farahi, C. Moser, and D. Psaltis, “High-resolution, lensless endoscope based on digital scanning through a multimode optical fiber,” *Biomed. Opt. Express*, vol. 4, no. 2, p. 260, Feb. 2013.
- [27] L. Le Xuan *et al.*, “Photostable Second-Harmonic Generation from a Single KTiOPO4 Nanocrystal for Nonlinear Microscopy,” *Small*, vol. 4, no. 9, pp. 1332–1336, Sep. 2008.
- [28] C.-L. Hsieh, Y. Pu, R. Grange, and D. Psaltis, “Digital phase conjugation of second harmonic radiation emitted by nanoparticles in turbid media,” *Opt. Express*, vol. 18, no. 12, pp. 12283–12290, Jun. 2010.
- [29] C.-L. Hsieh, Y. Pu, R. Grange, G. Laporte, and D. Psaltis, “Imaging through turbid layers by scanning the phase conjugated second harmonic radiation from a nanoparticle,” *Opt. Express*, vol. 18, no. 20, pp. 20723–20731, Sep. 2010.
- [30] X. Yang, C.-L. Hsieh, Y. Pu, and D. Psaltis, “Three-dimensional scanning microscopy through thin turbid media,” *Opt. Express*, vol. 20, no. 3, pp. 2500–2506, Jan. 2012.
- [31] I. Papadopoulos, “Dynamic control of light transmission through multimode fibers,” PhD Thesis, École Polytechnique Fédérale de Lausanne, Lausanne, Switzerland, 2014.
- [32] J. W. Goodman, *Speckle Phenomena in Optics: Theory and Applications*. Roberts and Company Publishers, 2007.
- [33] R. Rokitski, P.-C. Sun, and Y. Fainman, “Study of spatial–temporal characteristics of optical fiber based on ultrashort-pulse interferometry,” *Opt. Lett.*, vol. 26, no. 15, pp. 1125–1127, Aug. 2001.
- [34] R. Rokitski and S. Fainman, “Propagation of ultrashort pulses in multimode fiber in space and time,” *Opt. Express*, vol. 11, no. 13, pp. 1497–1502, Jun. 2003.
- [35] E. E. Morales-Delgado, S. Farahi, I. N. Papadopoulos, D. Psaltis, and C. Moser, “Delivery of focused short pulses through a multimode fiber,” *Opt. Express*, vol. 23, no. 7, p. 9109, Apr. 2015.

Chapter 3

Fluorescence and optical-resolution photoacoustic imaging through capillary waveguides using digital phase conjugation

As described in the previous introductory chapters, phase conjugation can be used to focus and scan a laser beam at the tip of a multimode optical fiber. Fluorescence or back scattered light from the interrogated sample can be collected through the same fiber to form an image. In order to increase the amount of information about the sample, photoacoustic imaging can be exploited, which provides image contrast of absorbance [1], [2]. Optical-resolution photoacoustic imaging has been demonstrated through multimode fibers [3]. The generated signal had to be detected at the tip of the multimode fiber because, contrary to fluorescence or backscattered light, the acoustic signal cannot travel back through the optical fiber and be detected on the proximal side. This leaves two options for implementations in MMFs. The first option is the introduction of a miniaturized ultrasound transducer at the tip of the optical fiber, which would increase the lateral dimension of the endoscope. The second is the placement of the transducer outside the body. This second option limits the imaging depth to few millimeters due to attenuation of ultrasound in tissues.

In this chapter we demonstrate that using digital phase conjugation, a 330 μm diameter, water-filled silica capillary waveguide can be used as an endoscopic probe to obtain both fluorescence *and* optical resolution photoacoustic imaging, with no optical or acoustic elements at the tip of the waveguide. This is possible by exploiting the properties of capillary waveguides as optical *and* acoustic waveguides [4]. We study the consequences of using digital phase conjugation combined with a capillary waveguide and we conclude with possible future improvements of our endoscopic approach.

Most of the material presented in this chapter can be found in the publications ([5], [6]):

- **N. Stasio***, A. Shibukawa*, I. N. Papadopoulos S. Farahi, O. Simandoux, J. P. Huignard, E. Bossy, C. Moser, D. Psaltis, “Towards new applications using

capillary waveguides,” *Biomed. Opt. Express*, vol. 6, no. 12, pp. 4619–4631, Dec. 2015.

- **N. Stasio**, A. Shibukawa, I. N. Papadopoulos S. Farahi, O. Simandoux, J. P. Huignard, E. Bossy, C. Moser, D. Psaltis, “Fluorescence and optical-resolution photoacoustic imaging through capillary waveguides,” 2016, vol. 9717, p. 97171H–97171H–8.

* Equally contributing authors

3.1 - Introduction

Glass capillaries, referred to as capillary waveguides (CWGs) in the photonics community due to their ability to support the propagation of waveguiding modes in the annular glass ring, have been consistently exploited by researchers as sensors [7] or as biosensors in lab on a chip platforms [8]. Nevertheless no application was demonstrated showing their use as an imaging device *per se*. Although optical fibers are widely used in endoscopy, at first glance the use of a CWG for endoscopic purposes does not bring advantages. In reality however, the presence of a physical access to the sample side, enabled by the presence of the hollow core at the center, adds a degree of freedom to the endoscopic device, which can be used for many applications. For example an endoscopic device can be used to deliver high-energy light for ablation purposes, so the hollow core could be used for eliminating gases formed during the ablation process. Alternatively, an endoscope based on CWGs can be used to check *in vivo* the effect of drugs that can be injected using the same device.

As said previously, usually endoscopes are made out of bundles of single mode fibers, or one single mode fiber equipped with a micro-fabricated lens and a scanning system to steer the laser beam [9], [10]. One problem carried by a direct transition from single-mode fibers to CWGs is that lateral dimension of the endoscopic device would increase. Fiber bundles and single-mode fiber endoscopes usually have large diameters (in the millimeter range): adding a hollow core in each optical fiber would not improve this aspect. Moreover, the point spread function of the imaging system would change from a quasi-Gaussian beam (the fundamental mode of a single-mode fiber) to a donut-like beam (the fundamental mode of a CWG), implying a deconvolution step while doing imaging.

We have shown in the previous chapters how, dynamically shaping light using a spatial light modulator (SLM), it is possible to scan a focus spot at the distal end of the MMF and collect the optically generated signal through the same fiber. In this way using an ultrathin fiber (only few hundreds of micrometers), can be converted in a high-resolution minimally invasive endoscope.

This approach can be adapted to ultrathin capillaries having a relatively thick silica wall, which can be used as multimode optical waveguide. The use of a SLM can turn a CWG into an imaging system, paving the way to new applications that would be otherwise impossible to achieve in conventional fiber based endoscopy.

In this chapter we demonstrate two new possible applications: using digital phase conjugation (DPC), a 330 μm -thick silica capillary can also be used as a fluorescence and

optical resolution photoacoustic endoscope. We combine fluorescence endoscopy [9] with optical resolution photoacoustic microscopy, which measures optical absorption in biological bodies [11], [12]. A double imaging modality, in fact, can allow the acquisition of additional information about the structural and molecular heterogeneities of interrogated biological samples [13].

Photoacoustic imaging is possible using a highly energetic nanosecond laser pulse, which, when absorbed by a sample, generates an acoustic wave due to thermoelastic expansion. The detection of the photoacoustic waves using an ultrasound (US) transducer enables the formation of an image. If the resolution is limited by the ability of focusing light in a diffraction limited volume, we can speak about optical-resolution photoacoustic microscopy (OR-PAM) [14], [15]. When widefield light is used to illuminate the sample, the resolution is given by the maximum US detectable frequency and by the characteristics of the US transducer. In this case we have acoustic-resolution photoacoustic microscopy (AR-PAM), with transverse resolution ranging from hundreds of micrometers to millimeters [1], [2].

OR-PAM images are obtained by scanning a diffraction limited focused spot which can be done deep in tissues using a fiber bundle optical endoscope [13], [16] and detecting the sound with an external US transducer. Fully encapsulated AR-PAM endoscopes have been demonstrated by Yang et al. [17], [18] using a single mode fiber and an actuation system for the beam steering. Recently OR-PAM images have been acquired by the same group using a device with an outer diameter of 3.4 mm and a lateral resolution of 9.2 μm [19]. OR-PAM by using a MMF has been demonstrated by Papadopoulos et al in [3]. The photoacoustic signal was collected using an external US transducer placed next to the interrogated sample, forming the photoacoustic image. The frequency of the generated signal was larger than 10 MHz. Since the attenuation of US in tissue increases linearly with frequency (around 0.5 dB/cm/MHz, [20]) the imaging depth using this approach is limited to a few millimeters [3]. We demonstrated that one way to guide the photoacoustic signal outside the body is to use CWGs. A water-filled silica capillary can guide acoustic waves through a 3 cm thick fat layer, enabling OR-PAM [4]. In this case, in order to form an image, the photoacoustic signal was created by focusing and scanning light through a microscope objective placed on the sample side.

We utilized the annular core as a multimode optical waveguide and the water-filled core as an acoustic waveguide. Using DPC we could focus and scan a laser beam and detect both the fluorescence and photoacoustic signal through a CWG device. Furthermore, we show that this approach is minimally invasive: after an initial calibration step, no optical element is needed on the sample side, resulting in an ultrathin and totally passive endoscopic probe.

3.2 - Materials and methods

Figure 3.1 shows a picture of our CWG and a simplified schematic of its structure. The silica part of the capillary waveguide has a higher refractive index than the cladding and the hollow core (Figure 3.1(b)). Therefore light undergoes total internal reflection at every

interface of the CWG and can be guided [21]. The CWGs used in this work have an external diameter of only 330 μm . Surrounded by the 10 μm -thick cladding are the silica layer and the hollow core. The effective numerical aperture (NA) of the optical waveguides is 0.22, so using hollow core diameters of 100 μm and 150 μm , the silica part of the CWG behaves as a multimode optical waveguide, allowing focusing light by using DPC. The 100- μm and 150- μm inner diameter CWGs have approximately 5×10^4 and 6×10^4 optical guided modes, respectively. The water-filled core, which has a lower phase velocity compared to the silica, can be used as an acoustic waveguide to collect the US waves. Analogous to the case of light waveguiding in the silica part, this phase velocity contrast keeps the US wave confined inside the fluid core via total internal reflection at the fluid-solid interface [22]. In the frequency range observed in this work (10-30 MHz), the CWG with an internal diameter of 150 μm is a few mode acoustic waveguide. In particular, the first-order quasi-piston mode can propagate in the water-filled hollow core and exits the CWG as a quasi-spherical wave, which can be detected by a spherically focused US transducer [4].

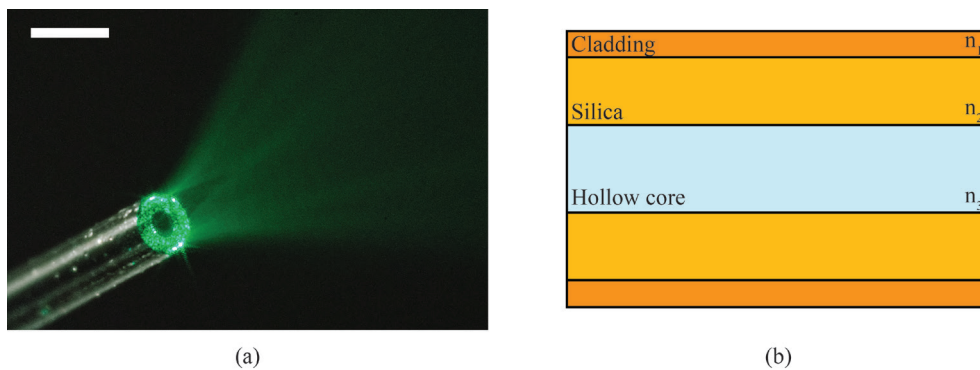


Figure 3.1: **Capillary waveguides.** (a) Light escaping the capillary waveguide (CWG): a closer look to the silica annular part shows the speckle diffraction pattern characteristic of multimode waveguides. Scale bar 500 μm ; (b) Schematic of the side cross-sectional view of a CWG: the silica annular part of the CWG has a refractive index n_2 higher than the cladding (n_1) and the hollow core (n_3 , usually air or water), so light can be guided by total internal reflection. The hollow core adds a degree of freedom to this kind of waveguides respect to common optical fibers. The overall diameter of the CWG is 330 μm . The cladding is 10 μm -thick. The remaining part is composed of the silica part and the hollow core. In this work we used inner diameters of 150 μm (silica part 76.5 μm -thick) and 100 μm (silica part 106.5 μm -thick).

The basic experimental setup is shown in Figure 3.2. The output of a Q-switched Nd:YVO4 laser (wavelength of 532 nm, pulse width of 5 ns, repetition rate 200 Hz, output energy 300 μJ /pulse, NL-201, EKSPLA, Lithuania) is expanded and collimated using the lenses OBJ1 and L1. The polarizing beam splitter (PBS) splits the beam in two arms: the *calibration arm* goes to the CWG and the *imaging arm* is used as the reference beam to record the digital hologram for DPC. The former goes through a couple of galvomirrors (Cambridge Technology Inc., USA) and relayed through the unit-magnification 4f system L2-L3 ($f = 10$ cm) onto the back focal plane of the objective OBJ2. The pair of

galvomirrors scans a focused spot in a regular grid in a plane at the distal end of the capillary (the *sample side*). On the other side of the capillary (the *proximal side*) the light coupled into the propagation modes of the capillary for each position of the focus, generates a speckle pattern. The amplitude and phase of this speckle pattern is digitally recorded with a CMOS detector (MV1-D1312IE-100-G2-12, Photonfocus, Switzerland) using off-axis digital holography. The half-wave plate ($\lambda/2$) placed before the PBS controls the power ratio between the imaging and calibration arms. A delay line on the imaging arm is added in order to match the optical path length of the two arms and therefore to obtain the best interference fringe contrast. From each off-axis hologram, the phase of the speckle pattern can be digitally calculated on a personal computer. The conjugated distributions of the detected phases are assigned to the spatial light modulator (SLM - Pluto-VIS, Holoeye, Germany). The phase conjugated beams are sent back inside the waveguide, allowing the scanning of a focused spot on the sample side. During this operation, the calibration beam is blocked. The focus spot is formed again at the original position and it is imaged on the camera marked CCD in Figure 3.2 through the 4f system OBJ2-L5 and the non-polarizing beam splitter BS1. The pulse energy at each phase conjugated spot is estimated around 500 nJ/pulse. It should be noted that after the calibration step, no optical element or transducer is needed on the sample side.

In the case of fluorescence imaging, the calibration objective OBJ2 is a 50 \times long working distance (WD) objective ($NA = 0.55$, $WD = 13$ mm, Mitutoyo, Japan) and OBJ3 is a 20 \times objective ($NA = 0.42$, $WD = 20$ mm, Mitutoyo, Japan). The light generated by the fluorescent sample is collected back through the silica ring of the CWG and detected by the CMOS camera. Two kinds of flexible fused silica capillaries are used to carry out the experiments: a polyimide coated ($NA = 0.22$, LTSP150375, Polymicro Technologies, USA) and a transparent Teflon coated ($NA = 0.22$, TSU100375, Polymicro Technologies, USA). The former has an inner diameter of 150 μm and silica guiding part of 76.5 μm ; the latter has an inner diameter of 100 μm and a silica wall 106.5 μm -thick. For fluorescence imaging no substantial difference in the image quality was observed. The results shown later in the text were obtained using the Teflon coated CWG, which has a higher photon collection due to the thicker silica walls.

In the case of photoacoustic imaging, the calibration objective OBJ2 is a 20 \times objective ($NA = 0.42$, $WD = 20$ mm, Mitutoyo, Japan) and OBJ3 is a 10 \times objective ($NA = 0.28$, $WD = 33.5$ mm, Mitutoyo, Japan). During the PAM experiment we use the polyimide coated CWG (LTSP150375, Polymicro Technologies, USA), which has better performances in terms of guidance and collection of the acoustic waves [4], [23] due to its larger inner diameter. The setup shown in Figure 3.2 was slightly modified to enable the US collection: the CWG is filled with water and immersed in a water tank (Figure 3.3). The change in the calibration objective OBJ2 compared to the fluorescence imaging experiment is only due to its reduced dimensions (the 20 \times is 75mm-long, while the 50 \times is 82 mm-long) and longer working distance that facilitates the accommodation of the water tank without redesigning the optical setup. The capillary holder physically separates the sample side from the proximal side: neither light nor sound waves can pass through it, so the sample is completely

inaccessible. Thanks to DPC and the CWG, light focuses on the sample and generates a US wave that travels back to the proximal side through the liquid core.

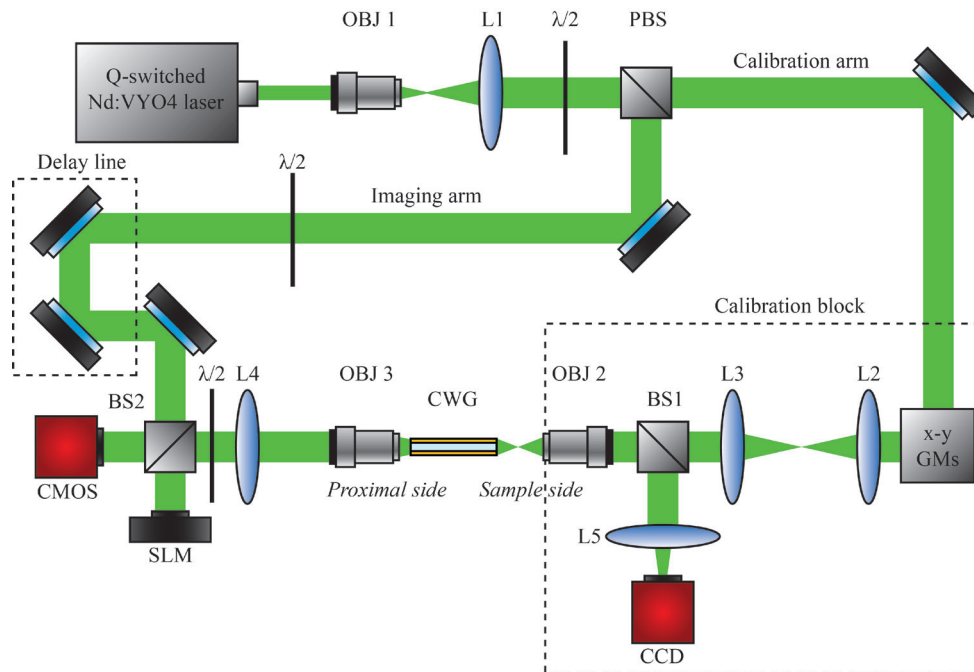


Figure 3.2: **Experimental optical setup for endoscopy through capillary waveguides.** The beam is expanded by the telescope formed by lenses OBJ1-L1 and is split in two arms by the polarizing beam splitter PBS: the calibration arm and the imaging arm. The calibration arm beam is focused on the capillary waveguide (CWG) by the objective OBJ2. The output of the capillary is imaged on the CMOS sensor through the 4f imaging system OBJ3-L4. The imaging arm, used as a reference beam, is combined with the image through the non-polarizing beam splitter BS2 generating a hologram. The phase conjugate beam is generated by displacing the calculated phase pattern on the SLM and the reference beam and is redirected back in CWG by BS2. The imaging system OBJ2-L5 and the beam splitter BS1 allow to check the generation of the phase conjugated focused spot on the CCD camera. The delay line and the half wave plates ($\lambda/2$) are used to optimize the quality of the digital hologram.

The US wave is reflected upwards by a 150 μm -thick glass slide and is collected by an acoustic transducer (20 MHz, spherically focused, 10.4 mm focal distance, 3.175 mm diameter, Olympus, Japan). The generated electric signal is amplified by a low noise amplifier (DPR500, remote pulser RP-L2, JSR Ultrasonics, USA) and displayed on an oscilloscope. To form the image, the average of 64 photoacoustic signal traces per pixel is recorded on a personal computer for further data processing. The transducer has to be carefully aligned to the hollow core of the CWG in order to be able to detect the US signal. The lateral resolution of the focused transducer used in this experiment, in fact, is comparable to the size of the inner diameter of the CWG. In order to maximize the detected signal, the transducer was first placed on top of CWG. Using the transducer in pulse-echo mode, an US pulse was fired towards the CWG and the position in the z -direction was

adjusted to maximize the detected echo signal. Following the CWG wall, the US transducer was shifted along the x -direction up to the glass slide acting as an acoustic reflector. The z -direction was adjusted again in order to detect the echo coming from the facet of the CWG. At this point the transducer was scanned in x and y in order to align it to the center of the CWG facet.

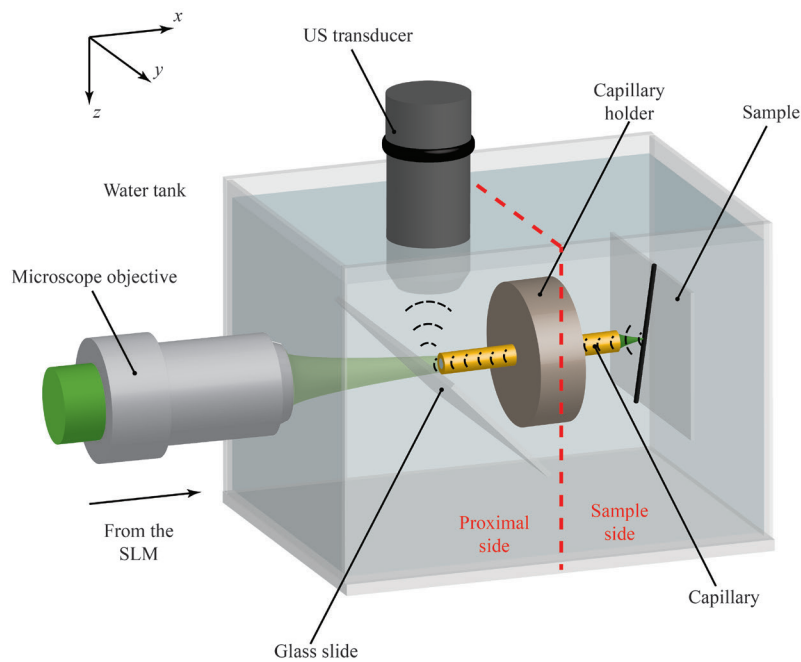


Figure 3.3: **Experimental setup for photoacoustic imaging.** The shaped laser beam coming from the SLM is coupled back into the capillary waveguide and creates a sharp focus spot on the sample side. The absorption of nanosecond laser pulse by the sample results in a photoacoustic wave that is guided backwards to the proximal side by the water-filled capillary core, used as an acoustic waveguide. The glass slide is used to deflect the ultrasound (US) signal towards the US transducer. The red dashed line shows the separation between proximal side and sample side. The imaging tip is free of any optical element or transducer, allowing minimally invasive endoscopy.

3.2.1 - Digital phase conjugation through capillary waveguide characterization

The CWG supports a large number of modes. These modes, during propagation, will generate a quasi-random speckle pattern at the end of the waveguide. As explained before, by properly shaping the light using a SLM it is possible to create a focus spot on one end of the CWG. A calibration step is needed to determine the required wavefront.

The implementation of DPC in CWGs shows some differences compared to the case of MMFs. When the calibration beam is focused on the plane of the capillary facet, two

possible situations can happen: the beam is focused on the silica annular part or on the hollow core of the capillary. In the first case, the light is guided to the other side of the capillary, and exits as a speckle pattern (Figure 3.4(a)) that can be recorded and phase conjugated, recreating a focus spot at the original position. The guiding mechanism in this case is total internal reflection, and the size of the phase conjugated spot is given by the maximum angle the optical waveguide can accept (i.e. the NA). Figure 3.4(b) shows that it is possible to scan a focused spot of full width at half maximum (FWHM) of $1.25\ \mu\text{m}$ in a regular grid in the area delimited by the silica walls of the CWG.

On the other hand, if the calibration beam is focused at the hollow core of the CWG, almost no light is going to reach the other side of the waveguide. As shown in Figure 3.4(c), light cannot be coupled into the silica part since only radiation modes can be excited in this configuration. Low order spatial modes, instead, are reflected with higher reflectivity and exit the center of the CWG at the proximal side: digital phase conjugation of the recorded field can thus form a focused spot with a lower NA (Figure 3.4(d)).

In order to obtain a regular grid of focused spots with high NA also at the center of the CWG, some working distance (WD) has to be added between the CWG facet and the focusing plane (Figure 3.4(e)). This is useful especially for photoacoustic imaging where the best US signal collection is obtained when the sample is aligned to the hollow core of the CWG (the acoustic waveguide). Focusing far from the CWG facet and letting the calibration beam diffract for a certain distance, allows us to illuminate the silica part of CWG, generating a high-resolution speckle pattern at the proximal side. This leads to the generation of a regular grid of spots with a large field of view, as shown in Figure 3.4(f) (the center of the grid corresponds to the center of CWG, the FWHM of the spots is on average $1.5\ \mu\text{m}$, scale bar $50\ \mu\text{m}$).

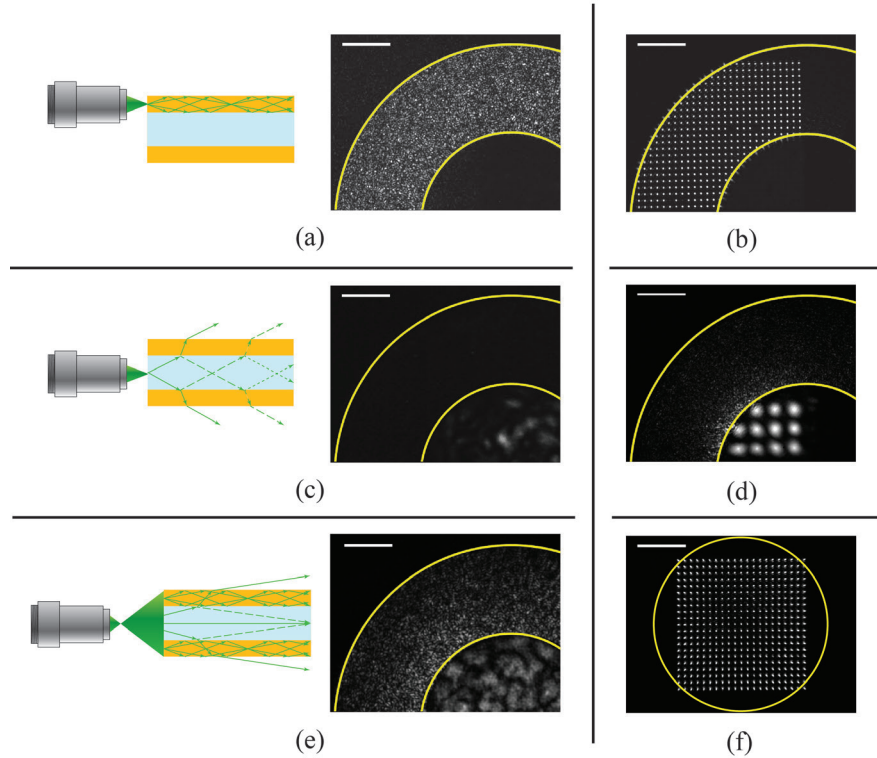


Figure 3.4: **Digital phase conjugation through capillary waveguides.** (a) During the calibration step, when light is focused directly in the silica part of the CWG, the light gets coupled to the propagation modes of the optical waveguide, so the optical field that exits the CWG on the other side will have a maximum spatial frequency given by the NA of the CWG. The field can be phase conjugated by using an SLM and sent back in the same location, forming a sharp focus; (b) Calibrating the endoscope in several positions it is possible to focus and scan a focus spot with a FWHM = 1.25 μm in a regular grid; (c) Focusing on the hollow core of the CWG, light cannot be coupled into the silica waveguide: light with low propagation angles is reflected better than the one with high angles, which gets lost into radiation modes. The field that exits the CWG has a small spatial spectrum, so the phase conjugated spot has a NA lower than the one of the CWG; (d) Focusing and scanning of a focus spot with a FWHM = 8 μm at the center of CWG; (e) Focusing in a plane at some distance from the capillary facet, it is possible to couple light in the silica part of the CWG even when the objective is focusing at the center of the CWG; (f) A 1.5 μm focused spot is scanned in a regular grid over a $130 \times 130 \mu\text{m}^2$ field of view in a plane 500 μm away from the facet of the CWG. The center of the grid corresponds to the center of the CWG. The elongated shape of the spots on the sides of the grid is given by a not perfect collection of the light during the calibration step. The calibration beam is partially coupled into the CWG due to the working distance and its relative position respect to the CWG. This affects the NA of the spot that can be phase conjugated. (b), (d) and (f) were formed superimposing images of spots focusing at different locations. The exposure time of (d) is 10 times the one used to acquire (b). Scale bars are 50 μm .

The introduction of the WD does not come without a cost. The focused spots at the edges are elongated along the radial direction. The observed aberrations become worse for spots further away from the center of the CWG. This is due to the fact that the calibration beam, when is focusing at the extremities of the scanning range, partially misses the CWG. Figure

3.5(a) shows the portion of the CWG illuminated during the training step when the calibration beam was focusing in the highlighted positions. During the focusing step by DPC, this results in a reduced NA along a preferential direction, which leads to the elongated shape of the focus spots. A beam propagation method (BPM [24]) simulation of the DPC focusing process, shows the same elongated shape when the focusing plane is $500\ \mu\text{m}$ away from the CWG facet (Figure 3.5(b)). Knowing the shape of the focused spots, deconvolution algorithms can be used to compensate for the aberration induced by the system.

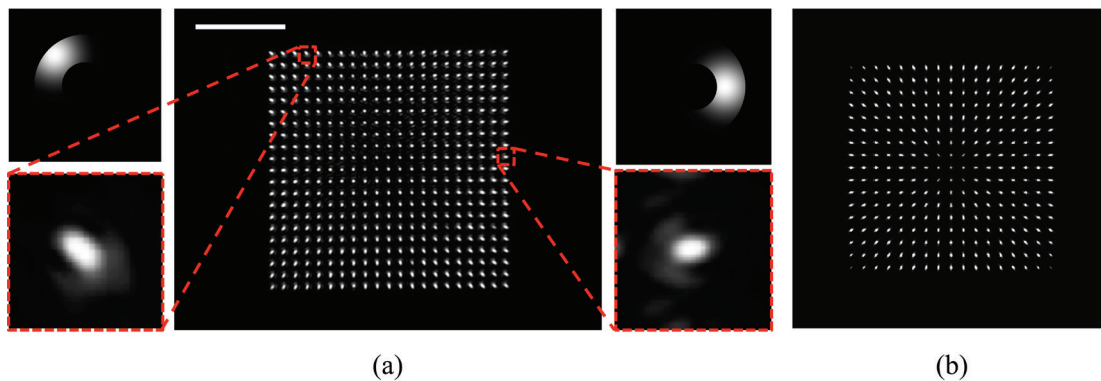


Figure 3.5: **Digital phase conjugation through capillary waveguides: simulation.** When the calibration beam is focused in a plane at some distance from the CWG, light is coupled also in annular part, allowing the generation of sharp focus spots in front of the hollow part of the CWG. (a) A $1.5\ \mu\text{m}$ spot is scanned in a regular grid $500\ \mu\text{m}$ away from the CWG facet. The central spot in the grid corresponds to the center of the CWG. The elongated shape of the focus spots on the side of the grid is due to the partial collection of the expanded calibration beam by the CWG, that reduces the NA of the phase conjugated spot along a specific direction. (b) Beam propagation method simulations confirmed the correlation between elongated shape and limited collection of the calibration beam. Scale bar is $50\ \mu\text{m}$.

3.3 - Results and Discussion

3.3.1 - Fluorescence imaging

We first demonstrated that the CWG is used as a fluorescence endoscopic device. A computer is used to synchronize the projection of phase conjugated patterns on the SLM and the fluorescence signal acquisition by the CMOS. For this experiment we use a $30\ \text{mm}$ -long capillary (Polymicro Technologies, TSU100375, USA). In Figure 3.6 we present imaging of fluorescent polystyrene beads with a diameter of $1.5\ \mu\text{m}$ in average, deposited on a glass slide. The fluorescent beads are scanned by focusing spots with the FWHM of $1.5\ \mu\text{m}$ in average at the imaging tip of the CWG, as shown in Figure 3.4(f). The number of scanning points is 100×100 , the step size is $0.31\ \mu\text{m}$, and the field of view is $31 \times 31\ \mu\text{m}^2$. The acquired fluorescence image has been convolved with a Gaussian filter and resampled to minimize pixelation effects (Figure 3.6(a)). The cross-sectional plot in Figure 3.6(c) shows that two beads $2.2\ \mu\text{m}$ apart could be completely resolved. The comparison between the fluorescence

image in Figure 3.6(a) and the white light optical image in Figure 3.6(b) shows one to one correspondence demonstrating the imaging ability of the CWG used as the fluorescence endoscopic device.

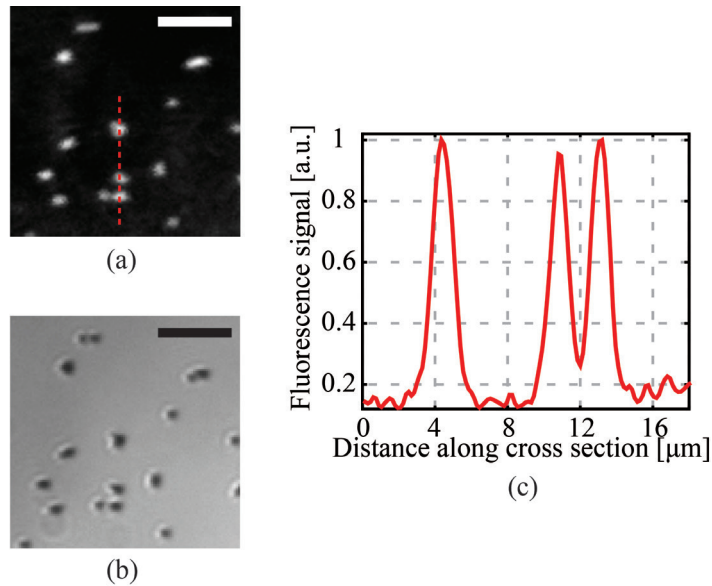


Figure 3.6: **Demonstration of high-resolution fluorescence imaging through capillary waveguides.** (a) Fluorescence image of 1.5 μm beads in a plane 100 μm away from the CWG facet. The sample is placed in front of the silica part of the CWG in order to maximize resolution and signal collection. The FWHM of the spot is 1.5 μm and the scanning step is 0.31 μm ; (b) white light optical image of the sample; (c) cross-sectional plot along the red dashed line in (a) shows that two beads 2.2 μm far apart were completely resolved, giving an upper limit for the resolution of the fluorescence endoscope of about 2 μm . Scale bar are 10 μm .

The curve in Figure 3.7 shows how the collection efficiency of the fluorescence signal varies as a function of the WD. The insets show how the loss in signal strength results in reduced signal-noise-ratio.

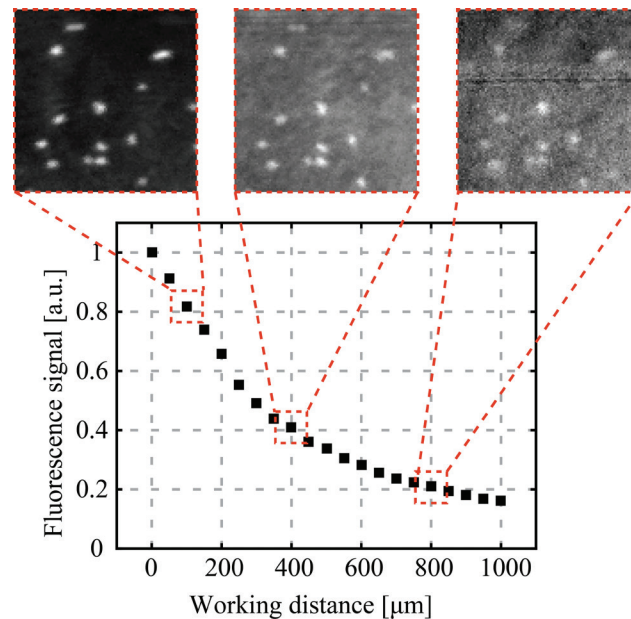


Figure 3.7: **Collection efficiency of the capillary waveguide as a function of the working distance.** Light is focused using DPC on a fluorescent bead and collected through the CWG. To generate a point in the curve, all the collected signal was integrated. Focus spots can be created very far away from the CWG, but the quality of the fluorescence images degrades due to decrease in collection efficiency.

3.3.2 - Photoacoustic imaging

We also demonstrate the use CWGs as a photoacoustic endoscopic device. For this experiment, we use a 25 mm-long capillary (Polymicro Technologies, LTSP150375, USA) as a CWG. The capillary used in this case has an inner diameter of 150 μm instead of 100 μm , so that the acoustic collection efficiency is optimized [23]. When we performed DPC in water, we saw a slight increase in the phase conjugated spot size due to a not perfect collection of the speckle pattern coming from the CWG during the calibration step. Figure 3.8 shows the size of the phase conjugated spot as a function of distance when focusing is performed in front of the hollow core or in front of the silica annular core.

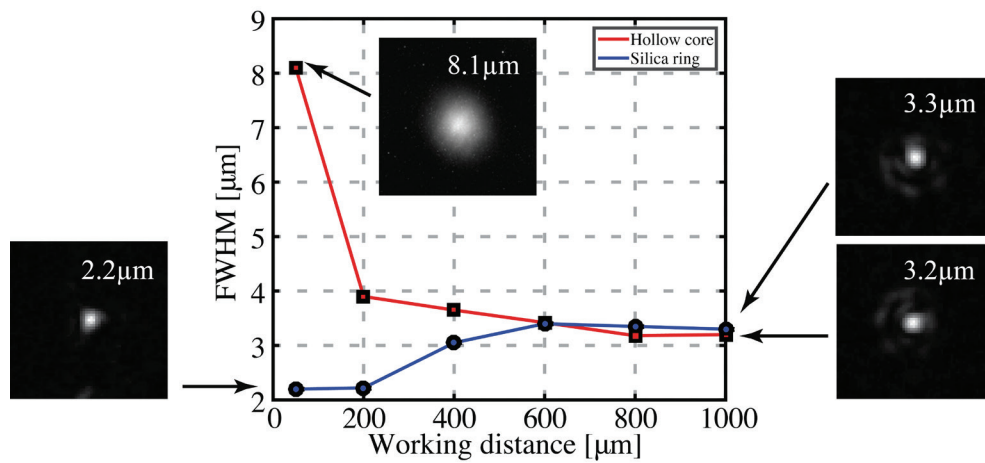


Figure 3.8: **Phase conjugated spot size in water as a function of the working distance.** The reduction of the size of the spot in front of the hollow core is obtained increasing the working distance. In this case, light is coupled into the propagation modes of the annular core of the CWG and a spot can be created with high NA. The size of the spot in front of the silica part is determined by the equivalent NA of the waveguide as a function of focusing position, as described by Papadopoulos et al.[25].

Although better performances are obtained in front of the silica region, the sample has to be placed in front of the hollow core to be able to optimally collect the photoacoustic signal. There is a tradeoff between resolution and amount of photoacoustic signal detected. In fact, further the sample is from the CWG, lower is the signal collected by the US transducer. At the same time, focus spots created close to the CWG have a larger FWHM compared to the ones at larger working distances.

In Figure 3.9 we first characterize the PA signal collection while focusing using DPC. The sample is a homogeneously absorbing 23 μm-thick layer of red polyester (color film 60193, Réfectiv, France). Figure 3.9(a) and Figure 3.9(b) respectively show time domain PA signals and their spectra depending on the distance between the sample and the distal tip of the CWG. The images show that the time trace of the signal does not change depending on the WD (apart from shifting in time), but just attenuates with a decrease in signal to noise ratio (SNR). Thus, the frequency content is kept, so no information is lost by the acoustic waveguide in the CWG due to the WD, unless the signal becomes too weak compared to the noise level.

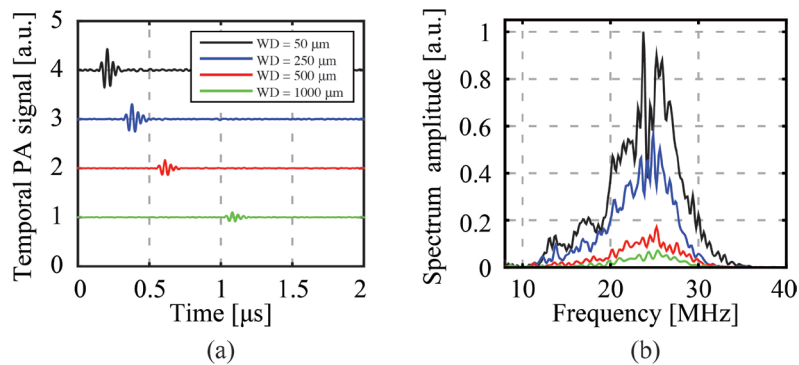


Figure 3.9: **Characterization of photoacoustic signal collection using the capillary waveguide.** (a) Photoacoustic signals acquired placing the sample at different distances from the CWG tip. Each position along the y-axis corresponds to a different acquisition. (b) Spectral components of the signals shown in (a). The pulse repetition rate of the laser was set to 200 Hz. The pulse energy at each phase conjugated spot was estimated at 500 nJ/pulse.

In Figure 3.10 we demonstrate optical-resolution photoacoustic imaging of a 30 μm diameter black nylon thread (NYL02DS, Vetsuture, France). In the experiment the number of scanning points is 64×64 , the step size is 3.45 μm , and the field of view is $220 \times 220 \mu\text{m}^2$.

As described before, a long WD gives a high NA focus spot at the center of the endoscope. At the same time, the signal collection becomes more homogeneous for a larger field of view, but the signal to noise ratio decreases as well. In Figure 3.10(b), the nylon thread is imaged at $WD = 1000 \mu\text{m}$ and the plot is the cross-section of the PA image along the red dashed line (Figure 3.10(c)). The resolution of the image is given by the size of the optical phase conjugated spot, which was on average 3 μm throughout the imaging plane, but the long distance from the CWG gives a noisy image due to the low SNR of the PA signal.

The SNR can be improved placing the sample closer to the CWG, at the expenses of the image resolution. In Figure 3.10(d), the nylon thread is imaged at $WD = 50 \mu\text{m}$. The phase conjugated spot was measured to have $FWHM = 2.2 \mu\text{m}$ in the silica region and 8 μm at the center of the CWG (see the red curve in Figure 3.8). The arrows in the PA image in Figure 3.10(d) point at two areas where the signal collection was limited by the presence of the silica walls of the capillary.

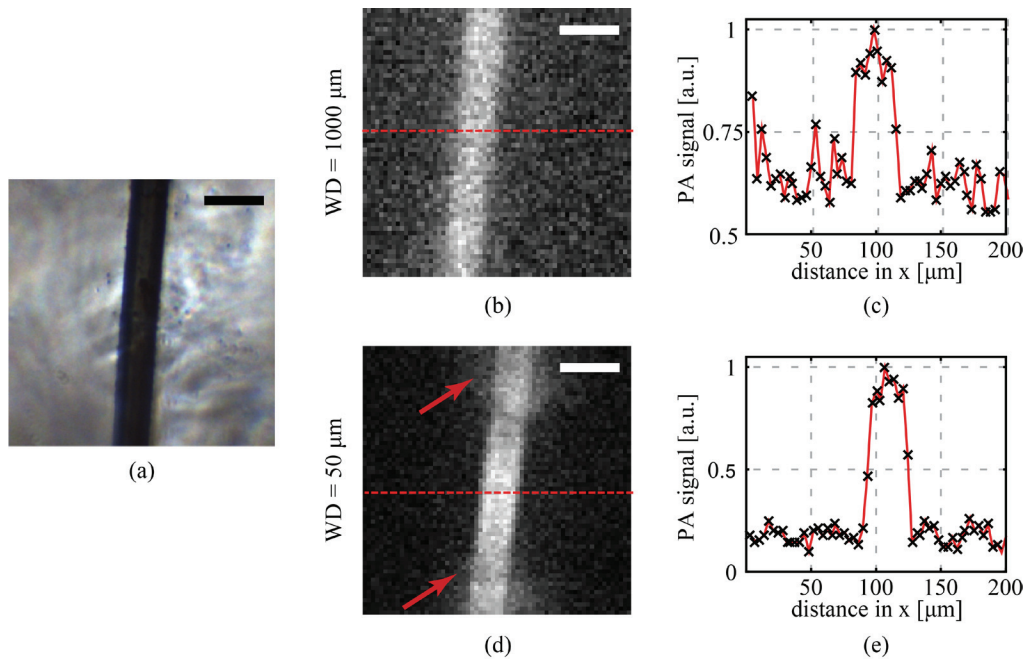


Figure 3.10: **Optical resolution photoacoustic imaging through capillary waveguides.** (a) A black nylon thread (30 μm in diameter) was used as absorber. Digital phase conjugation was used to digitally focus and scan a pulsed laser beam over a field of view of 220×220 μm². (b) Optical resolution photoacoustic image of the same sample placed at a working distance (WD) of 1000 μm. Due to the distance, the collection of the US waves is homogeneous within the whole field of view. Since at high WD it is possible to scan with the same high-resolution in the entire imaging plane, the resolution obtained in this case is the best attainable for photoacoustic imaging at the center of the CWG. The transition from background to signal is between 1 and 2 pixels, as shown in (c). (d) At WD = 50 μm it was possible to obtain an image of the thread with a better SNR (10). The two arrows indicate two areas where the collection was limited by the proximity of the sample to the CWG. (e) The cross-section of (d) shows a transition from background to signal between 2 and 3 pixels, giving an upper limit for the resolution around 10 μm. At the center of the CWG in fact, for short WDs, the phase conjugated spot has a low numerical aperture. Scale bars are 50 μm.

3.4 - Conclusions

In this chapter we have shown that CWGs can be used not only as a sensor or biosensor, but also as an imaging device, which can bring advantages to minimally invasive endoscopy. We have demonstrated that an ultrathin capillary waveguide can be used as a fully passive imaging device for fluorescence and photoacoustic imaging. Wavefront shaping combined with the possibility to use the CWG as an acoustic and optical multimode waveguide, can be seen as a powerful solution to focus light deep in tissue, picking up fluorescence and photoacoustic signals, while being at the same time minimally invasive.

A custom-made CWG with an optimized hollow core size and silica walls thickness would allow to make the two measurements at the same time. This will lead to a rigid endoscopic device that measures only 330 μm in diameter. The possibility of acquiring through the same endoscope fluorescence and photoacoustic signal can give complementary

information about the interrogated sample. This can be extremely helpful, for example, in case of early-stage cancer diagnosis. The fluorescence contrast images can give information about the morphology of the cells. At the same time, an absorption map of the tissue can be obtained using the photoacoustic capability, which can give high contrast label-free images of tumor masses, tissue vascularization and blood saturation.

Optical resolution photoacoustic imaging was demonstrated by imaging a 30 μm nylon thread. In order to maximize the US signal collection, the sample had to be placed right in front the hollow core. For small working distances it is possible to focus a low NA focus spot, obtaining a resolution below 10 μm , and reconstructing an image by collecting US waves through the same CWG. It is possible to obtain high NA focused spots in the entire imaging plane by increasing the working distance, so an image with a better resolution can be obtained at the cost of a lower signal to noise ratio. One possible solution to this problem and also reduce the working distance is to increase the NA of the optical waveguide, or changing the materials composing the CWG or introducing a scattering layer at the imaging tip [26], [27]. The second option would increase the photoacoustic imaging capability at the expenses of the fluorescence imaging, since the fluorescence collection efficiency will decrease.

Moreover, engineering the light and acoustic guidance properties of the CWG, and integrating the device with an acoustic beam splitter as in [28] and [29], would improve the acoustic signal collection and detection efficiency. A Teflon coated CWG with an inner diameter larger than the ones commercially available (150 μm for example) would also improve the endoscope. In fact Teflon coated capillaries have the peculiarity of guiding light also in the liquid core when filled with water. This happens because the cladding has a refractive of 1.31, which is lower than the water's one (1.33). At this point no WD is needed and a high NA focus spot can be formed everywhere in front of the CWG.

Bibliography

- [1] P. Beard, “Biomedical photoacoustic imaging,” *Interface Focus*, vol. 1, no. 4, pp. 602–631, Aug. 2011.
- [2] L. V. Wang and S. Hu, “Photoacoustic Tomography: In Vivo Imaging from Organelles to Organs,” *Science*, vol. 335, no. 6075, pp. 1458–1462, Mar. 2012.
- [3] I. N. Papadopoulos *et al.*, “Optical-resolution photoacoustic microscopy by use of a multimode fiber,” *Appl. Phys. Lett.*, vol. 102, no. 21, p. 211106, May 2013.
- [4] O. Simandoux *et al.*, “Optical-resolution photoacoustic imaging through thick tissue with a thin capillary as a dual optical-in acoustic-out waveguide,” *Appl. Phys. Lett.*, vol. 106, no. 9, p. 094102, Mar. 2015.
- [5] N. Stasio *et al.*, “Towards new applications using capillary waveguides,” *Biomed. Opt. Express*, vol. 6, no. 12, pp. 4619–4631, Dec. 2015.
- [6] N. Stasio *et al.*, “Fluorescence and optical-resolution photoacoustic imaging through capillary waveguides,” 2016, vol. 9717, p. 97171H–97171H–8.
- [7] O. S. Wolfbeis, “Capillary waveguide sensors,” *TrAC Trends Anal. Chem.*, vol. 15, no. 6, pp. 225–232, Jun. 1996.
- [8] M. Borecki, M. L. Korwin-Pawlowski, M. Beblowska, J. Szmidt, and A. Jakubowski, “Optoelectronic Capillary Sensors in Microfluidic and Point-of-Care Instrumentation,” *Sensors*, vol. 10, no. 4, pp. 3771–3797, Apr. 2010.
- [9] B. A. Flusberg, E. D. Cocker, W. Piyawattanametha, J. C. Jung, E. L. M. Cheung, and M. J. Schnitzer, “Fiber-optic fluorescence imaging,” *Nat. Methods*, vol. 2, no. 12, pp. 941–950, Dec. 2005.
- [10] G. Oh, E. Chung, and S. H. Yun, “Optical fibers for high-resolution in vivo microendoscopic fluorescence imaging,” *Opt. Fiber Technol.*, vol. 19, no. 6, Part B, pp. 760–771, Dec. 2013.
- [11] H. F. Zhang, K. Maslov, G. Stoica, and L. V. Wang, “Functional photoacoustic microscopy for high-resolution and noninvasive in vivo imaging,” *Nat. Biotechnol.*, vol. 24, no. 7, pp. 848–851, Jul. 2006.
- [12] K. Maslov, G. Stoica, and L. V. Wang, “In vivo dark-field reflection-mode photoacoustic microscopy,” *Opt. Lett.*, vol. 30, no. 6, p. 625, Mar. 2005.
- [13] P. Shao, W. Shi, P. Hajireza, and R. J. Zemp, “Integrated micro-endoscopy system for simultaneous fluorescence and optical-resolution photoacoustic imaging,” *J. Biomed. Opt.*, vol. 17, no. 7, pp. 0760241–0760244, 2012.
- [14] K. Maslov, H. F. Zhang, S. Hu, and L. V. Wang, “Optical-resolution photoacoustic microscopy for in vivo imaging of single capillaries,” *Opt. Lett.*, vol. 33, no. 9, p. 929, May 2008.
- [15] Z. Xie, S. Jiao, H. F. Zhang, and C. A. Puliafito, “Laser-scanning optical-resolution photoacoustic microscopy,” *Opt. Lett.*, vol. 34, no. 12, p. 1771, Jun. 2009.
- [16] P. Hajireza, W. Shi, and R. J. Zemp, “Label-free in vivo fiber-based optical-resolution photoacoustic microscopy,” *Opt. Lett.*, vol. 36, no. 20, p. 4107, Oct. 2011.
- [17] J.-M. Yang, K. Maslov, H.-C. Yang, Q. Zhou, K. K. Shung, and L. V. Wang, “Photoacoustic endoscopy,” *Opt. Lett.*, vol. 34, no. 10, p. 1591, May 2009.
- [18] J.-M. Yang *et al.*, “A 25-mm diameter probe for photoacoustic and ultrasonic endoscopy,” *Opt. Express*, vol. 20, no. 21, p. 23944, Oct. 2012.

Chapter 3 – Fluorescence and optical-resolution photoacoustic imaging through capillary waveguides using digital phase conjugation

- [19] J.-M. Yang *et al.*, “Optical-resolution photoacoustic endomicroscopy in vivo,” *Biomed. Opt. Express*, vol. 6, no. 3, p. 918, Mar. 2015.
- [20] P. N. T. Wells, “Ultrasonic imaging of the human body,” *Rep. Prog. Phys.*, vol. 62, no. 5, p. 671, May 1999.
- [21] B. E. A. Saleh and M. C. Teich, *Fundamentals of Photonics*. Wiley, 2013.
- [22] D. T. Blackstock, *Fundamentals of Physical Acoustics*. John Wiley & Sons, 2000.
- [23] O. Simandoux, “Photoacoustic imaging: contributions to optical-resolution photoacoustic endoscopy and experimental investigation of thermal nonlinearity,” PhD Thesis, Université Paris Diderot Paris 7, Paris, France, 2015.
- [24] K. Okamoto, *Fundamentals of Optical Waveguides*. Academic Press, 2010.
- [25] I. N. Papadopoulos, S. Farahi, C. Moser, and D. Psaltis, “High-resolution, lensless endoscope based on digital scanning through a multimode optical fiber,” *Biomed. Opt. Express*, vol. 4, no. 2, p. 260, Feb. 2013.
- [26] I. N. Papadopoulos, S. Farahi, C. Moser, and D. Psaltis, “Increasing the imaging capabilities of multimode fibers by exploiting the properties of highly scattering media,” *Opt. Lett.*, vol. 38, no. 15, p. 2776, Aug. 2013.
- [27] Y. Choi, C. Yoon, M. Kim, J. Yang, and W. Choi, “Disorder-mediated enhancement of fiber numerical aperture,” *Opt. Lett.*, vol. 38, no. 13, p. 2253, Jul. 2013.
- [28] S. Hu, P. Yan, K. Maslov, J.-M. Lee, and L. V. Wang, “Intravital imaging of amyloid plaques in a transgenic mouse model using optical-resolution photoacoustic microscopy,” *Opt. Lett.*, vol. 34, no. 24, p. 3899, Dec. 2009.
- [29] S. Hu, K. Maslov, and L. V. Wang, “Second-generation optical-resolution photoacoustic microscopy with improved sensitivity and speed,” *Opt. Lett.*, vol. 36, no. 7, pp. 1134–1136, Apr. 2011.

Chapter 4

Enhanced resolution in a multimode fiber imaging system

Capillary multimode waveguides and multimode optical fibers have been demonstrated to be a promising candidate for ultrathin and high-resolution endoscopy. However, the imaging modalities demonstrated to date do not offer depth discrimination for fluorescence imaging, and, at the same time, the numerical aperture of the fiber limits the achievable resolution. In this chapter we demonstrate optical sectioning and enhanced resolution using saturated excitation and temporal modulation. Using a continuous wave laser excitation, we demonstrate improved resolution in all three dimensions and increased image contrast by rejecting out of focus light. The material presented in this chapter has been published in [1]:

- G. P. J. Laporte*, **N. Stasio***, C. Moser, and D. Psaltis, “Enhanced resolution in a multimode fiber imaging system,” *Opt. Express*, vol. 23, no. 21, pp. 27484–27493, Oct. 2015.

* Equally contributing authors

4.1 - Introduction

As discussed in previous chapters, MMFs yield higher resolution imaging compared to optical fiber bundles in a reduced cross section [2]–[6]. Nevertheless, the resolution of the MMF image is limited by the relatively small numerical aperture of the fiber (NA typically between 0.2 and 0.5) [6], [7].

The numerical aperture of the multimode fiber endoscope system can be increased by using a thin layer of scattering material [8], [9] or with micro-fabricated optics [10] in front of the fiber. In this case only the lateral resolution of the MMF imaging system would increase. At the same time, the ability to reject out of focus light is also important, especially when it is critical to discriminate structural features in a thick sample. Fiber-based endoscopic sectioning has been obtained by implementing multi-photon imaging using fiber

bundles [11], [12]. Lensless, digital scanning two-photon endoscopy was also demonstrated with thin, custom-made bundles [13], [14]. The images in ref. [13] and [14] had a limited field of view (FOV) of about 50 μm and the imaging plane was 500 μm away from the fiber facet, which reduced the collection efficiency. Endoscopic sectioning can also be obtained by implementing confocal filtering. Confocal microendoscopy using a fiber bundle was demonstrated in 1996 [15]. Starting from the transmission matrix approach [16], confocal microscopy has been obtained through MMF applying a virtual pinhole or through optical correlation [17], [18]. The same technique could be extended to fluorescence imaging calculating or measuring the transmission matrix for the excitation and the emission wavelength. The excitation transmission matrix can be used to focus light, while the emission transmission matrix has to be utilized to retrieve the field emitted from the sample. For moderate NAs and centimeter-length step index MMFs, the bandwidth for which the detection transmission matrix would work is on the order of 1 nm [19], severely limiting fluorescence confocal imaging through MMFs.

Multi-photon excitation is widely used in microscopy to obtain depth sectioning. Multi-photon excitation requires the focusing of femtosecond pulses. Through MMFs this is possible compensating modal and chromatic dispersion as demonstrated recently [20]. In this chapter, we exploited nonlinearities in fluorescence response to achieve sectioning capabilities by using a continuous wave laser (CW) illumination. We use saturated excitation (SAX) [21] a nonlinear method used for high-resolution microscopy and we harness it to imaging through MMFs. As in two-photon microscopy, the nonlinearity of the fluorescence response induced by SAX improves spatial resolution and introduces optical sectioning [21]–[23]. Furthermore, SAX is well matched to MMF imaging since it uses a CW laser with narrowband temporal modulation instead of femtosecond pulses, thereby bypassing the problem of modal and chromatic dispersion. Hence, using fluorescence saturation with CW excitation, we demonstrate ultrathin endoscopic imaging with an improved resolution compared to linear imaging. We also demonstrate that the depth discrimination provided by fluorescence saturation can improve the contrast of thick sample images.

4.2 - Working principle

This section aims at recalling the principle of resolution improvement and depth discrimination in SAX imaging. We also show that the geometry of MMF endoscopy by phase conjugation is compatible with SAX. As described in the previous chapters, fluorescence scanning imaging through MMFs is possible focusing and scanning a spot at the tip of the fiber by using digital phase conjugation (DPC). The fluorescence can be collected through the same fiber and integrated at every scanning position, resulting in a fluorescence map.

At low power, the effective intensity point spread function (PSF_{fiber}) is equal to the illumination intensity point spread function (PSF_{exc}):

$$PSF_{fiber}(r, z) = PSF_{exc}(r, z). \quad (4.1)$$

Let us consider a sinusoidally time modulation of the excitation intensity I_{exc} :

$$I_{exc}(t) = \frac{1}{2} I_{max} [1 + \cos(\omega t)]. \quad (4.2)$$

In case the maximum intensity I_{max} is not enough to induce fluorescence saturation, the time dependent fluorescence response from an interrogated sample, $I_{fluor}(t)$, will be proportional to $I_{exc}(t)$. In this case the frequency response of $I_{fluor}(t)$ (i.e. its Fourier transform) will contain a single peak at the frequency ω . At higher excitation intensities, saturated excitation of fluorescence molecules induces a nonlinear relationship between illumination and fluorescence response. At this point the fluorescence response $I_{fluor}(t)$ will be a saturated sinusoidal time function, so its spectrum will contain high order harmonics at 2ω , 3ω , etc. depending on I_{max} . The fluorescence signal obtained by demodulation of the n^{th} harmonic frequency is proportional to the n^{th} power of the excitation intensity (at the condition that the illumination intensity is low enough in order to not saturate the n^{th} harmonic) [21]–[24]:

$$PSF_{fiber,SAX^{mo}}(r,z) = [PSF_{exc}(r,z)]^n, \quad (4.3)$$

where ω is the frequency of the sinusoidal temporal modulation. Thus, as it can be seen in Figure 4.1(a), the effective excitation point spread function ($PSF_{fiber,SAX}$) is sharpened at the region around the peak where the saturation is maximum. The resolution of the contribution proportional to the n^{th} power of the excitation intensity, improves the linear imaging resolution by a factor of \sqrt{n} ([21], [22]).

Extracting the nonlinear fluorescence signal also provides depth discrimination [23]. This can be visualized by calculating the signal emitted as a fluorescent plane is axially translated through the PSF (Figure 4.1(b)). In case of single photon fluorescence, the signal emitted by a thin layer can be calculated as:

$$I_{layer}(z) = \int_{r=0}^{r=\infty} PSF_{exc}(r,z) dr. \quad (4.4)$$

The SAX demodulated signal from the n^{th} harmonic is given by:

$$I_{layer,SAX^{mo}}(z) = \int_{r=0}^{r=\infty} [PSF_{exc}(r,z)]^n dr. \quad (4.5)$$

Because of energy conservation, in the linear case (blue plot on Figure 4.1(b)), the signal is constant as a function of the axial position, illustrating the absence of sectioning. Instead, the integrated intensity of the SAX demodulated signal exhibits a peak in the focal plane (red and green plots in Figure 4.1(b)). This is the origin of optical sectioning capability in SAX microscopy. For this reason, demodulated saturated fluorescence signal can be recorded to obtain both improvement in resolution and depth discrimination.

Due to the difficulty of creating a thin homogeneous fluorescence layer, in order to evaluate the sectioning performances we consider the axial edge response of our imaging system ([25], [24]). It consists in measuring the fluorescence emitted by a thick layer of fluorophores (theoretically infinitely thick) as the excitation focus enters the sample. The edge response can be calculated as:

$$I_{edge, fiber}(z) = \int_{z'=-\infty}^{z'=z} \left\{ \int_r PSF_{exc}(r, z') dr \right\} dz', \quad (4.6)$$

$$I_{edge, 2^{nd} harmonic}(z) = \int_{z'=-\infty}^{z'=z} \left\{ \int_r [PSF_{exc}(r, z')]^2 dr \right\} dz'. \quad (4.7)$$

In the first case (blue curve in Figure 4.2), the fluorescence response is linear to the excitation. Assuming an infinitely thick dye layer, the edge response is constant. The red and the green curve in Figure 4.2 represent the edge response for SAX microscopy demodulating at frequency 2ω , and two-photon microscopy, respectively. The better sectioning performance in SAX microscopy is given by the shorter excitation wavelength.

We detail in the next section how is possible to implement SAX microscopy for MMF endoscopic imaging.

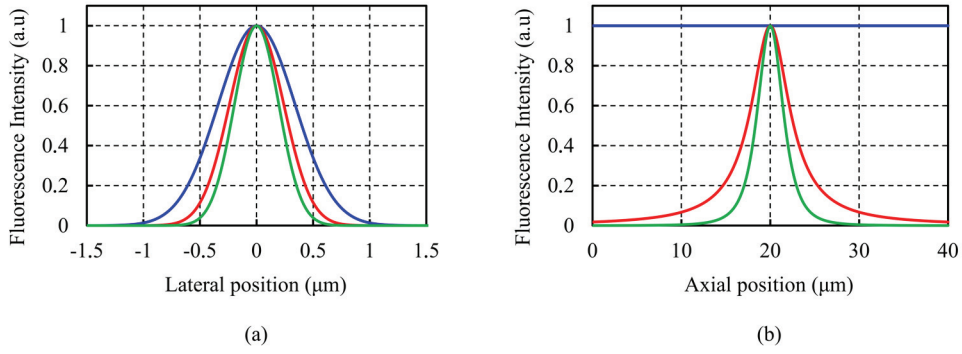


Figure 4.1: **Resolution improvement and optical sectioning in saturated excitation microscopy.** (a) Effective intensity PSF profile for linear imaging (blue) and for 2nd (red) and 3rd (green) harmonic demodulated saturated fluorescence signal. (b) Fluorescence signal as a perfect planar thin object is scanned axially. Linear case (blue) shows the absence of sectioning while the 2nd (red) and 3rd (green) harmonic SAX signal indicate depth discrimination. We assumed 0.39 NA and 532 nm excitation wavelength.

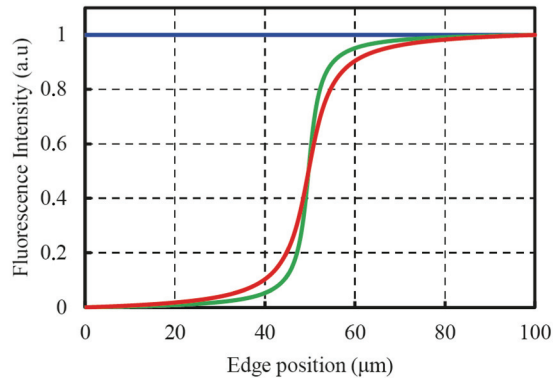


Figure 4.2: **Edge responses for a 0.39 NA scanning imaging system.** Blue curve, no optical sectioning ability; red curve, with two-photon fluorescence response; green curve, saturated fluorescence excitation microscopy response.

4.3 - Experimental setup

The schematic diagram of our experimental apparatus is shown in Figure 4.3. It is a modified version of the one presented in the previous chapter. As described before, the focused spot produced by the multimode fiber (0.39 NA, 200 μm core diameter, Thorlabs) is obtained by digital phase conjugation of the field recorded previously on the opposite side with the off-axis holographic setup. The sample is scanned to produce a fluorescence image. To implement SAX microscopy, the laser beam is modulated sinusoidally in time. At low excitation level, the fluorescence response depends linearly on the excitation. When the excitation intensity increases, the fluorescence response saturates and modifies the temporal response of the nanodiamonds. This leads to the formation of harmonics of the carrier frequency.

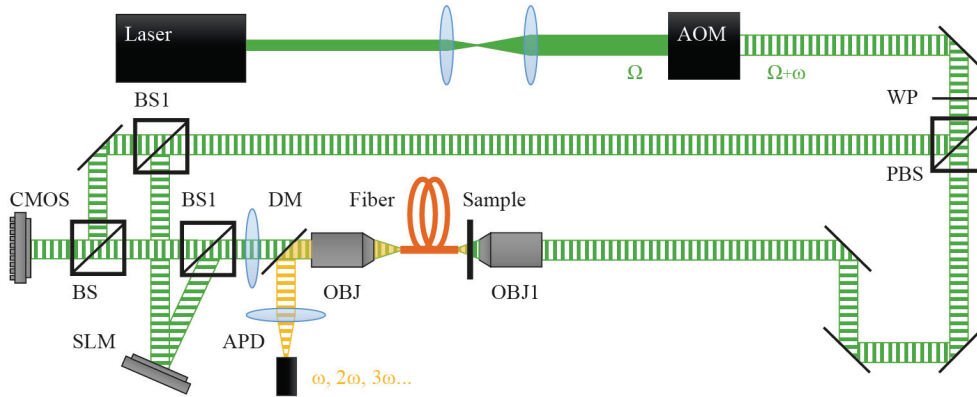


Figure 4.3: **Schematic of the imaging setup for saturated excitation endoscopy.** Light is focused on the fiber facet by an objective (OBJ) the speckled output interferes with the reference and the resulting interference pattern is digitally recorded onto the camera sensor (CMOS). The reconstructed phase of the hologram is assigned on the Spatial Light Modulator (SLM), which then modulates the high power arm of the reference beam. The phase conjugate beam propagates backwards recreating a focused spot in the initial position. This focused beam is used to excite the sample. To record a fluorescence image, the sample is scanned with a piezoelectric-stage and the light is collected back through the fiber, isolated with a dichroic mirror (DM) and detected with an avalanche photodiode (APD). The beam is modulated in time with an acousto-optic modulator (AOM) and for each scanning position a time trace of the fluorescence signal is recorded and then post-treated to isolate harmonics. (Other acronyms: WP: wave plate, PBS: Polarizing Beam Splitter, BS: 50/50 Beam Splitter, BS1: 90/10 Beam Splitter).

In the experiment the beam was sinusoidally modulated in time at $\omega = 2$ kHz with an acousto-optic modulator (AOM). The AOM is placed at the very beginning of the setup so that the induced Doppler shift does not affect the hologram acquisition. To accurately detect the saturated contribution, it is critical that the excitation modulation is a perfect sinusoid in order not to induce any signal at the harmonics frequency not associated to the saturation process. To do so, we calibrated the acousto-optic modulator response and drove it with a radio frequency generator able to envelop the 80 MHz sound wave with an arbitrary kHz modulation (AFG 3102C, Tektronix).

A substantial intensity (about 100 kW/cm^2) is necessary to obtain fluorescence saturation (see the results section), so a high power source (Verdi-V10, Coherent, $\lambda = 532 \text{ nm}$) is used and the losses are minimized. The phase only spatial light modulator is placed in the image plane of the facet of the fiber, but on a different optical path than the one used to record the hologram. This separation avoids the 75% loss of light induced by the (50/50) beam splitter in the previous arrangement [3]. Two (90/10) beam splitters are used to maximize the light sent onto the SLM which is used during the scan. The possibility of digitally scanning the beam by using a set of saved patterns has been demonstrated elsewhere ([3], [6]) and in the previous chapter. Here we keep a single phase conjugated excitation spot and we scan the sample with a piezoelectric stage. For each scanning position, the temporal response is recorded during 20 ms. The time trace for each scanning position is saved and by taking the Fourier transform, the value of the harmonics for each pixel is extracted off-line on a

computer. By averaging over several periods, the narrow band harmonic signals buried into the noise (spread over a wider spectrum) can be recovered.

4.4 - Results

For our experiments we utilized fluorescent nanodiamonds (120 nm diameter) as imaging probe [22]. They contain nitrogen vacancies defects that exhibit fluorescence that peaks at 670 nm and do not bleach even under high excitation intensity.

We first measured the nonlinear response of a single nanodiamond containing about 1000 nitrogen vacancies (Figure 4.4). From this curves the level of excitation intensity necessary to demodulate high harmonics and get high-resolution imaging can be determined. The noise is measured as the average value over all the frequencies apart from the modulation frequencies and its harmonics. The slope of the noise signal ($\propto\sqrt{I}$, yellow curve in Figure 4.4) indicates that shot noise was the main source of noise in the detection of nonlinear fluorescence signals. As reported previously [22], around 100 kW/cm², the saturation of the fluorescence response becomes significant enough to allow the extraction of the high harmonic signals. In order not to saturate the harmonic signal and to maximize the level of nonlinear signal compare the fundamental, we used about 60 kW/cm² for the second harmonic signal and 250 kW/cm² for the third harmonic signal.

In order to characterize the improvement in resolution given by this technique we recorded the PSF by scanning a single nanodiamond into the focused spot produced by the fiber with different excitation intensities.

It can be observed in Figure 4.5 that both the lateral and axial FWHM decrease with higher harmonics demodulation. We measured the linear lateral FWHM to be 850 nm (the diffraction limit is 700 nm for a 0.39 NA fiber). From the profiles on Figure 4.5(d) and Figure 4.5(e), the gain both in lateral and axial resolution is estimated to be about 1.6 with the third harmonic demodulation, close to the theoretical limit of $\sqrt{3}$. The images and the plots on Figure 4.5 are normalized. The higher harmonic frequency components have a signal intensity one to two orders of magnitude lower than the fundamental frequency component and the background that appears on the Figure 4.5(c) is due to shot noise.

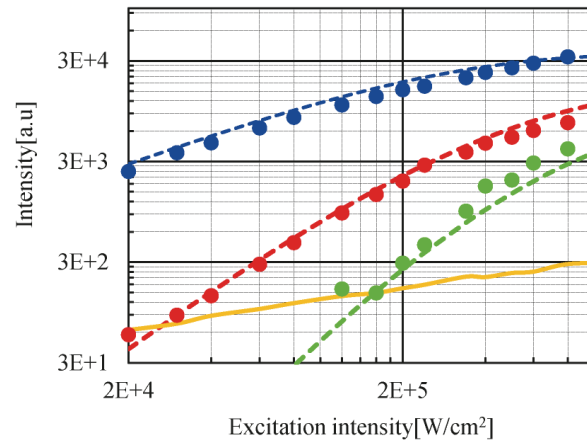


Figure 4.4: **Demodulated fluorescence signal intensity from nanodiamonds.** The blue points correspond to the fluorescence signal with demodulation at the fundamental frequency. The red dots to the second harmonic and the green ones to the third. The dashed curves are the theoretical response for a three level Jablonski diagram, considering an absorption cross section of 10^{-15} cm^2 and a fluorescence lifetime of 10 ns. The slopes at the beginning of the curve are respectively 1, 2 and 3 in logarithmic scale, illustrating the nonlinear fluorescence response that results in a gain in resolution. The noise level is taken as the average of the signal in all the frequencies but the harmonics, and represented by the yellow curve. Its slope of 0.5 is characteristic of Poisson noise (shot noise).

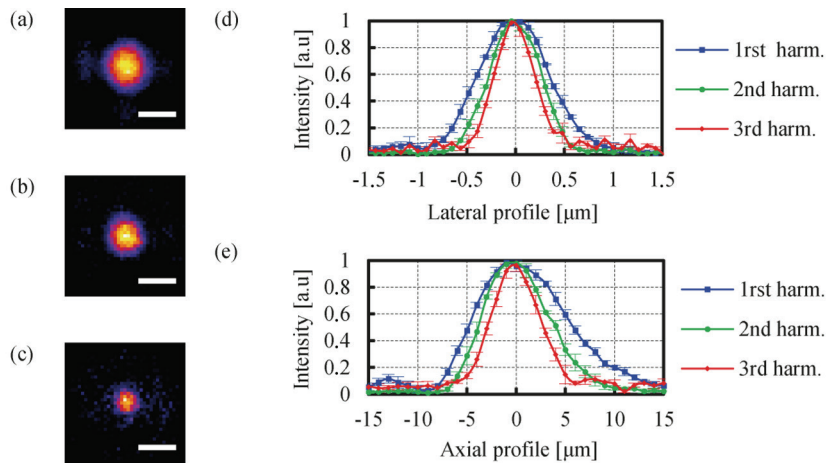


Figure 4.5: **Point spread function narrowing with saturated excitation endoscopy.** The PSF is measured by making a fluorescent scanning image of a single nanodiamond (with a diameter much smaller than the diffraction limit of the imaging system). Scale bars are $1 \mu\text{m}$. (a) Linear image in the focal plane obtained by demodulation at the modulation frequency. (b) Image with second harmonic demodulation (c) Image with third harmonic demodulation. (d) The intensity profiles along the images (a), (b) and (c). The effective point spread function FWHM, decreases as we use higher harmonics for demodulation. The gain in resolution is measured to be about 1.6 times for the third harmonic demodulation compared with the fundamental frequency. Each point on the plot is the average over 5 measurements obtained with different nanodiamonds, the error bars represent \pm the standard deviation. (e) The nanodiamond is also scanned in the axial dimension and the axial intensity profile are plotted. The same resolution improvement factor is obtained in the three dimensions.

In Figure 4.6, we illustrate the gain in resolving power due to SAX by imaging clusters of nanodiamonds immobilized on a glass slide. The fluorescent nanodiamonds were observed by extracting the third harmonic component. Comparison of the image formed at low light power at the fundamental frequency with the SAX image, confirms the improvement of the spatial resolution in SAX microscopy. Some details (arrows on Figure 4.6(b)) of the nanocrystals assembly, not visible with linear imaging, are resolved in the demodulated image. The resolution for the third harmonic is about 500 nm and it opens the path for microstructures observation with MMFs.

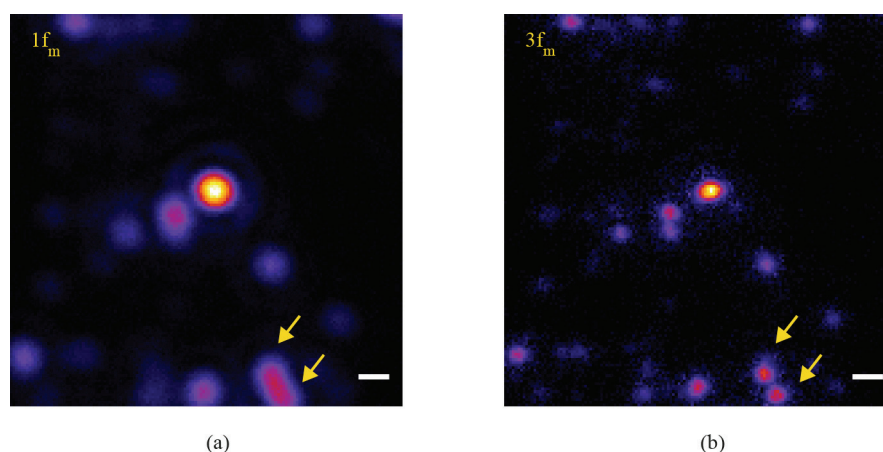


Figure 4.6: **Fluorescence images of nanodiamonds immobilized on a glass slide.** Scale bars 1 μm . (a) Linear image. (b) Saturated excitation image. The excitation intensities for those experiments were about 2 kW/cm^2 for (a) and 200 kW/cm^2 for (b).

As predicted by equation 4.2 and in Figure 4.1(b), SAX also achieves significant suppression of out-of-focus light in a similar manner as two-photon fluorescence microscopy [23]. The measurement of the axial edge response ([25], [24]) of our system confirms this depth-discrimination property. Figure 4.7(a) shows an experimental axial edge response, which is the fluorescence signal collected from a thick dye layer (Rhodamine 6G) while it is scanned along the optical axis. The linear response (blue plot) shows the absence of sectioning in the system but the demodulated signal (green plot) at the second harmonic exhibits the edge transition when the focus is entering the dye layer.

For a given fluorophore, the illumination wavelength is shorter in SAX (by a factor of 2 roughly) than in two-photon excitation imaging. As a result the excitation PSF is narrower because of the shorter wavelength. Correspondingly, the light used to form the image comes from a thinner section when we extract the second harmonic of the modulation in SAX. Furthermore the sectioning performance is not altered by the Stokes shift. It can be observed on the curve of Figure 4.7(a), that the slope of the transition with second harmonic demodulation is similar to the one given in a confocal microscope with a 0.4 NA objective and an infinitely small pinhole. However, the out of focus light rejection mechanism takes place in the digital domain and as we will detail in the conclusions section is bound to the available SNR.

We demonstrated that the image contrast can be improved with this method by scanning a sample composed of two layers of nanodiamonds separated by a 30 μm -thick transparent polymer (PDMS, Sylgard 184, Dow Corning). Background fluorescence light is generated by the out of focus layer but is not saturated. It can be observed on Figure 4.7(b) and Figure 4.7(c) that the background light is filtered out in the second harmonic demodulated signal and that the contrast of the image is improved. As with the edge response measurement, only the second harmonic demodulation could be recorded.

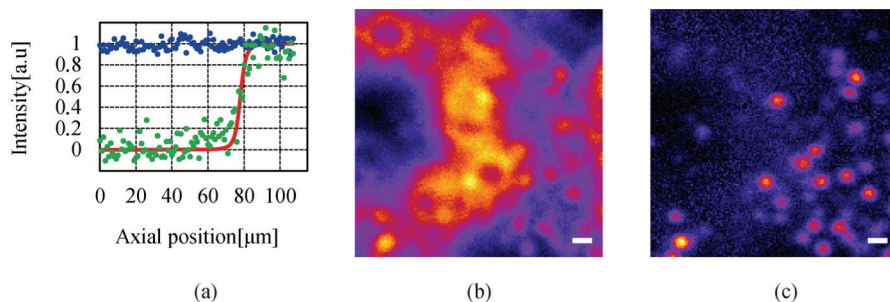


Figure 4.7: **Sectioning properties of saturated excitation microscopy.** Scale bars are 1 μm . (a) Edge response from a Rhodamine 6G solution, for linear excitation with demodulation at the excitation frequency (blue points), for saturated excitation with demodulation at the second harmonic (green points) and the theoretical edge response curve (red), equivalently for a linear detection with infinitely small pinhole or for second harmonic SAX demodulation. The integration time was 200 ms per point. (b) Fluorescent image through MMF of fluorescent diamonds: the image is blurred by out of focus signal coming from a cluster of nanodiamonds placed 30 μm deeper. (c) Saturated excitation image through MMF: second harmonic demodulation rejects out of focus signal and improves the contrast.

4.5 - Conclusions

In this chapter, we have demonstrated that saturated excitation in MMF scanning fluorescence microscopy can lead to resolution increase in all three dimensions. We measured an improvement in resolution by a factor of 1.6, which is close to the theoretical factor of resolution gain of 1.73. The available improvement in resolution can in principle be improved indefinitely by using higher harmonics of the modulation frequency, but the improvement is practically restricted by the available signal to noise ratio. As shown on Figure 4.4, the third harmonic signal is about 30 times lower than the DC component. With nonbleaching probes, the SNR could be improved by increasing the acquisition dwell time and improving detected signal, but this comes with the cost of imaging speed.

We also demonstrated that besides the resolution improvement, the advantage of saturated excitation imaging method is the ability to remove out of focus light. However, this property suffers from its inability to physically reject out-of-focus light before it reaches the detector. As opposed to two-photon absorption, saturated excitation creates fluorescence signal throughout the entire thickness. Then, the out of focus light rejection is obtained by isolating digitally the harmonics generated by the saturation. Thus, in the presence of out of focus light, the level of the high harmonics compared to the fundamental frequency signal is

reduced. As the system is shot noise limited, the stronger the out of focus signal is, the more severe the SNR conditions are for extracting the harmonics signals. Because of this limitation we demonstrated background rejection only with the second harmonic in the result section.

In the case of biological imaging, the staining is usually made of fluorescent proteins or anti-bodies, which are subject to photobleaching. For a typical dye, hundreds of kW/cm^2 excitation intensity is required to observe the saturation with the SAX method ([22]–[24]). Therefore, the main issue is whether the number of photons obtained at each pixel is large enough to probe the high demodulated harmonics. On optimized SAX microscope systems, high excitation intensity has been shown to be compatible with various biological samples [23], [24]. In this proof of concept experiment, we bypassed the problem by both using nonbleaching nanodiamonds and scanning the sample with a fast piezoelectric stage. In a real endoscope based on phase conjugation through multimode fiber, the limiting element in terms of scanning speed is the phase modulating element. The use of a digital micro-mirror device would allow modulation at kHz rates and would achieve the required speed [26]. The MMF collection efficiency here is also limited compared to microscope objectives. So, for biological imaging with this method, only the second harmonic demodulation is realistic.

Bibliography

- [1] G. P. J. Laporte, N. Stasio, C. Moser, and D. Psaltis, “Enhanced resolution in a multimode fiber imaging system,” *Opt. Express*, vol. 23, no. 21, pp. 27484–27493, Oct. 2015.
- [2] S. Bianchi and R. D. Leonardo, “A multi-mode fiber probe for holographic micromanipulation and microscopy,” *Lab. Chip*, vol. 12, no. 3, pp. 635–639, Jan. 2012.
- [3] I. N. Papadopoulos, S. Farahi, C. Moser, and D. Psaltis, “Focusing and scanning light through a multimode optical fiber using digital phase conjugation,” *Opt. Express*, vol. 20, no. 10, p. 10583, May 2012.
- [4] T. Čižmár and K. Dholakia, “Exploiting multimode waveguides for pure fibre-based imaging,” *Nat. Commun.*, vol. 3, p. 1027, Aug. 2012.
- [5] Y. Choi *et al.*, “Scanner-Free and Wide-Field Endoscopic Imaging by Using a Single Multimode Optical Fiber,” *Phys. Rev. Lett.*, vol. 109, no. 20, p. 203901, Nov. 2012.
- [6] I. N. Papadopoulos, S. Farahi, C. Moser, and D. Psaltis, “High-resolution, lensless endoscope based on digital scanning through a multimode optical fiber,” *Biomed. Opt. Express*, vol. 4, no. 2, p. 260, Feb. 2013.
- [7] R. N. Mahalati, R. Y. Gu, and J. M. Kahn, “Resolution limits for imaging through multi-mode fiber,” *Opt. Express*, vol. 21, no. 2, pp. 1656–1668, Jan. 2013.
- [8] I. N. Papadopoulos, S. Farahi, C. Moser, and D. Psaltis, “Increasing the imaging capabilities of multimode fibers by exploiting the properties of highly scattering media,” *Opt. Lett.*, vol. 38, no. 15, p. 2776, Aug. 2013.
- [9] Y. Choi, C. Yoon, M. Kim, J. Yang, and W. Choi, “Disorder-mediated enhancement of fiber numerical aperture,” *Opt. Lett.*, vol. 38, no. 13, p. 2253, Jul. 2013.
- [10] S. Bianchi, V. P. Rajamanickam, L. Ferrara, E. Di Fabrizio, C. Liberale, and R. Di Leonardo, “Focusing and imaging with increased numerical apertures through multimode fibers with micro-fabricated optics,” *Opt. Lett.*, vol. 38, no. 23, p. 4935, Dec. 2013.
- [11] M. T. Myaing, D. J. MacDonald, and X. Li, “Fiber-optic scanning two-photon fluorescence endoscope,” *Opt. Lett.*, vol. 31, no. 8, p. 1076, 2006.
- [12] D. R. Rivera *et al.*, “Compact and flexible raster scanning multiphoton endoscope capable of imaging unstained tissue,” *Proc. Natl. Acad. Sci.*, vol. 108, no. 43, pp. 17598–17603, Oct. 2011.
- [13] E. R. Andresen, G. Bouwmans, S. Monneret, and H. Rigneault, “Toward endoscopes with no distal optics: video-rate scanning microscopy through a fiber bundle,” *Opt. Lett.*, vol. 38, no. 5, p. 609, Mar. 2013.
- [14] E. R. Andresen, G. Bouwmans, S. Monneret, and H. Rigneault, “Two-photon lensless endoscope,” *Opt. Express*, vol. 21, no. 18, p. 20713, Sep. 2013.
- [15] A. F. Gmitro and D. Aziz, “Confocal microscopy through a fiber-optic imaging bundle,” *Opt. Lett.*, vol. 18, no. 8, p. 565, Apr. 1993.
- [16] S. M. Popoff, G. Lerosey, R. Carminati, M. Fink, A. C. Boccara, and S. Gigan, “Measuring the Transmission Matrix in Optics: An Approach to the Study and Control of Light Propagation in Disordered Media,” *Phys. Rev. Lett.*, vol. 104, no. 10, p. 100601, Mar. 2010.
- [17] D. Loterie, S. Farahi, I. Papadopoulos, A. Goy, D. Psaltis, and C. Moser, “Digital confocal microscopy through a multimode fiber,” *Opt. Express*, vol. 23, no. 18, pp. 23845–23858, Sep. 2015.

- [18] D. Loterie, S. A. Goorden, D. Psaltis, and C. Moser, “Confocal microscopy through a multimode fiber using optical correlation,” *Opt. Lett.*, vol. 40, no. 24, pp. 5754–5757, Dec. 2015.
- [19] D. Loterie, D. Psaltis, and C. Moser, “Confocal microscopy via multimode fibers: fluorescence bandwidth,” 2016, vol. 9717, p. 97171C–97171C–6.
- [20] E. E. Morales-Delgado, S. Farahi, I. N. Papadopoulos, D. Psaltis, and C. Moser, “Delivery of focused short pulses through a multimode fiber,” *Opt. Express*, vol. 23, no. 7, p. 9109, Apr. 2015.
- [21] K. Fujita, M. Kobayashi, S. Kawano, M. Yamanaka, and S. Kawata, “High-Resolution Confocal Microscopy by Saturated Excitation of Fluorescence,” *Phys. Rev. Lett.*, vol. 99, no. 22, p. 228105, Nov. 2007.
- [22] M. Yamanaka *et al.*, “SAX microscopy with fluorescent nanodiamond probes for high-resolution fluorescence imaging,” *Biomed. Opt. Express*, vol. 2, no. 7, pp. 1946–1954, Jun. 2011.
- [23] M. Yamanaka *et al.*, “Saturated excitation microscopy for sub-diffraction-limited imaging of cell clusters,” *J. Biomed. Opt.*, vol. 18, no. 12, pp. 126002–126002, 2013.
- [24] M. Yamanaka, S. Kawano, K. Fujita, N. I. Smith, and S. Kawata, “Beyond the diffraction-limit biological imaging by saturated excitation microscopy,” *J. Biomed. Opt.*, vol. 13, no. 5, pp. 050507–050507–3, 2008.
- [25] A. Diaspro, *Confocal and Two-Photon Microscopy: Foundations, Applications and Advances*. Wiley, 2001.
- [26] A. M. Caravaca-Aguirre, E. Niv, D. B. Conkey, and R. Piestun, “Real-time resilient focusing through a bending multimode fiber,” *Opt. Express*, vol. 21, no. 10, pp. 12881–12887, May 2013.

Chapter 5

Lensless two-photon imaging through a multicore fiber with coherence-gated digital phase conjugation

Although saturated excitation microscopy achieves three-dimensional imaging, it relies on high photostability of the sample. For this reason, in the previous chapter we utilized as a fluorescent probe nonbleaching nanodiamonds. In this chapter we show that regular staining agents, such as Rhodamine 6G, can be imaged in polystyrene beads and cells using two-photon microscopy through optical fibers. Instead of multimode fibers (MMFs), here we use a lensless multicore fiber. Respect to MMFs, each core of the MCF supports only few modes, so the multimode dispersion is minimized. Another advantage over MMFs is given by the fact that MCFs could perform dual imaging modalities, by functioning also as a widefield imager [1]. We show that the lensless MCF can perform near diffraction limited two-photon fluorescence (TPF) imaging utilizing digital phase conjugation (DPC). The phase conjugation technique is compatible with commercially available MCFs with high core density. Wavefront shaping applied to MCFs breaks the usual resolution limit imposed by the core-to-core spacing. We construct TPF images of fluorescent beads and cells by digital scanning of the phase conjugated focus on the target object and collection of the emitted fluorescence through the MCF.

The results presented in this chapter have been published in [2]:

- D. B. Conkey*, N. Stasio*, E. E. Morales-Delgado, M. Romito, C. Moser, and D. Psaltis, "Lensless two-photon imaging through a multicore fiber with coherence-gated digital phase conjugation," *J. Biomed. Opt.*, vol. 21, no. 4, p. 045002, Apr. 2016.

* Equally contributing authors

5.1 - Introduction

There is strong interest in developing high-resolution devices for internal, in vivo imaging. These tools would aid medical doctors and researchers in diagnosing and understanding many medical ailments, such as cancer, with a less invasive method than current practice. Multiphoton imaging [3] provides a useful tool for cellular imaging [4]–[9] and is widely used in brain [9] and biological imaging [4]–[7]. Like confocal microscopy, multiphoton imaging provides optical sectioning, which is necessary for imaging within thick tissue samples [4]. The compatibility between multiphoton imaging and biology is well known and a few endoscopic devices have been developed as a result [10]–[13]. Endoscopic devices for two-photon fluorescence (TPF) imaging generally utilize a single mode fiber for pulse delivery with mechanical components encased in a probe at the fiber’s distal tip to enable point scanning [11]–[13]. The scanning mechanism significantly increases the size of the endoscope over that of the light delivering fiber. While these devices are a significant improvement over existing technologies, a more compact TPF endoscope remains a desired goal.

To meet this goal, novel endoscopes utilizing specialty fibers and optics without distal optics or mechanics are being pursued. For example, commercial confocal endoscopes (not multiphoton) utilize a multicore fiber (MCF) for small diameter endoscopes [14], [15]. These devices scan light through the many cores of the fiber to sample the image at each core position at the distal end. The resolution of core by core scanning MCF endoscopes is limited by the core spacing [1], which must be kept sufficiently large to limit core-to-core coupling [16], [17]. The resolution can be improved with a graded index (GRIN) lens that demagnifies the fiber facet, however this improvement comes at the expense of a reduced field of view and the resolution is still limited by core spacing. This GRIN lens arrangement was used in a previous implementation of TPF imaging through a MCF [10]. More recently, MCFs have been utilized with wavefront shaping techniques to control the wavefront at the entrance of the fiber ([1], [18]–[20]) as done before with multimode fibers (MMFs) [21]–[24]. As explained in **Chapter 2**, the key difference between these methods are that in MMFs the modes provide the degrees of freedom in the light field control, whereas the fiber cores (and their modes) do in MCFs. With step-index MMFs these methods are restricted with regard to multiphoton microscopy due to modal dispersion of a propagating ultrashort pulse. The temporal spread of the modes as they propagate through the fiber limits the number that can contribute to a focus spot recreation [25]. However, GRIN-MMFs exhibit significantly less modal dispersion and it was recently demonstrated TPF imaging through one combined with a GRIN lens [26]. Using single mode MCFs bypasses the restrictions of modal dispersion, as well. Recently, a wavefront shaping method has been demonstrated with MCFs for multi-photon imaging [20]. The system developed by Andresen, et al. [20] uses a custom-fabricated MCF comprised of 169 highly-spaced, single-mode cores arranged in a hexagonal grid. With this fiber, the light field can be controlled with minimal core-to-core coupling. However, the large separation between periodically arranged cores resulted in

a close spacing between diffraction orders at the focal plane, thus limiting the field of view and forcing a large working distance which decreases resolution [20], [27].

In this chapter, we use wavefront shaping in conjunction with MCFs for two-photon fluorescence imaging. We utilize TPF imaging to enable optical sectioning in our lensless endoscope. To create the focus we use coherence-gated digital phase conjugation (DPC), as explained in **Chapter 2**. DPC compensates for core-to-core coupling [28] and allows for use of commercially available MCFs, which contain a large number (several thousand to 100,000) of densely packed cores arranged in a quasi-periodic array. The closely spaced cores spread the diffraction orders in the focal plane away from the desired focus which allows for a larger field of view than possible with highly spaced core MCFs [20] and also reduces the power distributed to the diffraction orders. While the MCF used propagates a few modes at our experimental wavelength, we show that a single mode can be selected through modal dispersion in the fiber and coherence-gating during hologram recording. We demonstrate that coherence-gated DPC allows for the selective propagation of individual modes and that the fundamental mode offers a better focusing performance when compared to the higher order mode. Finally, we construct TPF images by digital scanning of the phase conjugated focus on the target object and fluorescence collection through the MCF to obtain images of fluorescently stained beads and cells.

5.2 - Coherence-gated digital phase conjugation

DPC of ultrashort pulses with fibers allows for precise selectivity of the phase conjugated modes. To perform DPC, a calibrating focus spot is created at the distal end of the fiber. After propagation through the fiber, the field emerging from the proximal end is recorded using off-axis digital holography. The recorded field can then be phase conjugated digitally and coupled back into the fiber to recreate a focus spot at the original calibration position. In the case of coherence-gated DPC, the two pulses recording the hologram must overlap in space and time at the detector array. One pulse emerges from the MCF and the other is a reference wave. In most commercially available MCFs, each core supports the propagation of only a few modes. An ultrashort pulse propagating in a core will couple into the LP modes, which temporally separate as a result of modal dispersion. During the hologram recording, the short coherence length of the high bandwidth laser pulse coherence-gates the recording process. This allows for time-sampling the pulse after propagation through the MCF, recording the field of a selected set of modes after propagation through the fiber (see **Chapter 2**).

To test coherence-gated DPC through a MCF we use a commercially available fiber (Fujikura, FIGH-03-215S). This fiber has 3000 cores within a 190 μm diameter. Individual cores have a numerical aperture (NA) of 0.34 and are 2.5 μm in diameter on average and spaced by 3.2 μm on average. These cores have a V number of ~ 3.4 and support the LP_{01} and LP_{11} modes at 785 nm wavelength. These fibers are designed with a variation in core diameter to minimize core-to-core coupling [16]. The smaller core spacing separates the

diffraction orders in the far field which allows a wider field of view than possible with highly-spaced core MCF [19].

The optical system used for coherence-gated DPC is illustrated in Figure 5.1. The laser beam emitted from a Coherent Chameleon (3 W, 140 fs, operated at $\lambda = 785$ nm) is collimated and split into reference and calibration arms. The power ratio between the two arms is selected depending on whether the system is in a hologram recording or readout configuration. For these experiments a 30 cm length of MCF is mounted between two objectives separated by 28 cm, thus fixing the fiber with a slight curvature. Figure 5.1(a) illustrates the optical path during the hologram recording phase. To record a hologram light travels through both the reference and calibration arms. The light in the calibration path is focused in front of the distal end of the fiber. After collection and transmission through the MCF the light is imaged onto a CMOS detector (MV1-D1312IE-100-G2-12, Photonfocus) by an objective lens and a lens in a 4f configuration. The pulse which propagates through the reference path arrives on the CMOS and interferes with the calibration pulse. A delay line is placed in the reference path for tuning the temporal delay.

After recording, the phase of the field is extracted from the recorded hologram, phase conjugated, and displayed on the spatial light modulator (SLM, Pluto-NIR2, Holoeye). Figure 5.1(b) shows the optical path during the hologram readout phase. Two 90/10 beamsplitters (R/T) are used to read out the phase conjugate hologram displayed on the SLM to minimize the beamsplitter losses of the phase conjugated beam, as shown in **Chapter 4** and in [29]. On the distal end of the fiber the objective used to focus the calibration beam is used to capture the phase conjugated light which is then reimaged on a CCD (Point Grey Research, Chameleon 3) in order to check the quality of the DPC process.

Coherence-gated holography of the pulse allows an analysis of the temporal and spatial shape of the transmitted pulse from each core. The coherence-gating reference pulse can be treated as a sampling window in time. However, its sampling window size is not determined by the pulse length, but by the coherence length of the source because the interference measurement is not sensitive to spectral phase (i.e. to chromatic dispersion which broadens the pulse). In this way it probes the temporal coherence function of the pulses emerging from each core. Because coherence-gated holography provides the coherence function across the fiber facet, it provides information about pulse transmission from individual cores.

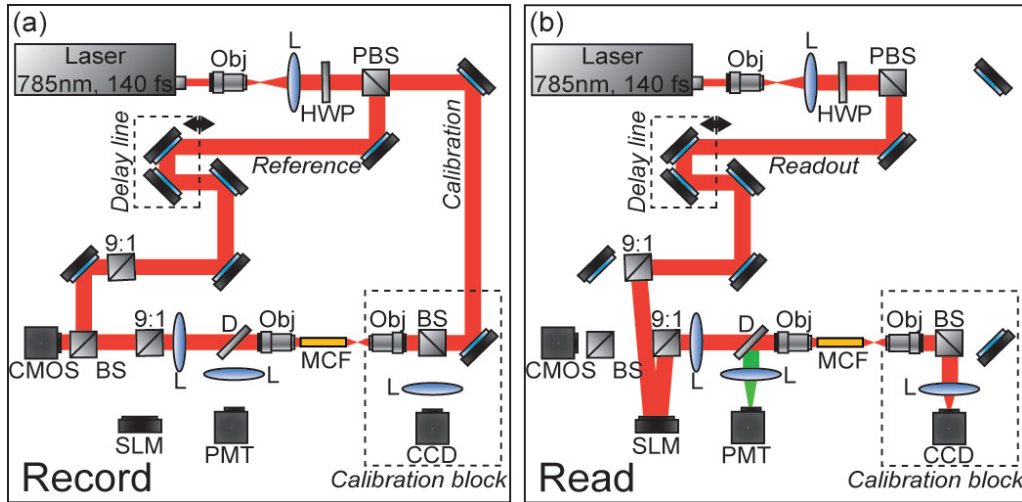


Figure 5.1: **The optical apparatus for coherence-gated digital phase conjugation with a multicore fiber.** The figures represent the optical apparatus in (a) hologram recording phase and (b) read out mode for focus spot recreation. In (a) the beam is split into two parts: reference and calibration paths. The calibration path creates a focus spot at the distal end of the MCF. This beam interferes with the reference beam at the CMOS after propagation through the fiber. In (b) the field recorded previously is phase conjugated and displayed on the SLM, which encodes the readout pulse before propagating through the MCF and recreating the focus spot. PBS= polarizing beam splitter, BS= beamsplitter, D= dichroic beamsplitter, 90/10= 90% reflection 10% transmission beamsplitter, Obj= objective lens, HWP= halfwave plate, L= lens, PMT= photomultiplier tube, SLM= spatial light modulator.

The temporal profile of the coherence-gated output was measured by first order cross correlation of the reference and the pulses transmitted through the MCF. To do this the delay line was moved in 20 μm steps (133 fs) and a hologram was recorded at each position. Then, by integrating the power in the first diffraction order of the hologram's Fourier transform, we measured the total power of the coherence-gated output from each core of the MCF at each step (Figure 5.2(a)). The temporal profile reveals that the light emerges from the MCF cores in two distinct LP modes: the LP_{01} and LP_{11} . Figure 5.2(b) and Figure 5.2(c) show the Fourier transforms of the hologram captured at $\tau_1 = 0.93$ ps and $\tau_2 = 7.2$ ps, respectively. A comparison of the spatial frequency components encoded in the holograms, shows distinct spatial frequency content in the two fields. After recovering the phase of the field, τ_1 is clearly the LP_{01} mode of each core (Figure 5.2(d)). This is apparent in the quadratic phase which encircles each core of the MCF at τ_1 . Whereas the phase recovered at τ_2 shows a phase image (Figure 5.2(e)) corresponding to the higher order LP_{11} mode. The inset of Figure 5.2(a) is a histogram showing the distribution of the times of the maximum power of the coherence function from each core during the LP_{01} mode arrival range. It contains 24 bins of 133 fs width.

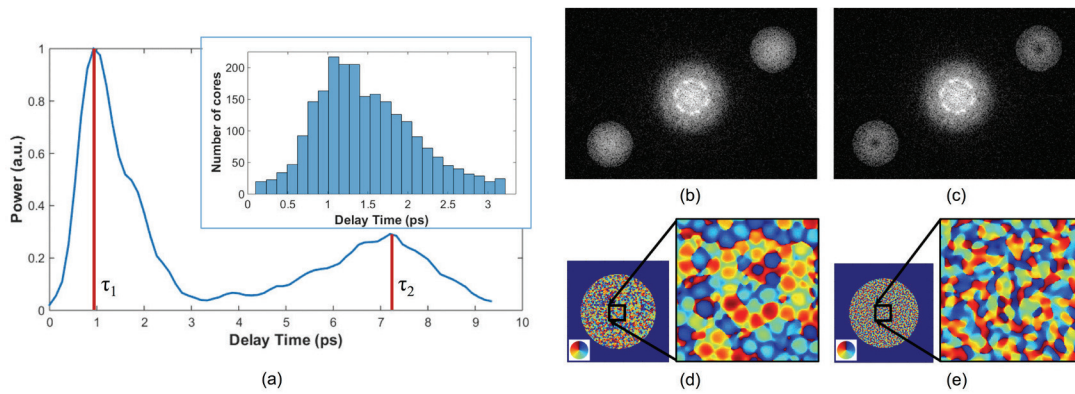


Figure 5.2: **The temporal profile of the total power of the coherence-gated output from the multicore fiber.** The inset shows a histogram of the times of the maximum power of the coherence function of the pulses from each core within the first 3.2 ps. (b) Fourier transform of the hologram captured at τ_1 . (c) Fourier transform of the hologram captured at τ_2 . (d) The phase reconstruction from (b) which shows quadratic phase patterns encircling individual cores indicating the LP_{01} mode. (e) The phase reconstruction from (c) with the LP_{11} mode in each core.

5.3 - Characterization of DPC focused ultrashort pulses

The reconstructed focus spots obtained by DPC of the LP_{01} and the LP_{11} modes were characterized. This analysis revealed that the focus spot created from the DPC in a MCF behaves in two distinct ways depending on the LP mode used in the reconstruction.

5.3.1 - Focal spot contrast and size

The calibration arm created a focus spot 225 μm away from the MCF distal end. After phase conjugation, the measured signal to the average of the background (SBR) for a calibration focus transversely centered on the fiber was 130 for phase conjugation with the LP_{01} and 60 for the LP_{11} modes of the MCF cores. The full width at half maximum of the focus was 1.5 μm for the LP_{01} mode and 1.3 μm for the LP_{11} mode. Because the fundamental mode consists of light which effectively has a lower NA than higher order modes, it is expected that the LP_{01} mode would create a larger focus spot than the LP_{11} mode [30]. We can use the measured spot sizes to calculate the effective NA (NA_{eff}) to be 0.27 and 0.31 for the LP_{01} and LP_{11} modes, respectively. Figure 5.3(a) shows the focal plane with the phase conjugated focus spot using the LP_{01} mode of the MCF cores at 225 μm from the MCF facet, in which the diffraction orders are not visible. After increasing the exposure time by 20 times (Figure 5.3(b)) the background becomes visible, including the spatially spread diffraction orders surrounding the phase conjugated focus at a lateral distance of 60 μm . The focus is 28 times more intense than the brightest spot in the diffraction order.

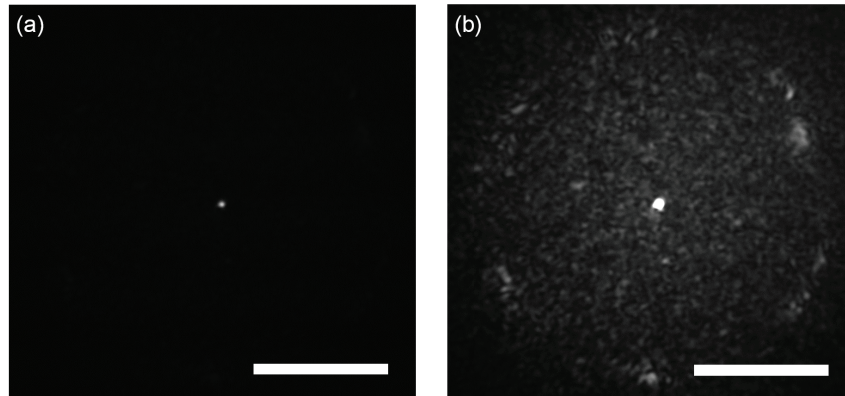


Figure 5.3: **Phase conjugated beam through multicore fiber.** (a) The focus spot created by phase conjugating the LP_{01} mode of the MCF cores at $225\ \mu\text{m}$ from the MCF facet. (b) The same focus spot with the exposure time increased $20\times$ to reveal the background, including the spread out diffraction orders. The scale bars are $50\ \mu\text{m}$.

5.3.2 - Modal contribution to focus spot

The temporal profile of the total power of the coherence-gated phase conjugated focus was analyzed at the distal end facet. An off-axis digital holography setup was built to enable this measurement. Figure 5.4 shows the temporal shape of the phase conjugated pulse at the distal end of the fiber, measured in the same way as Figure 5.2(a). When the LP_{01} mode was coherence-gated (at τ_1 in Figure 5.2(a)) and phase conjugated, we measured that 88% of the optical power exiting the fiber arrived in the LP_{01} mode (Figure 5.4(a)). In fact, 70% of the core pulses arrive within 0.5 ps at the distal end (Figure 5.4(a) inset). The spread is a result of varying group delay in each core [31]. In contrast, 70% of the pulses arrive within 1.25 ps at the proximal end during the hologram recording phase (Figure 5.2(a) inset). When coherence gating the LP_{11} mode, some of the optical power after DPC coupled into the LP_{01} mode, but most of the power (62%) propagated in the LP_{11} mode (Figure 5.4(b)). The loss of power could be attributed to slight misalignment or to phase-only wavefront modulation which contributed to the lower focal spot SBR when using the LP_{11} mode. These results demonstrate the ability of DPC to control and couple the pulse directly into the LP_{01} mode. As mentioned above, slight variations in core properties cause a spread in group delay between cores [31]. Inter-core group delay is not compensated by DPC, but coherence-gated DPC allows selective phase conjugation of pulses that have traveled with similar group delay. Thus, on the distal end they arrive within a similar time frame. Of course, large differences in group delay between cores results in some cores not contributing to the phase conjugation. We estimate that only approximately 50% of the cores contribute to the formation of the pulsed wavefront at the focus spot resulting in a loss of peak intensity by a factor of 4.

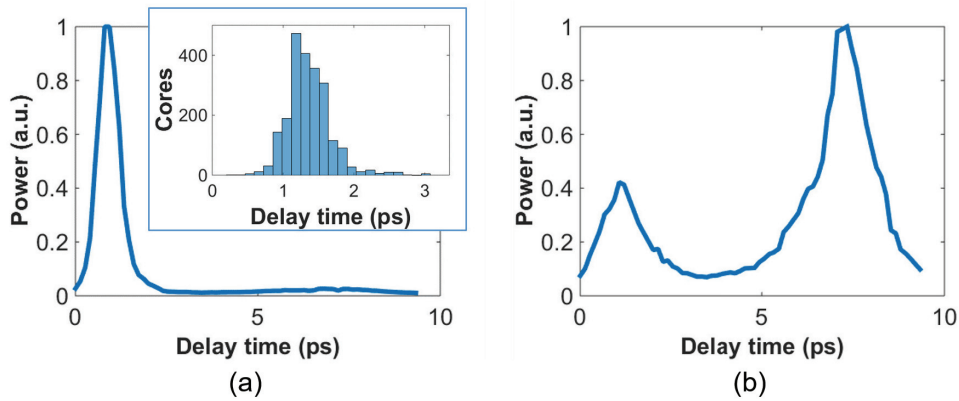


Figure 5.4: **Temporal profile of the phase conjugated beam through multicore fiber.** The temporal profile of the total power of the coherence-gated output from the distal end of the MCF after phase conjugation. (a) The pulse profile when phase conjugating the LP_{01} mode (at τ_1 in Figure 5.2(a)). The inset shows a histogram of the distribution of the time point of peak intensity of the coherence function of the pulses from each core within the first 3.2 ps. (b) The profile when phase conjugating the LP_{11} mode (at τ_2 in Figure 5.2(b)).

5.3.3 - Pulse length

To measure the pulse width of the focused pulse, the optical system was altered in order to build an interferometric second order autocorrelator. A Michelson interferometer with a variable delay in one arm was added into the reference path [32] to create two co-aligned pulses propagating with varying delay times. A two-photon screen (20 μm thick SU-8 with Rhodamine 6G) was placed in the focal plane of the fiber to provide a nonlinear signal for pulse autocorrelation. The measured pulse width of the optical focus using the phase conjugated LP_{01} mode (coherence-gate at the τ_1 peak in Figure 5.2(a)) was 390 fs. The pulse length was measured to be 270 fs before propagation through the fiber. The increased pulse length in this case is not due to the variability of the group delay from one core to another. Instead it is the result of chromatic dispersion in each core. In principle, pre-chirping the pulse could compensate this. We did not measure the pulse length of the optical focus phase conjugating the LP_{11} mode, because the intensity in the focus spot was not enough to generate two-photon signal.

5.4 - Digital scanning and field of view

TPF imaging through the MCF is enabled by scanning the focused femtosecond pulse across the object. This was implemented by recording and saving the phase conjugating hologram for each calibration focus spot in the sample plane. The distal end of the MCF was attached to a stage which moved transversely in 1 μm increments. In this way the focal spot position moved relative to the fiber facet. Once the holograms were saved in the computer memory, they were ready to be sequentially displayed on the SLM and scan a focus spot.

The field of view for imaging with this technique is limited by the angular spread of the phase conjugated mode. As the focus spot transversely moves away from the center of the fiber, fewer cores can contribute to the focus spot and the aperture at the fiber facet shrinks and loses its circular shape, as shown already in DPC operation at large distances from the fiber facet (see for example **Chapter 3** and [33]). Furthermore, the hologram records the phase value from each individual core, which essentially discretizes the phase by sampling the quadratic phase field of the diverging calibration beam. When the quadratic phase is too strong, the core spacing undersamples the field, causing aliasing effects and focusing into neighboring diffraction orders away from the desired focus.

The field of view was analyzed by simulating the spatial dependence of the focus intensity with the LP_{01} mode. To do this the phase conjugating field at the distal facet of the MCF is modeled and propagated with a beam propagation simulation. The resulting focus intensities reveal the usable and optimal range for imaging. The core positions were modeled according to the experimentally measured positions of the MCF. We simulated the propagation of a monochromatic beam ($\lambda = 785$ nm) from the MCF distal facet by a distance z to reconstruct the focus spot. We selected the phase of the field at each core by sampling the phase of a spherical wave centered at the focus position. A phased array pattern was then calculated using the radiation pattern of the LP_{01} mode centered at each core. Figure 5.5(a) shows an intensity map of the peak intensity of the focus radially (ρ) within a 100 μm -radius and axially (z) from the fiber facet to 500 μm . The simulation shows a peak intensity hot spot located between 300 μm and 400 μm from the facet. This is the point where all the cores significantly contribute to the focus reconstruction corresponding to the NA_{eff} of the phase conjugating mode. Also, creating a focus further from the facet minimizes the percentage of power in the diffraction orders. At $z = 225$ μm the simulation shows 15% of the total power in the focal spot, this value increases to 37% at $z = 500$ μm . It is important to note that we expect lower percentages with a pulsed laser due to group delay variability between cores and mode coupling. Beyond the peak intensity hot spot the focusing NA begins to decrease as the aperture diameter remains constant and z increases, thus the increasing focus spot size decreases the intensity. Figure 5.5(b) shows the experimentally obtained intensity distribution of the DPC generated focus spot at $z = 225$ μm . Figure 5.5(c) shows the profile of experimentally obtained focal spot intensities at $z = 225$ μm compared to the simulated intensity profile at that distance.

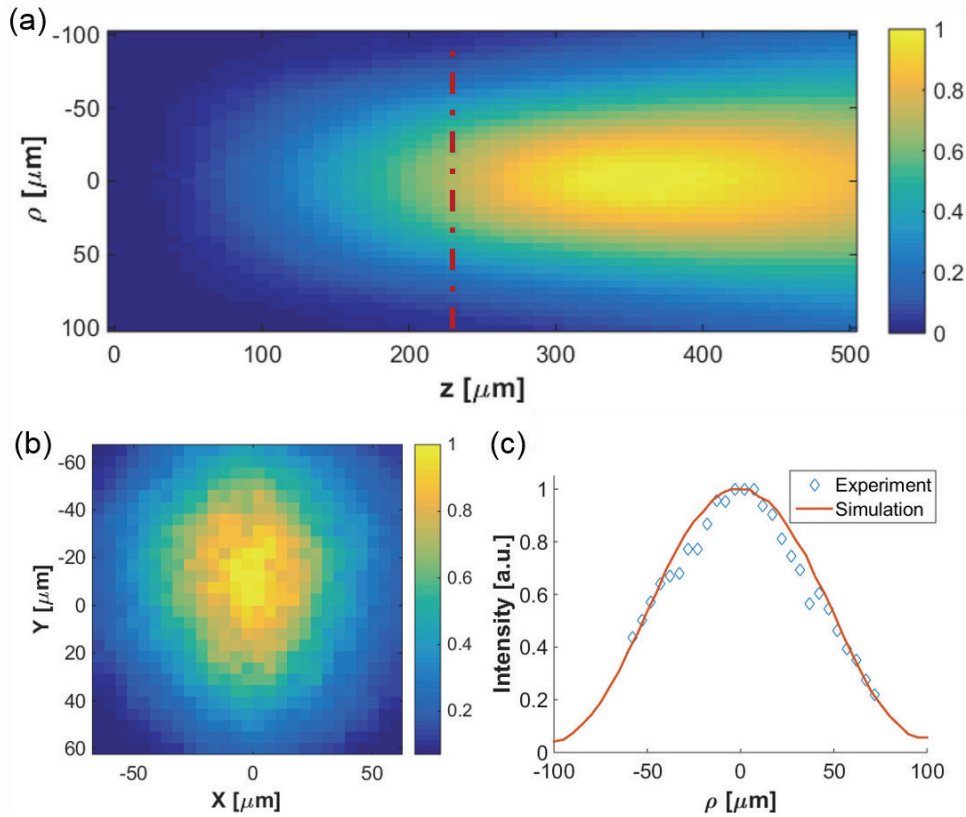


Figure 5.5: **Intensity of phase conjugated beam as function of position: simulation and experiment.** (a) The relative intensity of a phase conjugated focus spot at varying radial distance from fiber center (ρ) and distance from fiber facet (z). (b) The experimentally obtained intensity distribution of the DPC generated focus spot at $z = 225 \mu\text{m}$. (c) The simulated intensity profile of the red dashed line shown in (a) compared with experimentally acquired intensity data; both correspond to $z = 225 \mu\text{m}$.

5.5 - Two-photon imaging

In TPF microscopy the signal detected from a voxel of a fluorescent object is proportional to I^2 , where I is the peak intensity of the excitation beam. In the experimental setup, the overall average optical power from the laser is reduced by a factor of almost 30 by the time it reaches the distal end of the fiber (2.8 W to 100 mW). This is mostly due to the diffraction efficiency of the SLM. In addition only 1% of the transmitted power is concentrated on the 1.5 μm focused spot. This leads to an overall reduction by a factor of 3,000 in the available peak intensity from the raw laser beam to the focused femtosecond pulse we obtain at the distal end of the fiber. Nevertheless, we obtain a peak intensity of approximately $1.6 \times 10^9 \text{ W/cm}^2$ with a 390 fs pulse. We used these pulses to demonstrate TPF imaging and optical sectioning through the MCF by imaging a three-dimensional sample of 1 μm polystyrene beads stained with Rhodamine 6G mounted in PDMS. An $80 \times 80 \mu\text{m}^2$ focal plane was calibrated with 1 μm steps between focus spots. An imaging plane at $z = 225 \mu\text{m}$ was

selected for optimal fluorescence collection. We measured the collection efficiency of the MCF for the fluorescence signal to be 20% collection and transmission of light within the fiber NA. With the LP₀₁ phase conjugating holograms saved, the sample was placed in the focal plane and the saved holograms were sequentially projected to scan the focal spot. The holograms were projected by the SLM at a 7 Hz rate. The central focus spot had 1 mW average power. For detection, the excited TPF signal collected by the MCF is deflected by a dichroic mirror (700 nm longpass) to a photomultiplier tube detector (Hamamatsu, H11526-20-NN) (Figure 5.1(b)). For simplicity in this initial demonstration, the axial scan was performed in four planes by moving the fiber in $\Delta z = 10 \mu\text{m}$ steps. The obtained image (Figure 5.6) shows slices of the high resolution, high contrast TPF image. The Y-Z and X-Z slices of the image demonstrate axial sectioning, with a depth of field determined by the NA_{eff} of the LP₀₁ mode, in this case $\sim 16 \mu\text{m}$ [4]. The Y-Z and X-Z slices in Figure 5.6 were obtained by interpolation of the 4 data points using the software ImageJ.

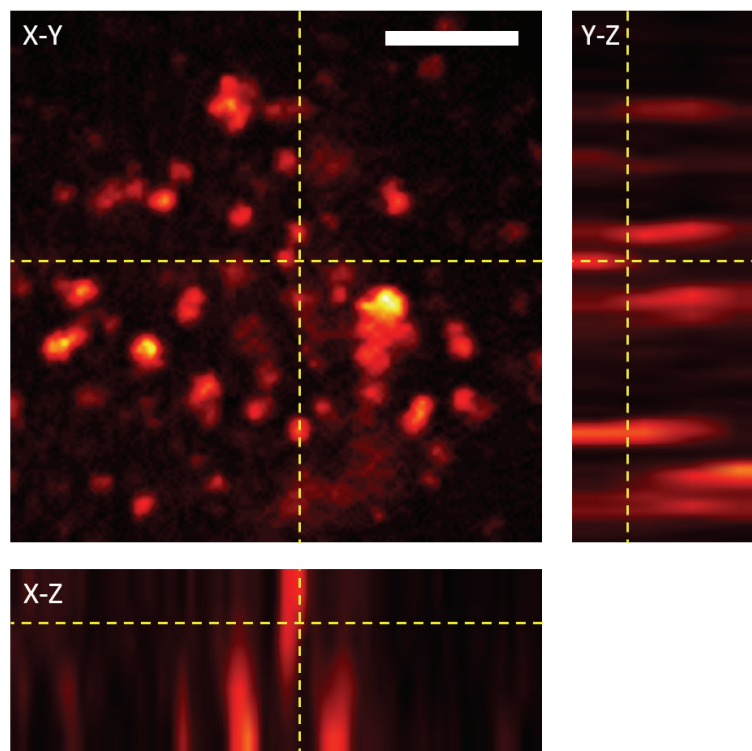


Figure 5.6: **Two-photon fluorescent image of 1 μm polystyrene beads stained with Rhodamine 6G dispersed in PDMS.** The image was acquired using DPC with the MCF to sequentially create 80×80 focus spots spaced by $1 \mu\text{m}$. These were scanned at 4 axial planes separated by $10 \mu\text{m}$. The fluorescence detection was performed at the proximal side of the MCF. Power in focus: 1 mW at image center. Pixel dwell time: 140 ms. The scale bar is $20 \mu\text{m}$.

To further demonstrate TPF imaging through the MCF, we imaged clustered cells. We prepared human colon carcinoma (HCT 116) cells by staining them with Rhodamine 6G and mounting them on a microscope slide under a cover slide. The cell clusters provided a good object to test the resolvability of individual cells with the resolution provided by the MCF. Figure 5.7(a) and Figure 5.7(b) show a highly dense clustering of HCT 116 cells. In the TPF image individual cells are clearly distinguishable. Figure 5.7(c) and Figure 5.7(d) show a less dense clustering of cells in which the TPF image shows individual cells and good agreement with the white light, widefield image.

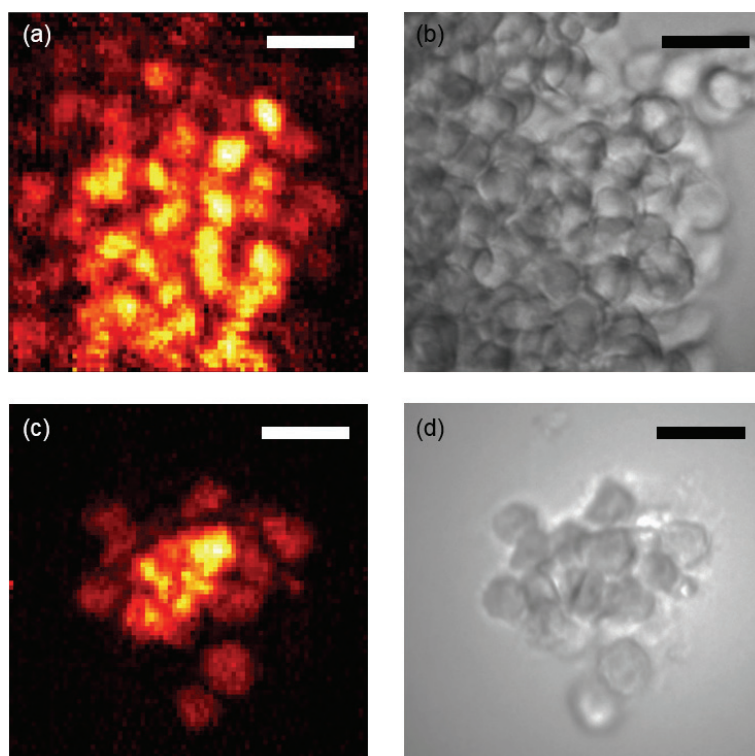


Figure 5.7: **Two-photon images of stained cells through multicore fiber.** (a) and (c) Two-photon fluorescent image of HCT 116 cells stained with Rhodamine 6G. The images were acquired using DPC with the MCF to sequentially create 80×80 focus spots spaced by $1 \mu\text{m}$. The fluorescence detection was performed at the proximal side of the MCF. Power in focus: 1 mW at image center. Pixel dwell time: 140 ms . (b) and (d) The corresponding white light, widefield images of the cells. Scale bars are $20 \mu\text{m}$.

5.6 - Conclusions

We have presented wavefront shaping for focusing ultrashort pulses through commercially available MCFs. In this chapter, we utilized DPC of ultrafast pulses for the wavefront calibration and focusing. DPC allows for a single-shot calibration for focusing to a single point at the distal end of the fiber. DPC focusing with the MCF yielded SBR of ~ 130 which

was sufficient for TPF imaging through the MCF. It should be noted that the image was formed despite the sub-optimal collection efficiency of the MCF, a result of the cores covering only $\sim 33\%$ of the fiber facet. To overcome this problem, Andresen, et al. designed a double clad fiber to increase the collection efficiency of their MCF endoscope [19]. Of course, implementing a similar approach for increased light collection efficiency would require a custom designed fiber. Furthermore, in this implementation we did not include any chromatic dispersion compensation, because of the relatively short length of the fiber. Although, we could expect further improvement in the excited TPF signal by pre-chirping the pulse.

The commercially available MCFs allowed for an imaging field of view and resolution currently not possible with highly spaced core MCFs. The small core diameters propagate only a few modes, thus limiting modal dispersion. Additionally, we have shown that the commercially available MCFs provide benefits due to their quasi-periodic and high-density core arrangement. Specifically, these offer an increased field of view due to the suppression and spreading of the diffraction orders. To understand what limits the field of view, we simulated focusing at different axial and radial distances and found that the optimal focusing distance is determined by the distance at which the mode NA_{eff} and MCF diameters allow for focal spot contribution from all cores. This is in contrast to MMFs and confocal use of MCFs, which operate optimally near the distal end facet. We also explored the unique characteristics of coherence-gated DPC with the fundamental LP_{01} mode and the higher order LP_{11} mode. We found that when phase conjugating the LP_{01} mode of the MCF that most of the energy stayed in the LP_{01} after propagating through the fiber. The MCF length that we used had a minimal spread in inter-core group delay. Further lengthening the fiber would increase the delay between cores and reduce the number of cores participating in the phase conjugation. On the other hand, a shorter fiber would increase the number of cores contributing and would increase the focal spot power.

In conclusion, we have demonstrated lensless focusing of ultrashort pulses through a commercially available MCF for TPF imaging. We demonstrated optical sectioning with TPF imaging on a 3D matrix of dispersed fluorescent beads and we also showed cellular imaging through the MCF. These results indicate the potential of high-density MCFs for integration into high-resolution TPF endoscope imaging.

Bibliography

- [1] D. Kim *et al.*, “Toward a miniature endomicroscope: pixelation-free and diffraction-limited imaging through a fiber bundle,” *Opt. Lett.*, vol. 39, no. 7, pp. 1921–1924, Apr. 2014.
- [2] D. B. Conkey, N. Stasio, E. E. Morales-Delgado, M. Romito, C. Moser, and D. Psaltis, “Lensless two-photon imaging through a multicore fiber with coherence-gated digital phase conjugation,” *J. Biomed. Opt.*, vol. 21, no. 4, p. 045002, Apr. 2016.
- [3] W. Denk, J. H. Strickler, and W. W. Webb, “Two-photon laser scanning fluorescence microscopy,” *Science*, vol. 248, no. 4951, pp. 73–76, Apr. 1990.
- [4] W. R. Zipfel, R. M. Williams, and W. W. Webb, “Nonlinear magic: multiphoton microscopy in the biosciences,” *Nat. Biotechnol.*, vol. 21, no. 11, pp. 1369–1377, Nov. 2003.
- [5] F. Helmchen and W. Denk, “Deep tissue two-photon microscopy,” *Nat. Methods*, vol. 2, no. 12, pp. 932–940, Dec. 2005.
- [6] I. Pavlova, K. R. Hume, S. A. Yazinski, R. M. Peters, R. S. Weiss, and W. W. Webb, “Multiphoton microscopy as a diagnostic imaging modality for lung cancer,” 2010, vol. 7569, pp. 756918–756918–7.
- [7] S. W. Perry, R. M. Burke, and E. B. Brown, “Two-Photon and Second Harmonic Microscopy in Clinical and Translational Cancer Research,” *Ann. Biomed. Eng.*, vol. 40, no. 2, pp. 277–291, Feb. 2012.
- [8] E. E. Hoover and J. A. Squier, “Advances in multiphoton microscopy technology,” *Nat. Photonics*, vol. 7, no. 2, pp. 93–101, Feb. 2013.
- [9] J. N. D. Kerr and W. Denk, “Imaging in vivo: watching the brain in action,” *Nat. Rev. Neurosci.*, vol. 9, no. 3, pp. 195–205, Mar. 2008.
- [10] W. Göbel, J. N. D. Kerr, A. Nimmerjahn, and F. Helmchen, “Miniaturized two-photon microscope based on a flexible coherent fiber bundle and a gradient-index lens objective,” *Opt. Lett.*, vol. 29, no. 21, pp. 2521–2523, Nov. 2004.
- [11] M. T. Myaing, D. J. MacDonald, and X. Li, “Fiber-optic scanning two-photon fluorescence endoscope,” *Opt. Lett.*, vol. 31, no. 8, p. 1076, 2006.
- [12] D. R. Rivera *et al.*, “Compact and flexible raster scanning multiphoton endoscope capable of imaging unstained tissue,” *Proc. Natl. Acad. Sci.*, vol. 108, no. 43, pp. 17598–17603, Oct. 2011.
- [13] O. Ferhanoglu, M. Yildirim, K. Subramanian, and A. Ben-Yakar, “A 5-mm piezo-scanning fiber device for high speed ultrafast laser microsurgery,” *Biomed. Opt. Express*, vol. 5, no. 7, pp. 2023–2036, Jul. 2014.
- [14] B. A. Flusberg, E. D. Cocker, W. Piyawattanametha, J. C. Jung, E. L. M. Cheung, and M. J. Schnitzer, “Fiber-optic fluorescence imaging,” *Nat. Methods*, vol. 2, no. 12, pp. 941–950, Dec. 2005.
- [15] H. H. Hopkins and N. S. Kapany, “A Flexible Fibrescope, using Static Scanning,” *Nature*, vol. 173, no. 4392, pp. 39–41, Jan. 1954.
- [16] K. L. Reichenbach and C. Xu, “Numerical analysis of light propagation in image fibers or coherent fiber bundles,” *Opt. Express*, vol. 15, no. 5, p. 2151, 2007.
- [17] X. Chen, K. L. Reichenbach, and C. Xu, “Experimental and theoretical analysis of core-to-core coupling on fiber bundle imaging,” *Opt. Express*, vol. 16, no. 26, p. 21598, Dec. 2008.

- [18] A. J. Thompson, C. Paterson, M. A. A. Neil, C. Dunsby, and P. M. W. French, “Adaptive phase compensation for ultracompact laser scanning endomicroscopy,” *Opt. Lett.*, vol. 36, no. 9, pp. 1707–1709, May 2011.
- [19] E. R. Andresen, G. Bouwmans, S. Monneret, and H. Rigneault, “Toward endoscopes with no distal optics: video-rate scanning microscopy through a fiber bundle,” *Opt. Lett.*, vol. 38, no. 5, p. 609, Mar. 2013.
- [20] E. R. Andresen, G. Bouwmans, S. Monneret, and H. Rigneault, “Two-photon lensless endoscope,” *Opt. Express*, vol. 21, no. 18, p. 20713, Sep. 2013.
- [21] I. N. Papadopoulos, S. Farahi, C. Moser, and D. Psaltis, “Focusing and scanning light through a multimode optical fiber using digital phase conjugation,” *Opt. Express*, vol. 20, no. 10, p. 10583, May 2012.
- [22] T. Čížmár and K. Dholakia, “Exploiting multimode waveguides for pure fibre-based imaging,” *Nat. Commun.*, vol. 3, p. 1027, Aug. 2012.
- [23] S. Bianchi and R. D. Leonardo, “A multi-mode fiber probe for holographic micromanipulation and microscopy,” *Lab. Chip*, vol. 12, no. 3, pp. 635–639, Jan. 2012.
- [24] Y. Choi *et al.*, “Scanner-Free and Wide-Field Endoscopic Imaging by Using a Single Multimode Optical Fiber,” *Phys. Rev. Lett.*, vol. 109, no. 20, p. 203901, Nov. 2012.
- [25] E. E. Morales-Delgado, S. Farahi, I. N. Papadopoulos, D. Psaltis, and C. Moser, “Delivery of focused short pulses through a multimode fiber,” *Opt. Express*, vol. 23, no. 7, p. 9109, Apr. 2015.
- [26] E. E. Morales-Delgado, D. Psaltis, and C. Moser, “Two-photon imaging through a multimode fiber,” *Opt. Express*, vol. 23, no. 25, pp. 32158–32170, Dec. 2015.
- [27] Y. Kim *et al.*, “Adaptive Multiphoton Endomicroscope Incorporating a Polarization-Maintaining Multicore Optical Fibre,” *IEEE J. Sel. Top. Quantum Electron.*, vol. 22, no. 3, pp. 1–8, May 2016.
- [28] N. Stasio, D. B. Conkey, C. Moser, and D. Psaltis, “Light control in a multicore fiber using the memory effect,” *Opt. Express*, vol. 23, no. 23, pp. 30532–30544, Nov. 2015.
- [29] G. P. J. Laporte, N. Stasio, C. Moser, and D. Psaltis, “Enhanced resolution in a multimode fiber imaging system,” *Opt. Express*, vol. 23, no. 21, pp. 27484–27493, Oct. 2015.
- [30] K. Okamoto, *Fundamentals of Optical Waveguides*. Academic Press, 2010.
- [31] E. R. Andresen, S. Sivankutty, G. Bouwmans, L. Gallais, S. Monneret, and H. Rigneault, “Measurement and compensation of residual group delay in a multi-core fiber for lensless endoscopy,” *JOSA B*, vol. 32, no. 6, pp. 1221–1228, Jun. 2015.
- [32] O. Katz, E. Small, Y. Bromberg, and Y. Silberberg, “Focusing and compression of ultrashort pulses through scattering media,” *Nat. Photonics*, vol. 5, no. 6, pp. 372–377, Jun. 2011.
- [33] N. Stasio *et al.*, “Towards new applications using capillary waveguides,” *Biomed. Opt. Express*, vol. 6, no. 12, pp. 4619–4631, Dec. 2015.

Chapter 6

Light control in a multicore fiber using the memory effect

As explained in the previous chapter, endoscopic imaging through a multicore fiber (MCF) is widely used but is affected by pixelated images, which limits its resolution to a few micrometers. This is due to the spacing between the cores of the MCF, which has to be kept large enough to avoid core-to-core light coupling. In **Chapter 5** we showed that wavefront shaping techniques, such as digital phase conjugation, are able to focus light to a resolution finer than the inter-core spacing. However, when a point scanning image has to be taken, a long calibration procedure is needed. In fact, to form a $N \times N$ pixels image, $N \times N$ calibration focus spots must be sent through the MCF to create the needed phase lookup table. Moreover, the calibration depends on the optical fiber conformation, so a single-shot calibration is highly desirable. This would allow, in fact, recalibration procedures that do not require access to both sides of the fiber. Here, we show that images can be formed even when the calibration step comprises only the acquisition of a single digital hologram. Again, we use again digital phase conjugation to focus light as shown in the previous chapter, but here we scan the focus spot exploiting the memory effect, present in MCFs. In addition, we show how simple and complex patterns can be projected using the same MCF.

Part of the material presented in this chapter has been published in ([1], [2]):

- **N. Stasio**, D. B. Conkey, C. Moser, and D. Psaltis, “Light control in a multicore fiber using the memory effect,” *Opt. Express*, vol. 23, no. 23, pp. 30532–30544, Nov. 2015.
- **N. Stasio**, D. Conkey, C. Moser, and D. Psaltis, “The Memory Effect in Multicore Fibers,” in *Imaging and Applied Optics 2016 (2016)*, paper ITh1F.1, 2016, p. ITh1F.1.

6.1 - Introduction

Limitations such as low resolution and invasiveness in endoscopic imaging have driven research towards high-resolution endoscopy by using ultrathin optical fibers. This has been possible by exploiting wavefront shaping techniques: optimization algorithms [3], [4], digital phase conjugation (DPC) [5], [6], and transmission matrix approaches [7], [8] have allowed imaging with diffraction limited resolution in ultrathin, high numerical aperture fibers.

As we have discussed already, wavefront shaping techniques require a calibration step for characterizing the optical fiber. In order to scan a diffraction limited focus spot in a regular grid across the whole facet of an optical fiber, the calibration step requires a large number of acquisitions. Theoretically, the number of acquisitions should be at least equivalent to the number of modes supported by the fiber in the case of transmission matrix approaches.

The scanning ability of the wavefront shaped focus spot through a step index MMF is limited to radial scanning, which prohibits the use of conventional scanning techniques [9] and limits the scanning speed to the refresh rate of a wavefront modulation device.

As shown in the previous chapter, the same wavefront shaping approaches used with MMFs have been applied to MCFs to create pixelation-free, diffraction-limited images, adding a new imaging modality to classical MCF based endoscopes. A transmission matrix approach was used with MCFs to account for mode coupling, as well as for core-to-core crosstalk [10]. Additional work has integrated wavefront shaping for optical focus creation and scanning with a MCF. This effort included the development of a custom-made, single-mode core MCF with 169 cores with spacing large enough to eliminate core-to-core crosstalk and enable focus spot scanning [11], [12]. A higher number of cores, which could support many modes, increases the wavefront shaping degrees of freedom, which would contribute to increase the amount of light delivered in the focus and reduce the background.

In this chapter, we investigate the characteristics of spot focusing and scanning by DPC through commercially available MCFs with a high number of densely packed multimode cores, with the acquisition of a single calibration hologram. We observed that, as in thin scattering media [13], [14], phase gradients are conserved within a certain range when coherent light is propagated through MCFs, resulting in a translational “memory effect.” Thus, despite mode coupling and core crosstalk, a focus spot can be steered through a significant scan range thanks to the memory effect present in this kind of optical fiber. This feature enables the use of a single real time feedback mechanism to create a scannable focus spot, which could potentially be steered with high-speed galvo-mirrors.

The ideal wavefront shaping technique for a single step calibration is DPC, in which only one digital hologram is necessary to create an optical focus. This simplifies the calibration step compared to [11], [12], in which a core by core calibration step was required for characterization. DPC has been extensively used for MMF endoscopy, but it also applies to MCF as shown in a pioneering work by Bellanger, et al. [15]. Single step calibration has been shown in MCF in [16], reaching a focus spot with a peak to background ratio of approximately 50. We show here that a ratio of above 1000 can be reached by DPC, since this technique gives the optimal phase pattern in order to obtain a focused spot.

6.2 - Experimental setup

We implemented DPC through MCF using the experimental setup schematically illustrated in Figure 6.1. The laser beam from a He-Ne laser ($\lambda = 632.8$ nm) is expanded and collimated by the 4f system formed by lenses OBJ1 and L1. A polarizing beam splitter (PBS) splits the beam into two arms: the calibration arm and the reference arm. The calibration arm is directed towards the objective (OBJ2) and is focused at plane S in front of the surface of the distal end of the MCF. The output of the fiber bundle is imaged by the imaging system OBJ3-L3 onto a CMOS camera (MV1-D1312IE-100-G2-12, Photonfocus), where it interferes with the reference arm, generating a digital hologram. A polarizer is placed before the CMOS and is oriented horizontally. The phase of the recorded complex field is digitally calculated, conjugated, and assigned to a spatial light modulator (SLM, Pluto-VIS, Holoeye). For optical phase conjugation, the reference beam is shaped by the SLM and sent into the MCF. After propagation, the phase conjugated beam recreates a focused spot in the plane S at the calibration location.

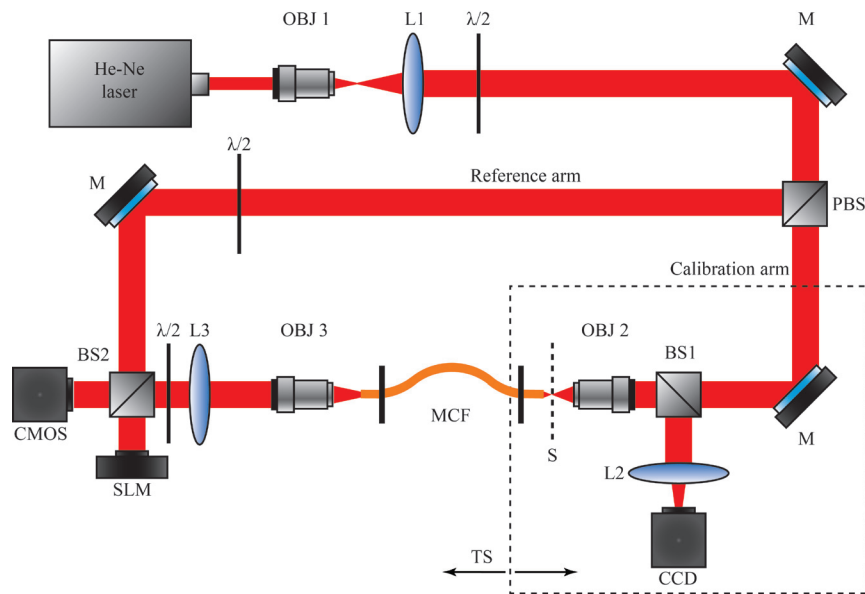


Figure 6.1: **Experimental optical setup.** The output of a He-Ne laser is expanded and is split by the polarizing beam splitter PBS into the calibration and reference arms. The objective OBJ2 focuses the calibration beam in a plane S in front of the distal end of the multicore fiber (MCF). The proximal end facet of the MCF is imaged on the CMOS sensor through the 4f imaging system OBJ3-L3. Using the non-polarizing beam splitter BS2, the reference arm is combined with the image on the CMOS to form a digital hologram. The phase extracted from the digital hologram is conjugated and projected on the spatial light modulator (SLM), which modulates and reflects the reference beam towards the MCF through BS2. A focus spot forms in the plane S and is imaged using the 4f system OBJ2-L2 on the CCD camera. The translational stage TS bends the fiber in a controllable way. OBJ1= 10 \times , NA= 0.25, Newport, OBJ2= OBJ3= 20 \times , NA= 0.4, Newport. Focal length lenses: L1= 150 mm, L2= 100 mm, L3= 200 mm.

On the distal end of the MCF the objective (OBJ2), the non-polarizing beam splitter (BS1), the lens (L2), and a CCD camera are all mounted on a translational stage (TS) to control the bending of the MCF and simultaneously check the quality of the phase conjugated spot. For our experiments we use a 3000 core MCF (FIGH-30-215S, Fujikura), the fiber diameter is 190 μm , the core diameters are measured to be on average 2.5 μm (they are actually slightly different to minimize core-to-core coupling [17], [18]), and the core and cladding refractive indexes are $n_1= 1.497$ and $n_0= 1.457$, yielding a numerical aperture (NA) of 0.34. Each core can support about 4 linearly polarized (LP) modes.

6.3 - Digital phase conjugation focus characterization

To understand the DPC focusing characteristics of the MCF, we analyzed the recreated focus spots dependence on distance between the plane S and the fiber facet, which we define as working distance. First, we measured the full width at half maximum (FWHM) of the phase conjugated spot, with each focus created within plane S aligned to the center of the MCF. This is shown by the blue curve in Figure 6.2(a). For working distances less than 250 μm , the spot size remains constant, but beyond this distance, the FWHM increases linearly. Within 250 μm , the focused spot size is determined by the fiber NA. Phase conjugation at larger working distances increases the spot size [6]. In this case, fiber diameter and working distance determine the FWHM. With the same data we also evaluated the enhancement of the focused spot, defined as the ratio between the peak intensity of the focus and the mean intensity of a speckle field generated by a random phase pattern. This quantity depends linearly on the number of degrees of freedom used to form the focused spot [19]. In this case the theoretical maximum enhancement would be approximately the number of fiber cores multiplied by the number of modes per core, if all the modes would be controlled at the same time. If all the modes and/or the cores are not fully excited during the calibration step, the maximum enhancement will be lower than the theoretical one. The enhancement versus the working distance is shown by the red curve in Figure 6.2(a). The peak enhancement is reached when all the cores of the MCF are contributing to the focusing, which occurs where the outer cores are excited with an angle equal to $\arcsin(NA)$. Beyond this distance the enhancement decreases with the peak intensity (decreases as the FWHM of the focus spot increases) and the number of excited higher order modes (the incidence angle on the outer cores lower than $\arcsin(NA)$).

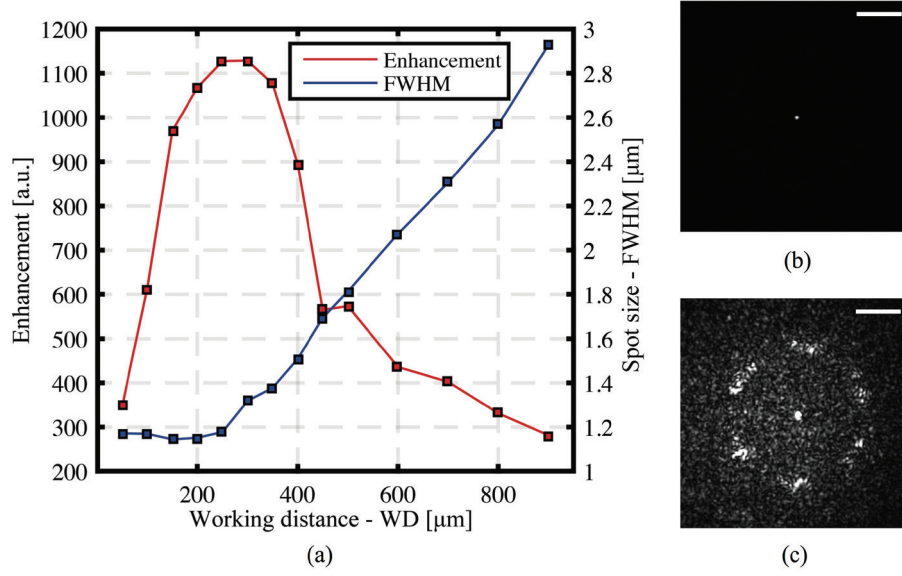


Figure 6.2: **Digital phase conjugated focus spot characterization.** (a) Focus spot size (FWHM, blue points) and enhancement (red points) as a function of the working distance. The lines are drawn only for clarity. (b) Example of DPC focus spot imaged on the CCD camera. (c) The same focus spot of (b) with the CCD exposure time increased 100 times. The six bright speckle areas around the main lobe are a result of the quasi-periodicity of the MCF. Scale bars are 20 μm .

6.4 - Using the memory effect in a multicore fiber

6.4.1 - Transverse scanning with the MCF

With the DPC-generated focus spot, a shift of the focus spot is possible by changing the tilt of the phase conjugated wave incident on the MCF. The memory effect of the MCF allows a transverse shift of the phase-conjugated spot by assigning to the SLM a phase pattern equal to:

$$\phi_{SLM}(x,y) = \arg \left[e^{j\phi_{DPC}(x,y)} e^{j(K_x x + K_y y)} \right], \quad (6.1)$$

where $\phi_{DPC}(x,y)$ is the optimal phase to recreate a focus spot in a given plane S and the second exponential term represents a plane wave having a carrier frequency, $\vec{K} = (K_x, K_y)$. This allows for scanning a focus spot in the plane S with a single digital hologram calibration. Figure 6.3(a) shows a collection of focus spots scanned in a plane 400 μm from the MCF facet. The spots shown in the figure were created individually with a fixed step size, ΔK , and combined into a single image for clarity. The cross-sectional plot in Figure 6.3(b) shows the decay in the focus spot peak intensity with increasing $|K_x|$. For a constant wave carrier frequency \vec{K} , the physical focal spot shift increases linearly with the working distance. The intensity drop can be explained as follows: during phase conjugation, the light

sent into the MCF couples into the distinct modes of each core. The mode confinement is the highest for the fundamental mode and decreases as the order of the mode increases [20]. This results in high order modes coupling more easily into neighboring cores. In fact, steering the beam changes the phase relationship between cores, which affects the core-to-core coupling and decreases the phase conjugation efficiency. This aspect is more pronounced when the coupling between cores is more significant, as in the higher order modes case. In other words, core-to-core coupling limits the final scanning range.

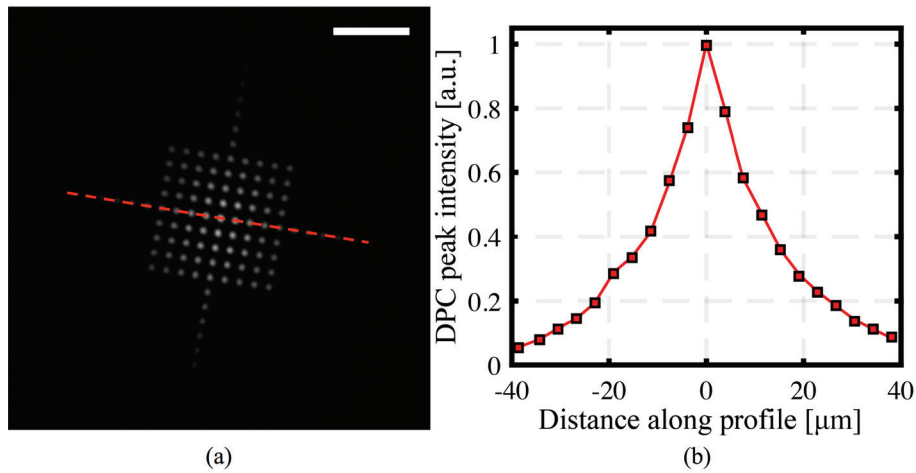


Figure 6.3: **Digital scanning of the focus spot using a single calibration hologram.** (a) The phase conjugation pattern is combined with a linear phase gradient and projected on the SLM. By changing the direction and the strength of the gradient it is possible to scan the focus spot in a regular grid. The image is a combination of several DPC projections. (b) The square markers represent the peak intensities of the DPC spots along the red dashed line in (a). Scale bar 20 μm.

A proof of this concept is shown using an ultrafast pulsed laser. We replaced the He-Ne laser shown in the setup in Figure 6.1 with a 140 fs duration pulsed laser (Chameleon, Coherent, wavelength 785 nm). Because of the ultrashort pulse and modal dispersion in the cores, the few modes of the fiber come out of the MCF separated in time. As shown in the previous chapter, by time gating the acquisition of the digital hologram with the pulsed reference beam, it is possible to select the optical mode to phase conjugate. With this system we were able to analyze the scanning ability of different waveguide modes with a single hologram. The blue and the red curves in Figure 6.4 show the scanning range obtained using the fundamental LP_{01} mode (red) and the LP_{11} mode (blue) respectively. The spot was scanned at a distance of 225 μm from the MCF facet. The LP_{01} mode has a wider, more slowly decaying scanning range compared to the LP_{11} mode. CW focus spot scanning consists of the interference between the LP_{01} , LP_{11} and possibly even higher order modes depending on the cores and the laser wavelength. Here we see that the decay profile shown in Figure 6.3(b) is the result of the LP_{01} mode and the less resilient higher order modes.

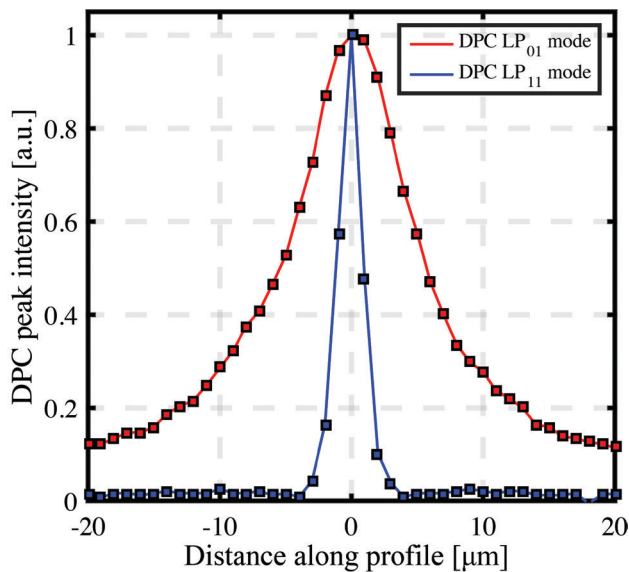


Figure 6.4: **Memory effect in multicore fibers: mode dependence.** Using a pulsed laser it is possible to independently phase conjugate distinct modes of the MCF cores. The scanning range of the fundamental LP_{01} mode is larger than the one of the higher order modes because of the limited core-to-core coupling.

A proof of concept experiment was implemented to show the ability to perform imaging using a single hologram and the memory effect (Figure 6.5). After the recording of the single calibration hologram, a USAF resolution chart was placed $300\ \mu\text{m}$ from the fiber distal facet. The laser beam was focused using DPC and scanned tilting the wavefront on the SLM. The transmitted signal through the resolution chart was collected using the CCD camera on the sample side. The laser used was continuous wave centered at $785\ \text{nm}$. Figure 6.5(a) shows a widefield image of a USAF resolution chart centered on the Group 7 element 5. Figure 6.5(b) is obtained by integrating all the photons reaching the CCD while performing DPC. Figure 6.5(c) is obtained, instead, by acquiring the maximum of the signal on the CCD, which is equivalent to implementing a confocal microscope with a pinhole as large as the camera pixel size (see [16]). Both Figure 6.5(b) and Figure 6.5(c) show one to one correspondence with the widefield image.

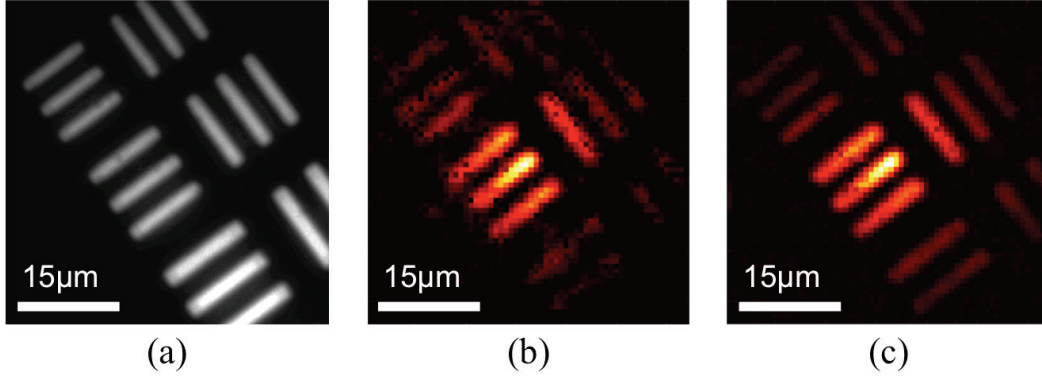


Figure 6.5: **Imaging using digital phase conjugation in combination with memory effect.** (a) white light optical image of a USAF resolution chart; (b) image obtained integrating the total transmitted light through the sample on the distal side CCD; (c) image obtained calculating the peak intensity of the recorded signal on the CCD.

6.4.2 - Axial scanning with MCF

In addition to transverse scanning, by adding a positive or negative parabolic phase pattern to the reference wavefront, $\phi_{DPC}(x, y)$, the phase-conjugated spot can also be shifted in the axial direction to enable 3D digital scanning. Figure 6.6 shows the axial variation of the focusing PSF. By adding a positive quadratic phase (a positive lens) to $\phi_{DPC}(x, y)$ the focus spot is shifted toward the fiber, and the opposite is true for a negative lens. Defining F as refocusing parameter, $\phi_{SLM}(x, y)$ can be rewritten as:

$$\phi_{SLM}(x, y) = \arg \left[e^{j\phi_{DPC}(x, y)} e^{-j\frac{\pi}{\lambda F}(x^2 + y^2)} \right], \quad (6.2)$$

where λ is the laser wavelength (632.8 nm in this case). We measured the FWHM of the attainable axial shift to be 60 μm (Figure 6.6), where the axial position of the DPC calibration is at the center of the scanning range (400 μm from the MCF facet in this case).

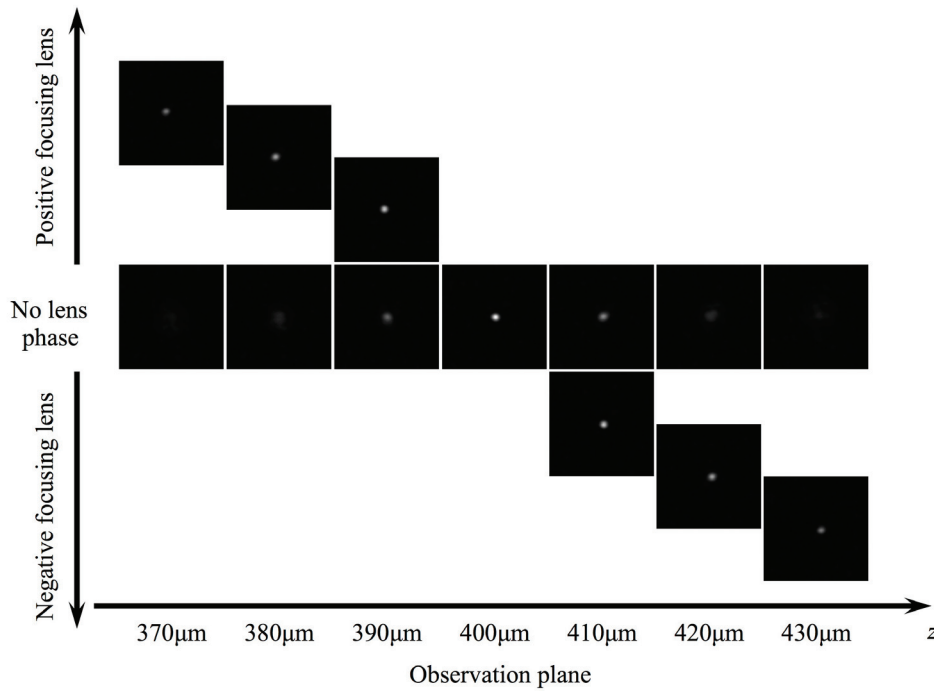


Figure 6.6: **Axial shifting of the digital phase conjugated focus spot using a single calibration hologram.** The central row of images shows a phase-conjugated spot observed at different planes. The calibration hologram was taken focusing at a distance of $400\ \mu\text{m}$ from the fiber facet. By adding a negative lens phase to the phase hologram, the focus shifts towards the fiber. The images above and below the central row show the axial shift of the focus with the increasingly positive or negative lens phases.

6.4.3 - No coupling scan range

In this section we show that the maximum attainable scanning range depends on the individual cores of the MCF, and in particular on their NA . Without loss of generality, let us consider an array of identical single-mode cores, where $E_a(x)$ is the mode of each core. The waveguide array is mathematically expressed as:

$$A(x) = \text{comb}(\Lambda_x x) * E_a(x), \quad (6.3)$$

where Λ_x is the center-to-center distance between the center of two neighboring cores and $*$ is the convolution operator.

If a quadratic phase is added to the input of waveguide array to focus at a focal length, f , the optical field in the focusing plane is equivalent to the Fourier transform (FT) of the input field with scaling dependent on f and the wavelength, λ :

$$\tilde{A}(f_x) = FT\{A(x)\} = FT\{\text{comb}(\Lambda_x x)\} \cdot FT\{E_a(x)\}. \quad (6.4)$$

Thus, in the absence of core-to-core coupling the scanning range is limited by the maximum spatial extent of the envelope $FT\{E_a(x)\}$, which is ultimately determined by the NA of the cores. If $E_a(x)$ is approximated with a Gaussian beam of waist size $w(0)$, then we can find an expression for the maximum scanning range, w_{MAX} , defined as the waist of the Gaussian beam diffracted after propagating the working distance, f . Defining $z_R = \pi w_0^2/\lambda$ as the Rayleigh length, and knowing that $z_R = w_0/NA$, we can write:

$$w^2(z) = \left[w(0) \sqrt{1 + \left(\frac{z}{z_R} \right)^2} \right]^2 = w^2(0) \left(1 + \frac{z^2}{z_R^2} \right) = w^2(0) + z^2 NA^2, \quad (6.5)$$

thus:

$$w_{MAX} = w(f) = \sqrt{w^2(0) + f^2 NA^2}. \quad (6.6)$$

In intensity this scanning range is decreased by a factor $\sqrt{2}$.

For imaging purposes, the field of view (FOV) and the maximum scanning range are not necessarily the same. In fact, due to the periodicity of the cores the focusing plane contains several focus spots, not just a single focused spot. The spacing between the foci p_x is given by:

$$p_x = f \tan(\arcsin(NA)) = f \tan\left(\arcsin\left(\frac{\lambda}{\Lambda_x}\right)\right) \approx f \frac{\lambda}{\Lambda_x}. \quad (6.7)$$

The actual FOV is limited by the presence of these secondary peaks, which bring ambiguity about the position of the optically generated signal. These secondary peaks scan with the focus and have an amplitude which modulates with the envelope, w_{MAX} . In this way, the intensity of the secondary peaks may surpass the primary focus intensity when the secondary peaks are near the primary. To increase the distance between the peaks the distance between cores must be decreased, however this introduces core-to-core coupling.

6.4.4 - Scanning limitations imposed by core-to-core coupling

To understand the effect of core-to-core coupling on the memory effect range, we modeled focusing with a one-dimensional waveguide array with varying core pitch. The model allowed simulation of focusing with a quadratic phase at the waveguide input, or focusing with DPC. The DPC simulation was carried out by performing the following steps: (1) a beam propagation method (BPM, [20]) step performs the propagation of a focus spot for a plane in front of the waveguide to the waveguide's distal facet; (2) the calculated field at the distal facet is coupled to the waveguide array. Coupled mode theory (CMT, [21]) is used to calculate the propagation through the array to the proximal facet of the waveguide; (3) to simulate DPC the field at the waveguide proximal end is phase conjugated and a new CMT step is performed; (4) a last BPM step takes the field at the fiber's output facet and propagates it back to recreate the focus.

In the presence of coupling between the cores, a quadratic phase at the input of the waveguide array is not enough to generate a focus spot, because coupling prohibits the relative phase at the input of the array from being directly transferred to the output. As discussed previously, DPC records the phase pattern at the proximal end of the waveguide array, which generates a focus spot by taking into account the core-to-core coupling. The simulation results in Figure 6.7 illustrate two scenarios with two arrays of 21 waveguides: no coupling and core-to-core coupling scenarios. The cores of the array have a diameter $d = 1 \mu\text{m}$, the cladding refractive index is $n_0 = 1.47$ and the core refractive index is $n_1 = 1.5$, so the waveguides are single-mode for $\lambda = 633 \text{ nm}$. The simulated arrays have core pitch of $\Lambda_x = 5 \mu\text{m}$ (no coupling) and $\Lambda_x = 3.5 \mu\text{m}$ (coupling) and a length of 30 cm. Figure 6.7(a) shows that in the no coupling case there is no difference between focusing with a quadratic phase or with DPC. However, in case core-to-core coupling is present (Figure 6.7(b)) the focusing ability is lost with quadratic phase focusing, but it is preserved when DPC is performed.

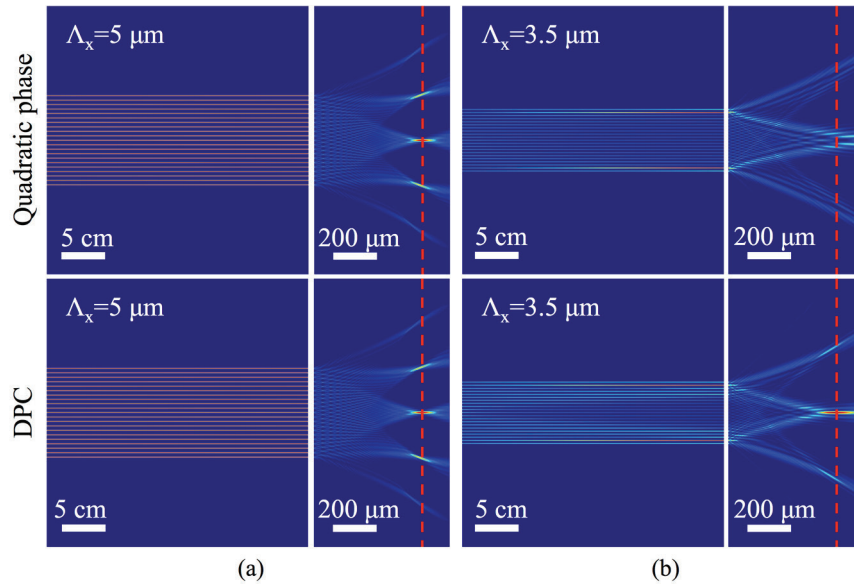


Figure 6.7: **Focusing through a waveguide array in no-coupling and coupling conditions.** The propagation in the waveguide array was simulated using coupled mode theory and the free space propagation with the beam propagation method. (a) Focusing in no coupling conditions is possible by assigning a quadratic phase at the input of the waveguide array. The phase relationship between the cores is preserved along the waveguide and it is possible to focus at a given distance for the waveguide facet ($400 \mu\text{m}$ in this case). Focusing using DPC gives equivalent results. (b) In coupling conditions, the phase relationship between cores is not preserved along the waveguide and focusing using a quadratic phase pattern is no longer possible. DPC allows focusing in severe coupling conditions.

We further investigated the effect of core-to-core coupling on the scan range by varying the coupling conditions and introducing a linear phase gradient. The phase gradient was added to the output of step (2) before performing step (3). In this way we scanned the DPC focus spot and evaluated the effect of coupling in reducing the scanning range. Figure 6.8 shows

the peak intensity of the DPC spot for different tilt angles of the input beam. The curves show the scanning range as a function of the core-to-core distance, Λ_x . In the absence of coupling, where $\Lambda_x = 5 \mu\text{m}$, the scanning range matches the one described by equation 6.7. When decreasing Λ_x the increased coupling decreases the scanning range.

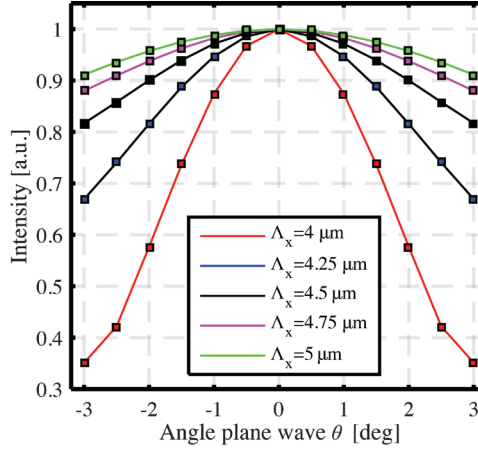


Figure 6.8: **Scanning range in a waveguide array using digital phase conjugation: coupling dependence.** By tuning the distance between the cores it is possible to change the coupling strength. Increased coupling decreases the scanning range. The green curve represents the no-coupling conditions, which yields the maximum scanning range.

6.5 - Single calibration pattern projection

Thanks to the memory effect, it is also possible to generate patterns with a single calibration hologram and project multiple focused spots within the memory effect range of the MCF. We have already seen that the phase of a plane wave having a carrier frequency $\vec{K} = (K_x, K_y)$ can be used to display the phase-conjugated spot in different locations (see equation 6.1). Since our system is linear, we can combine multiple tilted beams in order to simultaneously project focus spots in multiple locations. In this case the phase to project on the SLM is given by:

$$\phi_{SLM}(x, y) = \arg \left[e^{j\phi_{DPC}(x, y)} \sum_i e^{j(K_{xi}x + K_{yi}y)} \right]. \quad (6.8)$$

The plane waves have to be combined in the right way in order to properly project a desired pattern. To find the right combination we can start by observing that the focusing plane and the MCF distal end form a Fourier pair. In fact the DPC process creates at the output of the MCF fiber the equivalent of a lens phase, which brings the far field onto the focal plane. This is why a tilted wave imposed on the SLM results in a shift in the focusing plane. The pattern to project using the phase conjugated spot can be considered as the convolution between the spot itself and the pattern whose points can be reached using a specific carrier frequency \vec{K} . For the convolution theorem we know that this convolution in

the focal plane corresponds to a multiplication between the pattern able to produce the spot (the lens phase) and the inverse Fourier transform (*IFT*) of the desired pattern at the distal end of the MCF.

If we indicate our pattern as a function of carrier frequencies as $\tilde{O}(k_x, k_y)$, the SLM pattern will be:

$$\phi_{SLM}(x, y) = \arg \left[e^{j\phi_{DPC}(x, y)} IFT \left\{ \tilde{O}(k_x, k_y) \right\} \right]. \quad (6.9)$$

Figure 6.9(a) and Figure 6.9(b) show the projection of a cross pattern when the two arms are in phase and out of phase, respectively, while Figure 6.9(c) shows a nine focus spot projection.

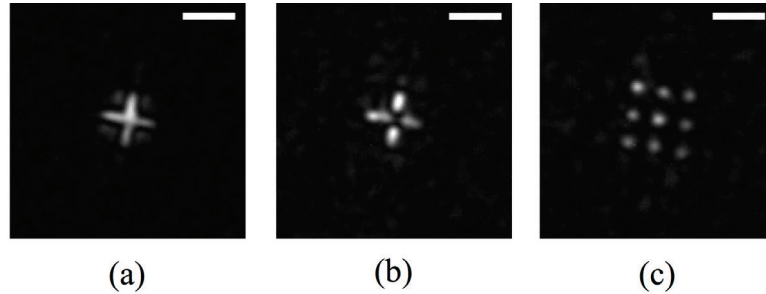


Figure 6.9: **Pattern projection using a single calibration hologram.** (a) cross obtained as a combination of shifted spots; (b) the same pattern as (a) except the spots of one arm are in opposite phase to those of the other arm; (c) multiple spot projection, in this case nine spots are projected simultaneously in a regular grid. Scale bars are 5 μm .

Figure 6.9(a) shows visible imperfections around the cross pattern, namely four blurred spots in the four quadrants created by the cross. These artifacts (or unwanted light) are due to the way the light beam is modulated at the entrance of the MCF. Even if there were no coupling (assuming the phase relationship between cores does not change from the input to the output of the fiber) the four spots would appear because of the phase-only modulation we applied with the SLM.

To demonstrate this we simulated free space propagation from the fiber facet to the focal plane using again BPM simulations. We considered as an input field the facet of our MCF, where only the fundamental mode is exiting the cores. In this case we did not simulate the propagation inside the fiber, but we assumed we could shape the phase directly at the distal end of the MCF and infinite memory effect. For the simulations we use $\lambda = 785 \text{ nm}$ and a propagation distance of 220 μm .

As said before, the DPC operation produces the phase pattern of a converging lens at the output of the MCF and the light focuses at the same location where the calibration beam was. The focusing operation is simulated in Figure 6.10: we assigned a converging phase assuming a phase only modulation (same amplitude for all the cores). Adjusting the contrast

of the simulation output image, the peaks around the main focus, due to the quasi-periodicity of the MCF, are visible as in Figure 6.2(c).

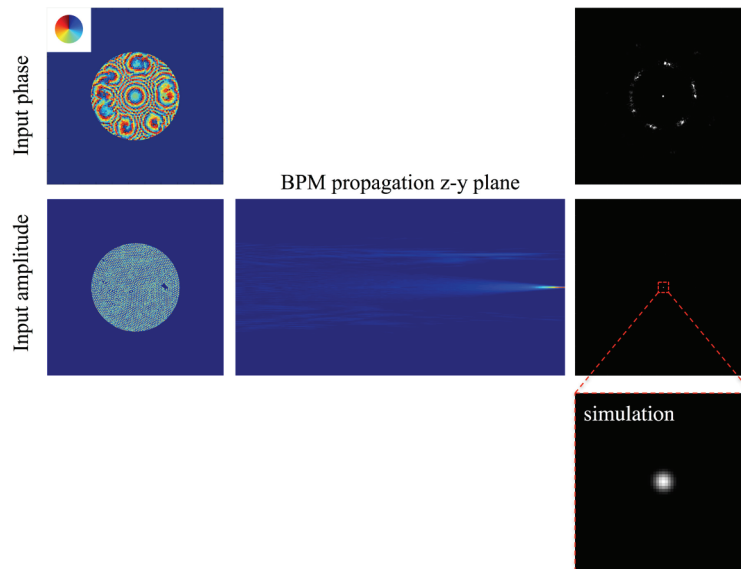


Figure 6.10: **Beam Propagation Method simulation: focusing using a multicore fiber.** In the simulation we assumed we could recreate a converging phase pattern at the distal end of the MCF. The left column shows the phase and the amplitude of the simulation. The central column shows the amplitude of the light propagation in free space from the MCF facet to the focal plane (220 μm propagation, $\lambda = 785 \text{ nm}$). The right column shows the intensity at the output of the simulation. A focus spot is created at the center of the computational window. The extra peaks that appear on the top image are due to the quasi-periodicity of the MCF.

Figure 6.11 shows the simulation and the experimental results of a cross projection obtained in the same conditions. This shows that, even with a perfect control of the propagation through the MCF, the phase only modulation operated by the SLM leads to the same imperfections in the projected pattern.

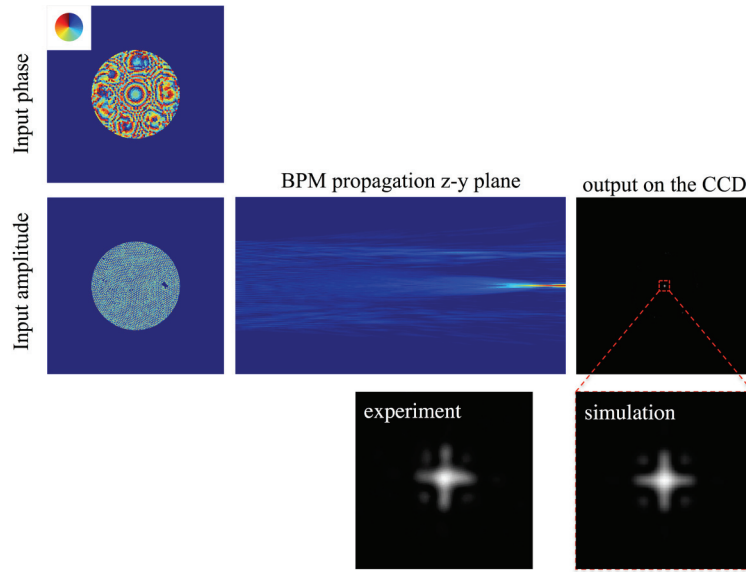


Figure 6.11: **Beam Propagation Method simulation: projection of cross pattern using a multicore fiber (phase only modulation).** The input phase is shaped in order to recreate a cross pattern 220 μm away from the fiber facet. The amplitude is assumed to be constant across the whole MCF. The intensity output shows a pattern consisting of the wanted cross and four extra spots due to the phase only modulation. The experimental result shows very high resemblance to the simulated result.

A perfect control of the amplitude, as shown in Figure 6.12 projects a cross pattern without the surrounding noise observed experimentally and in the previous simulations. This means that we need the field leaving our SLM, $A(x,y)$, to be:

$$A(x,y) = e^{j\phi_{DPC}(x,y)} IFT \left\{ \tilde{O}(k_x, k_y) \right\} = \left| IFT \left\{ \tilde{O}(k_x, k_y) \right\} \right| e^{j\phi_{DPC}(x,y)} e^{j\arg[IFT\{\tilde{O}(k_x, k_y)\}]}. \quad (6.10)$$

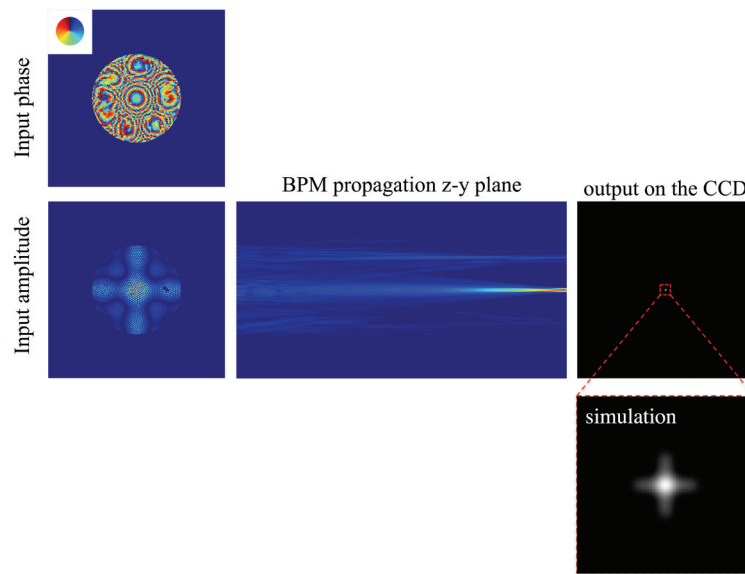


Figure 6.12: **Beam Propagation Method simulation: projection of cross pattern using a multicore fiber (phase and amplitude modulation).** The input phase is shaped in order to recreate a cross pattern 220 μm away from the fiber facet. The amplitude is shaped accordingly to the amplitude of the inverse Fourier transform of the cross pattern (see equation 6.10). The intensity output shows a pattern consisting of the wanted cross.

The importance of having control over the amplitude of the input beam is even more important when more extended patterns have to be displayed. In the following figures we show the projection of a square pattern and a continuous line pattern. While the control of the amplitude of the input beam would lead to the projection of the desired pattern (not shown), the use of only the phase information would result in the projection of patterns where only the edges are visible due to the missing amplitude information (edge enhancement).

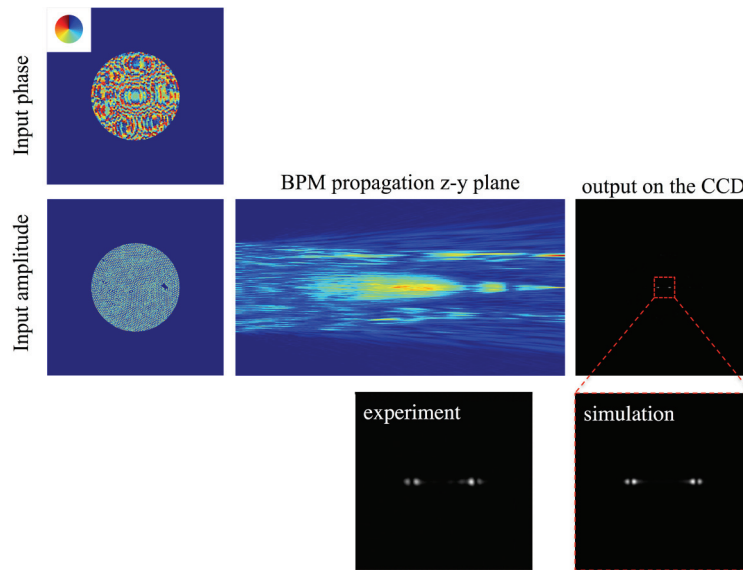


Figure 6.13: **Beam Propagation Method simulation: projection of a line using a multicore fiber (phase only modulation).** The projection of an extended pattern such as a line using a phase only spatial light modulator results in missing low frequency components and enhanced edges.

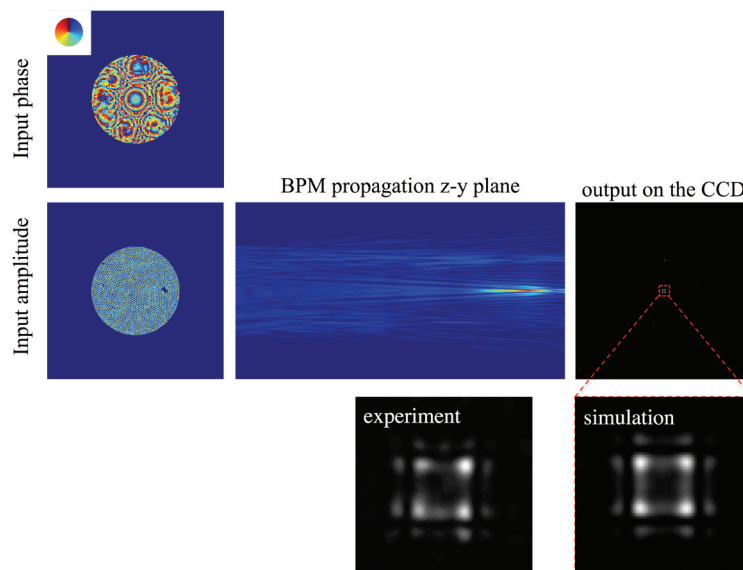


Figure 6.14: **Beam Propagation Method simulation: projection of a square pattern using a multicore fiber (phase only modulation).**

6.5.1 - Pattern projection encoding amplitude and phase on the SLM: Gerchberg-Saxton algorithm

In order to project intensity patterns using the phase only SLM we first implemented the Gerchberg-Saxton algorithm [22]. Using this iterative algorithm it is possible to calculate the phase at an input plane needed to project a given intensity in a separated plane linked to the first via a propagating function. Assuming as two planes of interest the MCF facet and the focal plane, we can consider the two planes, as said before, as a Fourier pair and use the Fourier transform operation as a propagating function. Let $R(x,y)$ and $\tilde{O}(k_x,k_y)$ be the source field (the Gaussian beam impinging the SLM) and the desired pattern in the Fourier plane, respectively. The algorithm starts with a guess of the input field $A(x,y)$, which is composed of the known source field and a guess of the SLM phase $\phi(x,y)$. The n^{th} iteration of the algorithm performs the following steps:

$$\begin{aligned}
 \tilde{A}_n(k_x,k_y) &= FT\{A_n(x,y)\} \\
 \theta_n(k_x,k_y) &= \arg\{\tilde{A}_n(k_x,k_y)\} \\
 \tilde{A}'_n(k_x,k_y) &= |\tilde{O}(k_x,k_y)| e^{j\theta_n(k_x,k_y)} \\
 \phi_{n+1}(x,y) &= \arg\left[IFT\{\tilde{A}'_n(k_x,k_y)\}\right] \\
 A_{n+1}(x,y) &= |R(x,y)| e^{j\phi_{n+1}(x,y)}.
 \end{aligned} \tag{6.11}$$

As a first test we considered the projection of 5 focus spots using the MCF. The results of this experiment are shown in Figure 6.15. After the calibration step, the phase-conjugated focus spot (Figure 6.15(a)) is displayed in multiple locations using only the phase of the *IFT* of the desired pattern, as in equation 6.9. Using only the phase information, extra lobes are formed around the projected pattern, as clearly shown in the inset of Figure 6.15(b). The output of the GS algorithm finds a phase pattern such that light only focuses in the 5 desired locations (Figure 6.15(c)).

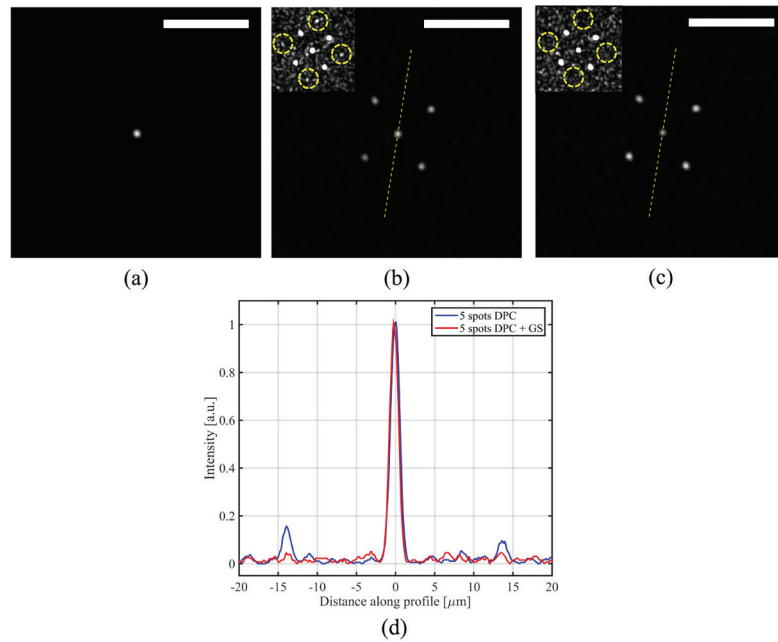


Figure 6.15: **Multiple spots projection using a multicore fiber.** (a) Phase conjugation of a single focus spot in the calibration position. (b) Projection of 5 spots using a phase only modulation: the missing amplitude information brings to the creation of extra spots around the desired pattern (the inset shows a saturated version of (b)). (c) Projection of 5 spots using a phase only modulation and GS algorithm. The use of the GS algorithm maximizes the amount of light sent to the desired pattern eliminating the presence of the extra foci (see inset and (d)). Scale bars are 10 μm .

Although the GS algorithm works well for sparse patterns, the projection of patterns such as lines or squares is still not optimal, as shown in Figure 6.16. The first column shows the intensity pattern we want to project through the MCF. The second column shows again the results previously described in Figure 6.13 and Figure 6.14, where the projection of the line and the squared were obtained assigning to the SLM the phase of the IFT of the desired pattern multiplied by the phase needed to perform the DPC, $\phi_{DPC}(x,y)$. The third column shows the projections obtained combining the phase $\phi_{DPC}(x,y)$ and the output of the GS algorithm. In this case the algorithm actually confines most of the light within the designated area. However, the intensity of the projected pattern is not homogeneous and presents speckle artifacts. The algorithm described in the set of equations 6.11, in fact, controls the amplitude of the pattern in the focusing plane, but not the phase. The phase, that can randomly vary, plays an important role. For example, if two adjacent points become out of phase after optimization, destructive interference produces unwanted variations in the intensity, generating speckles.

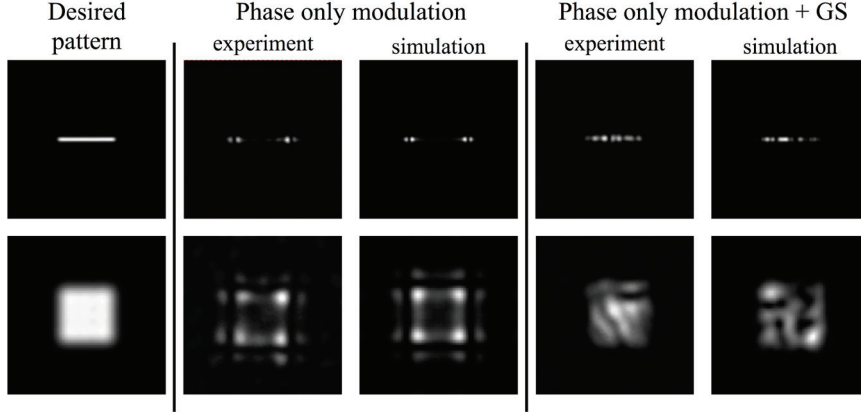


Figure 6.16: Pattern projection using a multicore fiber: GS algorithm.

6.5.2 - Pattern projection encoding amplitude and phase on the SLM: J.A. Davis encoding

In order to have a complete control over the amplitude and phase of the projected fields using a phase only SLM, we implemented the technique proposed by Davis et al. in [23]. As described in **Chapter 2**, when performing DPC, we display on the SLM the phase pattern able to focus light in front of the fiber and a grating phase pattern used to separate the useful information displayed onto the SLM from its direct reflections. The reflections (or zero diffraction order) are filtered out by the optical system and the first diffraction order of the phase grating forces the readout beam to follow the calibration path in the reverse direction, performing DPC. The technique proposed in [23] allows spatial modification of the efficiency of the diffraction into the first diffraction order by modulating the depth of the phase grating. Here we briefly give a qualitative explanation of the phenomenon as described in [23].

The transmission of a phase only grating is given by:

$$T(x) = e^{j\frac{2\pi}{\Lambda_x}Mx}, \quad (6.12)$$

where M is a modulation factor and Λ_x is the period of the grating. If $M = 1$, we have a normal blazed grating. In this first case, all the light is diffracted into the first (and only) diffraction order. If M decreases to 0.5, the light diffracts also into other orders. The grating described in equation 6.12, in fact, can be seen as the Fourier series:

$$T(x) = \sum_{n=-\infty}^{+\infty} T_n e^{j\frac{2\pi}{\Lambda_x}nx}, \quad (6.13)$$

where T_n is given by:

$$T_n = e^{j(n-M)\pi} \frac{\sin \pi(n-M)}{\pi(n-M)} = e^{j(n-M)\pi} \text{sinc}(n-M). \quad (6.14)$$

The diffraction pattern of this phase grating can be calculated by taking the Fourier transform of equation 6.13. This results in:

$$\tilde{T}(k_x) = \sum_{n=-\infty}^{+\infty} T_n \delta\left(x - \frac{n}{\Lambda_x}\right), \quad (6.15)$$

The diffraction pattern is a linear combination of delta functions separated by a distance n/Λ_x and with amplitude T_n . The light intensity that goes into each order can then be calculated as $|T_n|^2$. Assuming that the input is a plane wave of total intensity 1, for $M = 1$ we have:

$$|T_n|^2 = \left| e^{j(n-1)\pi} \text{sinc}(n-1) \right|^2 = \begin{cases} 0 & \text{for } n = 0 \\ 1 & \text{for } n = 1 \end{cases}$$

so all the light goes into the first diffraction order, as expected. Varying the modulation factor M to, for example, 0.6, the light intensity gets spread into more orders. The light that goes into the first order is about the 41% of the total. Another 41% goes into the zero diffraction order and the rest of the light is distributed into the other orders. Varying the modulation factor we can change the amount of light that goes into the first diffraction order.

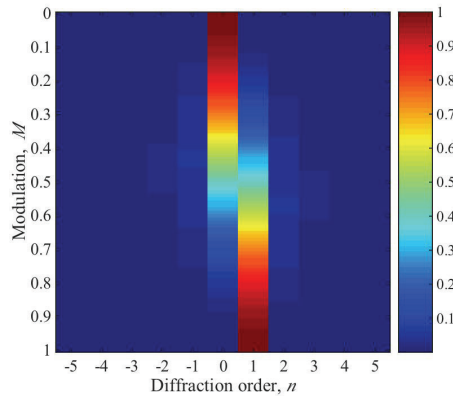


Figure 6.17: **Amplitude modulation: diffraction efficiency into different orders.**

If the modulation M varies spatially:

$$T(x) = e^{j\frac{2\pi}{\Lambda_x} M(x)x}. \quad (6.16)$$

In this case the percentage of light that goes into the first diffraction order will spatially vary as well. The relationship between M and the actual amount of light that goes into the first diffraction order is not linear. For this reason, a lookup table was created in order to figure out what modulation, M , has to be set in order to obtain a given amplitude modulation (for more details see [23]).

With this approach, we could project patterns through the MCF with improved quality. In fact, by projecting both amplitude and phase, we have full control over the field leaving the SLM, with the possibility of encoding in our reconstruction beam all the terms shown in equation 6.10, needed for the pattern reconstruction. Figure 6.18 shows experimental results of the projection of a single focused spot obtained by DPC, and the line that could be obtained encoding amplitude and phase modulation on the phase only SLM. Respect to the results shown in Figure 6.16, the projected line does not show edge enhancement or discontinuities in the intensity profile.



Figure 6.18: **Pattern projection through a multicore fiber: line projection (amplitude and phase modulation)**. Projection of a DPC focus spot and the line obtained using the same single calibration. Scale bars are 10 μm .

Figure 6.19 shows the projection of the letters which compose the acronym EPFL and the comparison between the patterns projected using the MCF and the desired pattern. Figure 6.20 shows the projection of more complex patterns, such as the SPIE and OSA logos and the entire word ‘epfl’. None of these patterns show speckle effects, or discontinuities present when using the Gerchberg-Saxton algorithm.

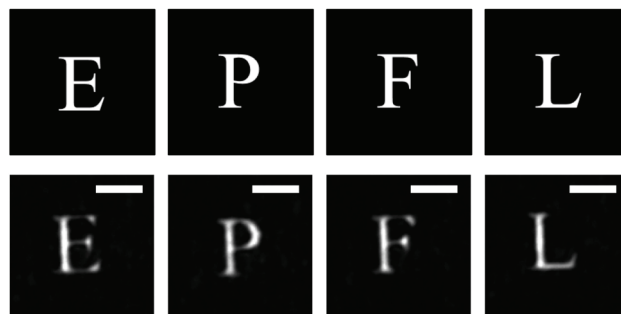


Figure 6.19: **Pattern projection through a multicore fiber: single characters (amplitude and phase modulation)**. Upper row: desired patterns. Lower row: projected pattern. Scale bars are 20 μm .



Figure 6.20: **Pattern projection through a multicore fiber: complex patterns (amplitude and phase modulation)**. Upper row: desired patterns. Lower row: projected pattern. Scale bars are 20 μm .

6.6 - Focus spot preservation in a bent fiber

Another interesting property of MCF was observed during bending of the optical fiber. Bending a fiber, in fact, changes the relative phase relationship between neighboring cores. When bent along a single axis a linear phase gradient, similar to the one used to steer the beam, should be introduced relative to the initial field. To test this, we created a calibration focus 225 μm away from the MCF distal end facet with the objective OBJ2. The complex field recorded by the CMOS when the MCF is not bent has a phase $\phi_1(x, y)$. After bending the fiber (Figure 6.21(a)), by translating the calibration block to position $p = i$, the recorded phase pattern $\phi_i(x, y)$ changes compared to the initial pattern because of the altered conformation of the optical fiber. If the phase change is too dramatic, $\phi_i(x, y)$ cannot be used to recreate a focused spot in the plane S . The 2D maps in Figure 6.21(b) show the difference between the phase in the bending position $p = i$ and the reference position $p = 1$, given by:

$$\Delta\phi = \phi_i(x, y) - \phi_1(x, y). \quad (6.17)$$

Figure 6.21(b) clearly shows that a transverse linear phase has been introduced across the MCF compared to the reference wavefront $\phi_1(x, y)$. The phase is a result of the path length differences across the cores induced by the bent fiber. In Figure 6.21(c) the focus spot is shown to shift spatially because of the linear phase added to the field across the MCF. This happens in the same way that the focus was steered by adding the linear phase with an SLM.

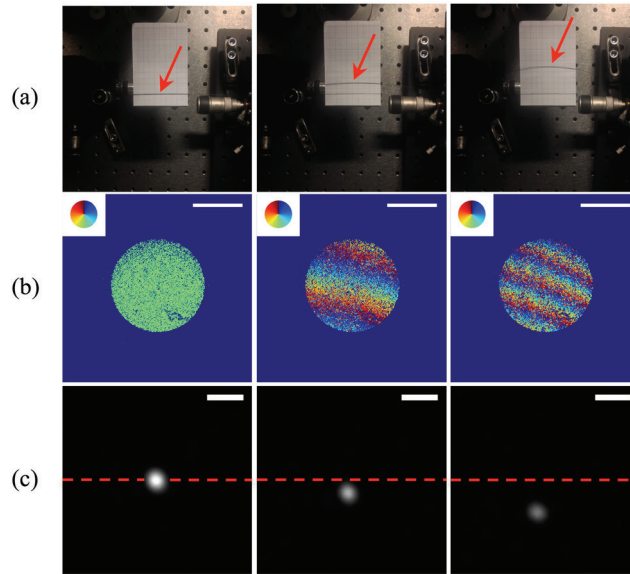


Figure 6.21: **Bending of a multicore fiber during digital phase conjugation.** (a) The translational stage where one end of the MCF is mounted is shifted to three different positions to increase fiber bending. The red arrows indicate the MCF. (b) For each bending position, a digital hologram is recorded on the CMOS: the three figures represent the difference between the extracted phase for each hologram and the phase obtained when the fiber is not bent. The insets show the color code used to represent the phase value. Scale bars are 100 μm . (c) The induced linear phase gradient across the fiber leads to a transverse shift of the focus spot in the plane S during DPC. The dashed red line indicates the position of the focus spot of an unbent fiber. Scale bars are 5 μm .

6.7 - Conclusions

Here we demonstrated that, by using a single hologram during the calibration step, a diffraction limited focused spot could be formed at the tip of a MCF and raster scanned in a regular pattern thanks to the memory effect. We have shown that a spot can be scanned transversely over several micrometers. This scanning range could be further improved by reducing the coupling events in the MCF which could be done by decreasing the number of modes per core, for example with smaller core diameters. In fact, by reducing the number of high-order modes, we can reduce coupling. Another way to increase the scanning range would be using a shorter fiber to reduce coupling along the MCF length. In this work, we used 30 cm long fibers, but many endoscopic applications are compatible with imaging probes only a few centimeters in length.

Knowledge of the scanning intensity decay could be used to compensate the acquired signal strength during fluorescence imaging depending on the focused spot position. Furthermore, since the scan is made by simply introducing a linear tilt to the calculated phase pattern, this could be implemented by imaging the SLM on a pair of galvomirrors, which in turn would be imaged on the facet of the MCF. In this way, a liquid crystal SLM could be used to project the phase pattern to focus light, while the spot scanning would be

achieved by tilting the galvomirrors. The scan speed could be increased to overcome speed limitations placed by the low refresh rate of liquid crystal SLMs.

As with other techniques based on wavefront shaping through optical fibers, this focusing technique depends on the conformation of the optical fiber. A clear advantage of the proposed implementation is that the calibration is extremely fast, since it requires a single hologram. This presents the possibility of calibration of a single, scannable focus spot during imaging. As an example, the light beacon presented in [24] could perform this function. Thus, in this case, while bending the fiber, a light beacon would allow a real time recalculation of the pattern to focus light. In this chapter we have also shown that the single calibration hologram is enough to project complex patterns within the memory effect of the MCF, that can be potentially used for patterned photo-stimulation, for example for optogenetics applications [25]. We showed that, in this case, an amplitude modulation is necessary in order to have full control of the projected light pattern.

Bibliography

- [1] N. Stasio, D. B. Conkey, C. Moser, and D. Psaltis, “Light control in a multicore fiber using the memory effect,” *Opt. Express*, vol. 23, no. 23, pp. 30532–30544, Nov. 2015.
- [2] N. Stasio, D. Conkey, C. Moser, and D. Psaltis, “The Memory Effect in Multicore Fibers,” in *Imaging and Applied Optics 2016 (2016)*, paper ITh1F.1, 2016, p. ITh1F.1.
- [3] S. Bianchi and R. D. Leonardo, “A multi-mode fiber probe for holographic micromanipulation and microscopy,” *Lab. Chip*, vol. 12, no. 3, pp. 635–639, Jan. 2012.
- [4] A. M. Caravaca-Aguirre, E. Niv, D. B. Conkey, and R. Piestun, “Real-time resilient focusing through a bending multimode fiber,” *Opt. Express*, vol. 21, no. 10, pp. 12881–12887, May 2013.
- [5] I. N. Papadopoulos, S. Farahi, C. Moser, and D. Psaltis, “Focusing and scanning light through a multimode optical fiber using digital phase conjugation,” *Opt. Express*, vol. 20, no. 10, p. 10583, May 2012.
- [6] I. N. Papadopoulos, S. Farahi, C. Moser, and D. Psaltis, “High-resolution, lensless endoscope based on digital scanning through a multimode optical fiber,” *Biomed. Opt. Express*, vol. 4, no. 2, p. 260, Feb. 2013.
- [7] T. Čížmár and K. Dholakia, “Exploiting multimode waveguides for pure fibre-based imaging,” *Nat. Commun.*, vol. 3, p. 1027, Aug. 2012.
- [8] Y. Choi *et al.*, “Scanner-Free and Wide-Field Endoscopic Imaging by Using a Single Multimode Optical Fiber,” *Phys. Rev. Lett.*, vol. 109, no. 20, p. 203901, Nov. 2012.
- [9] L. V. Amitonova, A. P. Mosk, and P. W. H. Pinkse, “Rotational memory effect of a multimode fiber,” *Opt. Express*, vol. 23, no. 16, pp. 20569–20575, Aug. 2015.
- [10] D. Kim *et al.*, “Toward a miniature endomicroscope: pixelation-free and diffraction-limited imaging through a fiber bundle,” *Opt. Lett.*, vol. 39, no. 7, pp. 1921–1924, Apr. 2014.
- [11] E. R. Andresen, G. Bouwmans, S. Monneret, and H. Rigneault, “Toward endoscopes with no distal optics: video-rate scanning microscopy through a fiber bundle,” *Opt. Lett.*, vol. 38, no. 5, p. 609, Mar. 2013.
- [12] E. R. Andresen, G. Bouwmans, S. Monneret, and H. Rigneault, “Two-photon lensless endoscope,” *Opt. Express*, vol. 21, no. 18, p. 20713, Sep. 2013.
- [13] S. Feng, C. Kane, P. A. Lee, and A. D. Stone, “Correlations and Fluctuations of Coherent Wave Transmission through Disordered Media,” *Phys. Rev. Lett.*, vol. 61, no. 7, pp. 834–837, Aug. 1988.
- [14] I. Freund, M. Rosenbluh, and S. Feng, “Memory Effects in Propagation of Optical Waves through Disordered Media,” *Phys. Rev. Lett.*, vol. 61, no. 20, pp. 2328–2331, Nov. 1988.
- [15] C. Bellanger, A. Brignon, J. Colineau, and J. P. Huignard, “Coherent fiber combining by digital holography,” *Opt. Lett.*, vol. 33, no. 24, p. 2937, Dec. 2008.
- [16] A. J. Thompson, C. Paterson, M. A. A. Neil, C. Dunsby, and P. M. W. French, “Adaptive phase compensation for ultracompact laser scanning endomicroscopy,” *Opt. Lett.*, vol. 36, no. 9, pp. 1707–1709, May 2011.
- [17] K. L. Reichenbach and C. Xu, “Numerical analysis of light propagation in image fibers or coherent fiber bundles,” *Opt. Express*, vol. 15, no. 5, p. 2151, 2007.
- [18] X. Chen, K. L. Reichenbach, and C. Xu, “Experimental and theoretical analysis of core-to-core coupling on fiber bundle imaging,” *Opt. Express*, vol. 16, no. 26, p. 21598, Dec. 2008.

- [19] I. M. Vellekoop and A. P. Mosk, “Focusing coherent light through opaque strongly scattering media,” *Opt. Lett.*, vol. 32, no. 16, pp. 2309–2311, Aug. 2007.
- [20] K. Okamoto, *Fundamentals of Optical Waveguides*. Academic Press, 2010.
- [21] A. Yariv and P. Yeh, *Photonics: Optical Electronics in Modern Communications*. Oxford University Press, 2007.
- [22] R. W. Gerchberg and W. O. Saxton, “A practical algorithm for determination of phase from image and diffraction plane picture,” *Optik*, vol. 35, no. 237, 1972.
- [23] J. A. Davis, D. M. Cottrell, J. Campos, M. J. Yzuel, and I. Moreno, “Encoding amplitude information onto phase-only filters,” *Appl. Opt.*, vol. 38, no. 23, p. 5004, Aug. 1999.
- [24] S. Farahi, D. Ziegler, I. N. Papadopoulos, D. Psaltis, and C. Moser, “Dynamic bending compensation while focusing through a multimode fiber,” *Opt. Express*, vol. 21, no. 19, p. 22504, Sep. 2013.
- [25] V. Szabo, C. Ventalon, V. De Sars, J. Bradley, and V. Emiliani, “Spatially Selective Holographic Photoactivation and Functional Fluorescence Imaging in Freely Behaving Mice with a Fiberscope,” *Neuron*, vol. 84, no. 6, pp. 1157–1169, Dec. 2014.

Chapter 7

Calibration-free imaging through a multicore fiber using speckle scanning microscopy

So far we have shown that, to image through optical fibers that support many modes, a calibration step is needed. Moreover, the calibration is dependent on the conformation of the optical fiber. Any change in the conformation requires a new calibration, which in general necessitates access to both sides of the fiber. In the last chapter we exploited digital phase conjugation through multicore fibers, in combination with memory effect. Coherent light can be focused and scanned at the tip of the fiber thanks to a calibration that requires a single hologram. In this way we tried to minimize the amount of information needed during the calibration step.

In this chapter we demonstrate that without a calibration step, even in the presence of core-to-core coupling, we can obtain fluorescence images with a resolution better than the core-to-core spacing. This is accomplished by taking advantage again of the memory effect present in this kind of fiber and of the statistical properties of the speckle pattern generated at the distal end of the multicore fiber when no wavefront shaping is performed.

Most of the material presented in this chapter has been published in [1]:

- **N. Stasio**, C. Moser, and D. Psaltis, “Calibration-free imaging through a multicore fiber using speckle scanning microscopy,” *Opt. Lett.*, vol. 41, no. 13, p. 3078, Jul. 2016.

7.1 - Introduction

As shown in the previous chapters, approaches based on wavefront shaping have two main drawbacks: they usually require a calibration step and the ability to image assumes that the fiber endoscope does not change its conformation. If the fiber bends, another calibration is needed which usually requires access to both sides of the endoscope. Recently it has been shown that it is possible to calculate the right wavefront in order to focus through a MMF,

even a bent one. This is possible by modeling the fiber, by knowing the refractive index profile of the MMF and its spatial conformation [2]. Calibration techniques utilized to focus light through a lensless MCFs have been described in the previous chapter and we concluded by affirming that if a light beacon is available at the distal end, it can be used to dynamically recalibrate the fiber, as was shown in [3].

We have also shown that, depending on the core-to-core coupling, phase gradients at the input of a MCF are preserved within some extent. As we described in **Chapter 6**, this effect is similar to what has been observed in thin scattering materials [4], [5]. This results in an angular “memory effect”, that can be used to scan a given pattern in the three dimensions (for example a focus spot, [6]).

Recent advancements in imaging through scattering media showed that, using the angular memory effect, it is possible to obtain an image of a sample behind a scattering layer without any calibration or wavefront precompensation [7], [8]. The approach demonstrated in [8] has been adapted to MCFs in [9], showing one-shot widefield imaging. The technique is based on the fact that, two emitting points at the same plane in the distal end will generate two shifted speckle patterns on the proximal side. Points of an object lying within the angular memory effect of the MCF can be retrieved by recording the generated speckle pattern on the proximal side and by a post-processing step [9]. In this case, the memory effect is used on the *detection side*. This is possible when the light coming from the sample is coherent or has a reduced bandwidth. An increase in bandwidth reduces the contrast of the attainable image [9].

Here we show that, using the memory effect on the *excitation side* (the distal end), we could image a fluorescent sample with broadband emission with a resolution superior to the core-to-core spacing of the MCF and without any calibration. Our only assumption is that the fiber does not change conformation during the acquisition of a single image, but it can bend arbitrarily in-between acquisitions.

7.2 - Working principle

We adapted the speckle scanning microscopy (SSM) technique described by Bertolotti et al. [7] to MCFs. Compared to the use of the technique in scattering media, SSM in MCFs has the advantage that the optical fiber delivers almost all the excitation light to the sample (whereas in a scattering material most of the light is scattered away from the sample), while collecting all the emitted fluorescence light within the *NA* of the MCF. As described in [7], if a speckle pattern is translated across a fluorescent sample, the intensity of the fluorescent signal I , as a function of the incidence angle θ , is given by:

$$I(\theta) = \int_{-\infty}^{+\infty} O(r)S(r - \Delta r)d^2r = [O * S](\theta), \quad (7.1)$$

where O is the sample, S is the speckle intensity field and $\Delta r \approx z\theta$ is the translation of the speckle S at the sample plane and z is the distance from the MCF’s facet. The fluorescence can be collected through the same MCF and integrated on a photon sensitive detector.

The averaged autocorrelation of the intensity map over N different scans can be expressed as:

$$\langle I \star I \rangle(\Delta\theta) = \langle O \star S \rangle \star \langle O \star S \rangle = \langle O \star O \rangle \star \langle S \star S \rangle, \quad (7.2)$$

where \ast and \star are the convolution and correlation operators, respectively, and $\langle \rangle$ represents an average over N speckle realizations (in practice different scans, [7]). This means that we are probing the autocorrelation of the object O convolved with the autocorrelation of the speckle pattern S . Multiple instances of the speckle autocorrelation are averaged to obtain a peaked function with a low random background [10], so that the autocorrelation of the acquired intensity $I(\theta)$ can be approximated by the object autocorrelation. At the same time we know that:

$$FT \{O \star O\} = FT \{O\} FT \{O\}^* = |FT \{O\}|^2 \quad (7.3)$$

where $FT \{ \}$ is the Fourier transform operator. This means that the knowledge of the autocorrelation of O give access to the amplitude of its Fourier transform, but not to its phase. We obtained the phase using a phase retrieval algorithm. For our experiments we used the Hybrid Input-Output algorithm and the Error Reduction algorithm (both described in [11]). Once we have access to both amplitude and phase of the Fourier transform of the object, it can be calculated simply with an inverse Fourier transform operation.

The algorithm starts with a guess of the input field $G(x,y)$ and assumes the knowledge of $|FT \{O(x,y)\}|$, which can be calculated using equation 7.3. The n^{th} iteration of the algorithm performs the following steps:

$$\begin{aligned} \tilde{G}_n(k_x, k_y) &= FT \{G_n(x, y)\} \\ \theta_n(k_x, k_y) &= \arg \{ \tilde{G}_n(k_x, k_y) \} \\ \tilde{G}_n'(k_x, k_y) &= |FT \{O(x, y)\}| e^{j\theta_n(k_x, k_y)} \\ G_n'(x, y) &= IFT \{ \tilde{G}_n'(k_x, k_y) \}. \end{aligned} \quad (7.4)$$

It can be observed that the algorithm is very similar to the Gerchberg-Saxton algorithm described in the previous chapter. One crucial difference is that, when choosing the next input $G_{n+1}(x,y)$, some constraints are applied. In our case, since we are measuring fluorescence, the next input (the guess of the object) for the algorithm has to be real and positive. If we define γ as the domain in which these requirements are satisfied, the guess of the object at the $(n+1)^{\text{th}}$ iteration is:

$$G_{n+1}(x,y) = \begin{cases} G'_n(x,y) & \text{for } (x,y) \in \gamma \\ 0 & \text{for } (x,y) \notin \gamma \end{cases} . \quad (7.5)$$

This implementation is what we introduced above as the Error Reduction algorithm. The Hybrid Input-Output algorithm, instead, defines the next input as:

$$G_{n+1}(x,y) = \begin{cases} G'_n(x,y) & \text{for } (x,y) \in \gamma \\ G_n(x,y) - \beta G'_n(x,y) & \text{for } (x,y) \notin \gamma \end{cases} , \quad (7.6)$$

where β is a feedback parameter that helps the convergence of the algorithm.

7.3 - Speckle Scanning Microscopy in MCFs

Figure 7.1 shows the optical setup used in the experiments. It is a variation of the setups shown in the previous chapters. A 532 nm continuous wave laser beam is expanded, collimated and sent towards a spatial light modulator (SLM, Pluto-Vis, Holoeye) using a polarizing beam splitter (PBS). The facet of the SLM is imaged onto the MCF (Fujikura, FIGH-06-300S, 6000 cores, core diameter 2.5 μm , 30 cm long, core-to-core spacing 3.2 μm , $NA= 0.34$) facet by the 4f system composed of the lens L2 and the objective OBJ2. Linear phase gradients are assigned to the SLM to tilt the incidence angle of the laser beam on the MCF. The beam that reaches the MCF covers an area of 200 μm in diameter, corresponding to illuminating approximately 3000 cores. Core-to-core coupling in a MCF with coherent light results in a speckle pattern S at the output of the MCF. Thanks to the memory effect, this speckle can be spatially scanned by tilting the angle θ of the input field to the MCF using the SLM. The fluorescence from the sample is collected through the same MCF and redirected towards an avalanche photodiode (APD) using a dichroic mirror (DM). This simple setup, indicated in Figure 7.1 as SSM path, is enough to perform SSM imaging using a MCF.

As described before, the technique allows imaging a fluorescent sample after averaging N scans by using N independent speckle patterns. In [7] this was obtained by starting each scan at a different incidence angle, such that the difference in starting angles is larger than the angular size of the object (or larger than the angular memory effect range). Here we created independent speckles by assigning a random input phase to each core of the MCF. In this way we are sure about the independence of consecutive scans, and we do not need to introduce an angular difference by starting with incidence angles that may exceed the NA of the MCF.

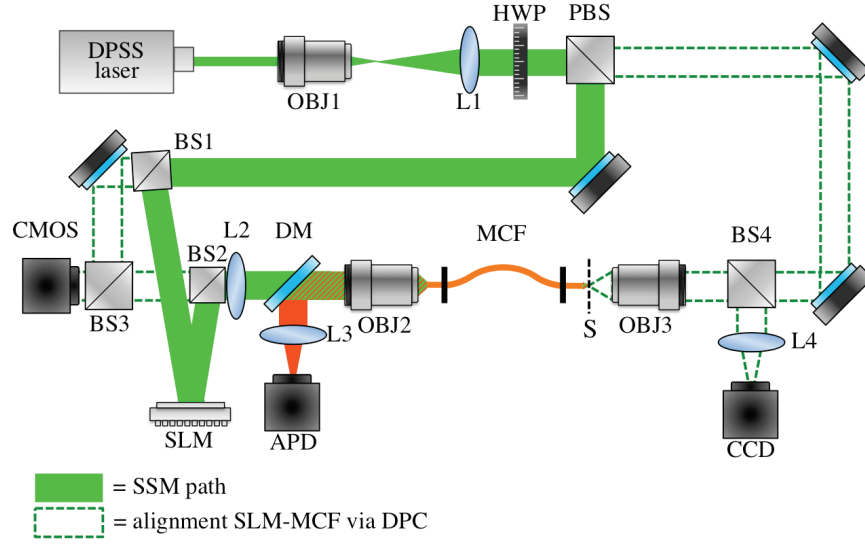


Figure 7.1: **Experimental optical setup for speckle scanning microscopy through a multicore fiber.** The output of a diode pumped solid-state laser ($\lambda = 532 \text{ nm}$) is expanded by the telescope OBJ1-L1 and is sent to the spatial light modulator (SLM) by the polarizing beam splitter (PBS). Tilted beams are created on the SLM plane, which is imaged on the MCF facet. Tilting the incidence angle on the MCF produces shifting speckle patterns in the sample plane S. For each angle of incidence, the fluorescence emitted by the sample is collected back through the MCF, reflected by a dichroic mirror (DM) and integrated by an avalanche photodiode (APD). HWP= half-wave plate; BS1= BS2 = 90% reflection 10% transmission beam splitter (90/10 R/T). BS1= BS2 = 50/50 R/T beam splitter. OBJ1= 10 \times , NA= 0.25, Newport; OBJ2= 40 \times , NA= 0.65, Newport; OBJ3 = 20 \times , NA= 0.4, Newport. Focal length lenses: L1= 150 mm, L2= L3= 200 mm, L4= 100 mm.

In order to assign random phase values to the optical fiber cores, we performed the following steps. First, the MCF facet was imaged onto the CMOS camera, illuminating the fiber with incoherent white light from the sample side (not shown in Figure 7.1). From this image, we identified the coordinates of the center of each core by calculating the center of mass of every core (this step was performed using the software ImageJ), and we created a matrix composed of delta functions at the cores coordinates:

$$C(x,y) = \sum_{i=1}^M \delta(x-x_i, y-y_i), \quad (7.7)$$

where M is the number of cores and (x_i, y_i) is the location of the i^{th} core. The matrix $C(x,y)$ was first multiplied by a matrix composed of random values between 0 and 2π , and finally convolved with a circular aperture of the size of core. This operation results in circular apertures with random phase values, placed at the cores locations:

$$\phi_{Rand}(x,y) = [C(x,y)R(x,y)] * \text{circ}\left(\frac{x}{a}, \frac{y}{a}\right), \quad (7.8)$$

where a is the radius of the cores. These steps are shown in Figure 7.2.

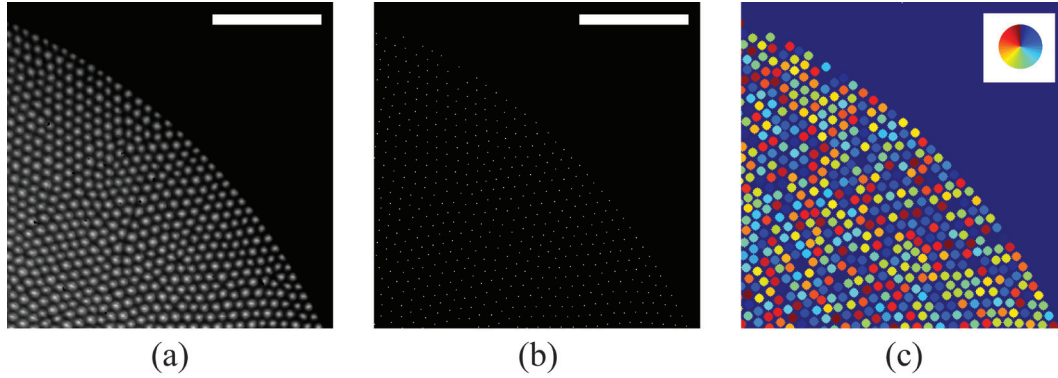


Figure 7.2: **Generation of uncorrelated speckles in a multicore fiber for speckle scanning microscopy.** (a) White light image of a portion of the MCF's facet. (b) Location of the center of mass of the cores of the MCF. (c) Random phase assigned to each core. Scale bars 30 μm .

To address the MCF cores in a predictable way, we introduced a separate *alignment* path to know exactly the correspondence between the SLM and MCF facet. This is possible by performing a digital phase conjugation of a focus spot as shown in **Chapter 6**, where the SLM is placed at the imaging plane of the MCF facet and a perfect alignment between SLM and fiber is required [12]. The CMOS camera is also placed at the imaging plane of the MCF facet and is aligned pixel-by-pixel with the SLM, so that the MCF can be mapped with one-pixel precision on the SLM. Once the mapping is obtained, the alignment path can be permanently removed and there is no need for access to the sample side.

7.4 - Experimental results

We first measured the angular memory effect of the utilized MCF. Figure 7.3(a) shows an experimental correlation map of the speckle pattern projected by the MCF as a function of the incidence angle ($\theta - \theta_0$), where θ_0 is the initial incidence angle. The speckle patterns were imaged on a CCD camera. The correlation map was formed taking the maximum of the two-dimensional cross-correlation between the speckle pattern at each angle and a reference speckle acquired for $\theta = \theta_0$. The resolution of SSM is given by the average speckle grain size [7], which in turn depends on the *NA* of the MCF and the working distance (i.e. the distance between the MCF facet and the object). Figure 7.3(c) shows the experimental mean size of the speckle grain as a function of the working distance obtained with the MCF. The speckle grain size has been calculated as the full width at half maximum (FWHM) of the autocorrelation of the speckle pattern at each working distance, in a $50 \times 50 \mu\text{m}^2$ area in front of the MCF. As shown in the curve in Figure 7.3(c), without any calibration, creating a speckle pattern and tilting the angle of the incidence beam on a MCF, it is possible to obtain sufficient information to form a fluorescence image of an object with a resolution higher than the core-to-core spacing ($3.2 \mu\text{m}$ in our case), for a large range of working distances. The technique has an infinite depth of field. A planar object can be imaged at any working

distance with a resolution decreasing with the distance from the fiber facet. This means that the technique does not have axial discrimination, as discussed in [8].

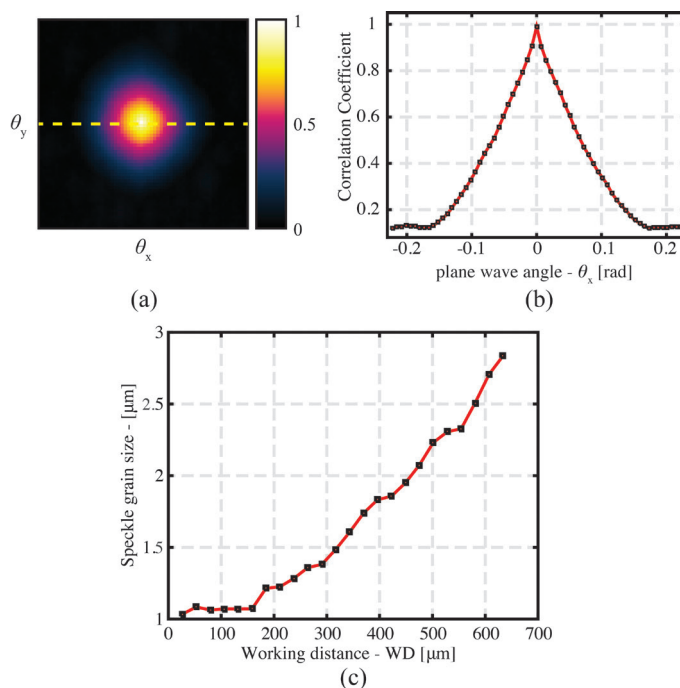


Figure 7.3: **Speckle scanning microscopy through a multicore fiber: characterization.** (a) The speckle pattern generated at the sample plane S for normal incidence on the MCF, is recorded on a CCD camera. Once the incidence angle is varied, the shifted version of the speckle is recorded and the cross-correlation with the first pattern is calculated. The intensity map represents the calculated degree of correlation as a function of the incidence angle. (b) Line profile along the yellow dashed line in (a). We consider the FWHM of this curve as memory effect range, which gives the maximum field of view. Imaging 300 μm far from the fiber facet gives a field of view of 35 μm . (c) Measured mean speckle grain size as a function of distance from the fiber facet, indicator of the resolution of the SSM technique. It has been calculated measuring the FWHM of the autocorrelation of the speckle pattern in a 50 $\mu\text{m} \times 50 \mu\text{m}$ area in front of the MCF. The lines in (b) and (c) are drawn only for clarity.

To test the SSM imaging through MCF and its resolution, we first imaged portions of a 1951 USAF resolution target (Edmund Optics) in a *transmission geometry*. The sample was placed 500 μm away from the MCF facet and imaged on the CCD through the 4f system OBJ3-L4. For each plane wave, the image on the CCD is the equivalent of the product between the shifting speckle pattern and the resolution target. An image, consisting of many features of the resolution chart, was acquired for each plane wave. We isolated from the image the pattern of the group 7 element 6 (stripes 2.19 μm wide) and the digit 7 of the group 7 in order to show that the technique has a resolution superior to the core-to-core spacing and the ability to image complex patterns, respectively. For each angle we integrated all the light transmitted through the pattern in order to obtain one point of the intensity matrix $I(\theta)$. In order to form an image, we averaged the autocorrelation of intensity maps

obtained using 20 speckle realizations. Figure 7.4 shows the experimental results. Each row represents a separate imaging experiment. The columns, from left to right, show the average autocorrelation map of 20 scans, the calculated Fourier transform of the object O , the transmission widefield image of the sample and the reconstructed object via SSM. The image reconstruction was obtained using 2000 iterations of Hybrid Input-Output algorithm [11], followed by 50 iterations of Error Reduction algorithm [11], as described in [7].

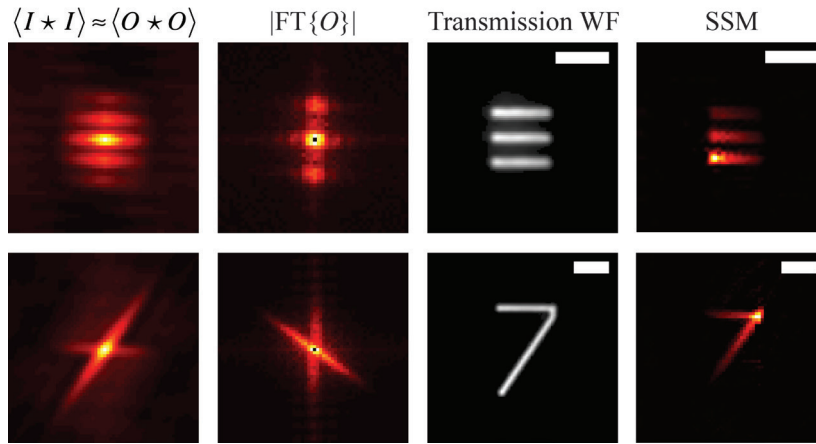


Figure 7.4: **Speckle scanning microscopy imaging through a multicore fiber: 1951 USAF target.** The four columns are respectively the autocorrelation of the intensity map $I(\theta)$, the Fourier transform of the object obtained from the autocorrelation map, the transmission widefield image of the sample and the sample imaged by SSM. Scale bars are 10 μm . The SSM image of the Group 7 Element 6 of the USAF target was 2D interpolated to double the number of pixels.

We now demonstrate the ability of fluorescent imaging using SSM in MCFs in a *reflection geometry*, with no access to the distal end. We prepared a sample depositing 1 μm diameter fluorescent beads on a 150 μm -thick microscope glass slide, and we placed it 300 μm away from the MCF facet, where, according to Figure 7.3(c) a resolution superior to 1.5 μm should be attainable. For this experiment we averaged the autocorrelation of intensity maps over 10 different speckle patterns. In Figure 7.5(a) three of these intensity maps are shown. Also in this case, the image reconstruction was obtained using 2000 iterations of Hybrid Input-Output algorithm, followed by 50 iterations of Error reduction algorithm. Figure 7.5(b) and Figure 7.5(c) show the comparison between the widefield fluorescent image of two beads 3 μm apart from each other, and the image obtain with the SSM technique through MCF. Since the distance between the two beads is comparable to the core-to-core spacing (3.2 μm), the fact that the two beads are completely resolved indicates that the resolution is finer than the inter-core distance, as predicted in Figure 7.3(c) measuring the speckle size and in Figure 7.4.

Figure 7.6 shows two additional experiments of SSM using a MCF. As in Figure 7.4, the columns, from left to right, show the average autocorrelation map of 10 scans, the calculated

Fourier transform of the object O , the fluorescence widefield image of the sample and the reconstructed object via SSM. We obtained similar images with a bent fiber, which worked unless the bending introduced too much coupling between cores and reduced the range of the memory effect [6]. Bending can also be used to change the speckle pattern between two scans, as shown in [9].

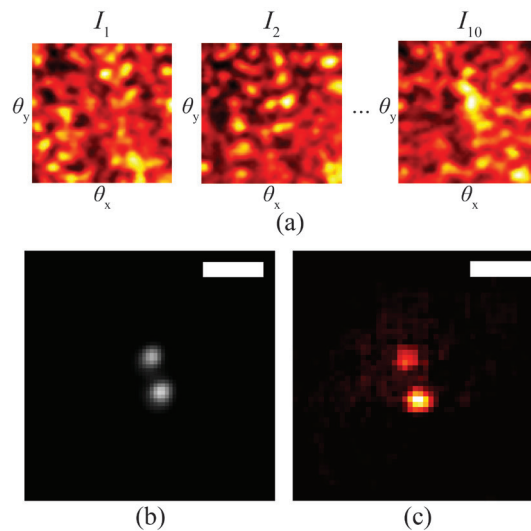


Figure 7.5: **Speckle scanning microscopy imaging through a multicore fiber: 1 μm fluorescent beads deposited on a glass slide.** (a) Example of intensity patterns $I(\theta)$ recorded by the APD. For the experiments 10 different intensity maps were acquired in order to calculate the average autocorrelation. (b) Fluorescence widefield image of the sample. (c) The sample imaged recovered by SSM. The distance between the two beads is approximately 3 μm . Scale bars are 5 μm .

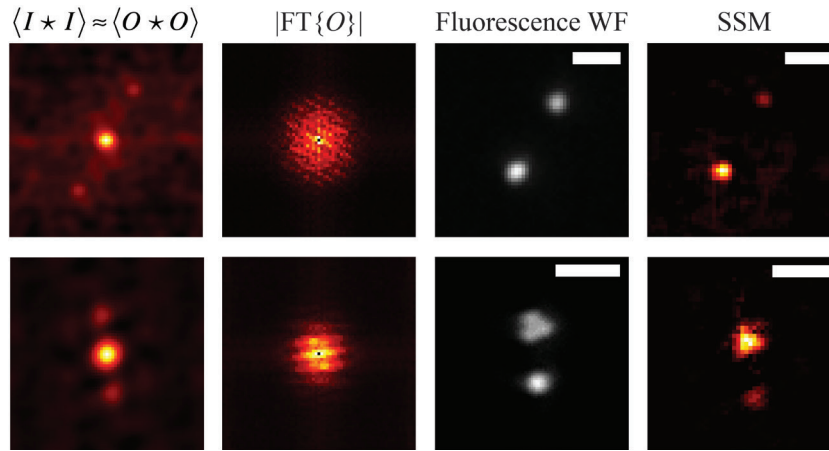


Figure 7.6: Speckle scanning microscopy imaging through a multicore fiber: $1\ \mu\text{m}$ fluorescent beads deposited on a glass slide. The four columns are respectively the autocorrelation of the intensity map $I(\theta)$, the calculated Fourier transform of the object, the fluorescence widefield image of the sample and the sample imaged by SSM. Scale bars are $5\ \mu\text{m}$.

7.5 - Conclusions

In this chapter we have demonstrated pixelation-free fluorescence imaging through MCFs of fluorescent samples with no calibration step. The SSM implementation allows obtain images with a resolution better than the core to core spacing. Bending does not affect the image quality as long as it does not happen during a single scan. In the experiments we described, an image consisting of 50×50 pixels is scanned in 125 seconds at the full speed of the SLM (maximum refresh rate is approximately 20 Hz). This speed can be drastically increased using digital micromirror devices instead, with refresh rates up to 20 kHz. Even higher speed could be obtained by scanning the incidence angle with galvo-mirrors: a quick test showed that with commercially available galvo-mirrors we can acquire five 100×100 pixel intensity maps per second (not shown here).

The obtained field of view is relatively small. This can be increased for example with a larger core-to-core spacing (which does not affect the resolution of SSM). Another way to increase the field of view would be to use a CCD camera to collect the fluorescence signal, instead of the APD. The main limiting factor for the field of view is the memory effect range. If there are two objects in the imaging plane and their distance is larger than the angular memory effect, the technique will fail. Using a CCD camera and imaging the distal facet of the MCF, we would be able to collect the fluorescence of the two objects independently thanks to the widefield imaging capability of the MCF. At this point two independent reconstructions can be run and the two SSM images can be combined in a larger image. This can enlarge the field of view considerably, as shown in [13] where SSM using scattering media was integrated with a widefield microscope.

Bibliography

- [1] N. Stasio, C. Moser, and D. Psaltis, “Calibration-free imaging through a multicore fiber using speckle scanning microscopy,” *Opt. Lett.*, vol. 41, no. 13, p. 3078, Jul. 2016.
- [2] M. Plöschner, T. Tyc, and T. Čížmár, “Seeing through chaos in multimode fibres,” *Nat. Photonics*, vol. 9, no. 8, pp. 529–535, Aug. 2015.
- [3] S. Farahi, D. Ziegler, I. N. Papadopoulos, D. Psaltis, and C. Moser, “Dynamic bending compensation while focusing through a multimode fiber,” *Opt. Express*, vol. 21, no. 19, p. 22504, Sep. 2013.
- [4] S. Feng, C. Kane, P. A. Lee, and A. D. Stone, “Correlations and Fluctuations of Coherent Wave Transmission through Disordered Media,” *Phys. Rev. Lett.*, vol. 61, no. 7, pp. 834–837, Aug. 1988.
- [5] I. Freund, M. Rosenbluh, and S. Feng, “Memory Effects in Propagation of Optical Waves through Disordered Media,” *Phys. Rev. Lett.*, vol. 61, no. 20, pp. 2328–2331, Nov. 1988.
- [6] N. Stasio, D. B. Conkey, C. Moser, and D. Psaltis, “Light control in a multicore fiber using the memory effect,” *Opt. Express*, vol. 23, no. 23, p. 30532, Nov. 2015.
- [7] J. Bertolotti, E. G. van Putten, C. Blum, A. Lagendijk, W. L. Vos, and A. P. Mosk, “Non-invasive imaging through opaque scattering layers,” *Nature*, vol. 491, no. 7423, pp. 232–234, Nov. 2012.
- [8] O. Katz, P. Heidmann, M. Fink, and S. Gigan, “Non-invasive single-shot imaging through scattering layers and around corners via speckle correlations,” *Nat. Photonics*, vol. advance online publication, Aug. 2014.
- [9] A. Porat, E. R. Andresen, H. Rigneault, D. Oron, S. Gigan, and O. Katz, “Widefield lensless imaging through a fiber bundle via speckle correlations,” *Opt. Express*, vol. 24, no. 15, pp. 16835–16855, Jul. 2016.
- [10] J. W. Goodman, *Speckle Phenomena in Optics: Theory and Applications*. Roberts and Company Publishers, 2007.
- [11] J. R. Fienup, “Phase retrieval algorithms: a comparison,” *Appl. Opt.*, vol. 21, no. 15, pp. 2758–2769, Aug. 1982.
- [12] I. N. Papadopoulos, S. Farahi, C. Moser, and D. Psaltis, “Focusing and scanning light through a multimode optical fiber using digital phase conjugation,” *Opt. Express*, vol. 20, no. 10, p. 10583, May 2012.
- [13] H. Yilmaz, E. G. van Putten, J. Bertolotti, A. Lagendijk, W. L. Vos, and A. P. Mosk, “Speckle correlation resolution enhancement of wide-field fluorescence imaging,” *Optica*, vol. 2, no. 5, p. 424, May 2015.

Chapter 8

Conclusions and outlook

In this thesis we have studied imaging through multimode optical waveguides through control of the light wavefront. The motivation for using wavefront shaping for imaging through fibers is to make the size of the endoscope as small as possible while maintaining, at the same time, a high resolution. In particular in this work we aimed to increase the amount of information that could be obtained through ultrathin optical fiber based endoscopy. We accomplished this by showing that a variety of imaging techniques can be implemented in multimode fiber imaging systems.

In **Chapters 3, 4 and 5** imaging through multimode optical fibers was obtained purely by digital phase conjugation. A calibration beam was raster scanned at the distal end of the optical fiber and digital holograms of the emerging field were recorded at the proximal side. The phase extracted from the digital holograms was utilized to form phase conjugated beams to recreate a scanning focus spot at the distal end, where the sample was positioned. The spots interrogating the sample created an emission signal that was collected through *the same fiber* and detected at the proximal end, without any sensor integrated at the distal end of the fiber.

In **Chapter 3** we used capillary waveguides to overcome a limitation that multimode fibers present in photoacoustic imaging. The photoacoustic ultrasound wave created by the interaction of a nanosecond pulsed focused beam with an absorbing sample cannot be collected through the same optical fiber. Instead of placing an ultrasound transducer at the tip of our device, that would increase the invasiveness of the endoscope, we exploited the acoustic waveguiding properties of water-filled capillary waveguides in order to detect the emission signal remotely, at the proximal side of the endoscope. We showed both photoacoustic and fluorescent images through capillary waveguides. We believe that the results presented in this chapter pave the way for an ultrathin and high-resolution endoscopic device, able to image with different modalities deep inside biological tissues while still being minimally invasive, with a total diameter of only 330 μm and with no optical or acoustic

elements on the imaging side. A future development of this kind of device could be given by the insertion of an optical fiber based ultrasound sensor in the hollow core of the capillary waveguide. This could eliminate the restriction in the length of the capillary waveguide, dictated by the attenuation of the acoustic signal traveling in the water-filled core. Moreover, we think that our approach will arouse curiosity around this type of waveguide and trigger new research, looking for new applications which combine light focusing through the multimode optical waveguide and the direct access on both sides of the waveguide itself.

In **Chapter 4** we showed how fluorescence saturation can improve imaging through optical systems based on multimode optical waveguides. The experiments were performed using regular multimode fibers, though the same techniques could be implemented utilizing capillary waveguides or multicore fibers. As we explained, the relatively low numerical aperture of the fiber limits the resolution of endoscopic imaging through multimode fibers. Exploiting saturated excitation microscopy (SAX microscopy), we demonstrated resolution improvement in all three dimensions. We obtained 500 nm lateral resolution, well below the limit of diffraction given by the numerical aperture of the fiber used. In linear fluorescent imaging, the contrast of thick sample images is limited by the absence of optical sectioning. We demonstrated out of focus light elimination by SAX can improve the image contrast. Thus, the use of SAX in MMF endoscopy by phase conjugation provides better image quality when photostable, fluorescent samples are used.

In **Chapter 5** we used multicore fibers and implemented two-photon microscopy using coherence-gated digital phase conjugation. Two-photon microscopy allowed us to obtain sectioning and imaging of samples stained using regular fluorescent dyes. We characterized the propagation of ultrafast pulses through multicore fibers and we finally demonstrated imaging of a complex 3D matrix of fluorescent beads and stained cells. Future work on the multiphoton multicore fiber endoscope should enable dual mode imaging and high speed scanning. Traditionally, multicore fibers have been used for widefield endoscopic imaging. Combining a widefield imaging modality with two-photon fluorescence imaging would provide a powerful tool for endoscope use.

We also believe that the transmission of more powerful pulses through multicore fibers would allow ablation of metals and tissues. For ablation purposes, in fact, it is not possible to send light into one core at the time, because this strategy would ablate the cores. In our case we use the contribution of all the cores, spreading the total power of the pulse across a wider region, i.e. the all multicore fiber's cores. Our approach could bring a minimally invasive device able to ablate material through multi-photon processes and verify the ultimate result of the ablation process with the imaging capability of the multicore fiber.

All the implementations we showed in these chapters rely on the stability of the fiber probe. First of all, as we have already detailed, the modal distribution in optical multimode fibers depends on the conformation of the fiber. This means that the calibration step needed for imaging is shape dependent. One possibility is to insert the endoscopic probes in a rigid jacket, such as a needle, to prevent any bending of the fiber. The probes used in **Chapters 3, 4 and 5** had an external diameter of 330 μm , 500 μm and 250 μm , respectively, including the

external coatings, which means that these fibers can be easily inserted into surgical needles already used in clinics.

The modal distribution also can be affected by temperature. Recently it was shown that a difference in temperature of 8°C is necessary to completely decorrelate the speckle pattern at the output of a 1 meter-long multimode fiber [1]. At the same time it was shown that this difference in temperature is inversely proportional to the length of the fiber. The fibers used in the whole of this thesis do not exceed 30 cm in length. Moreover, for applications where the fiber needs to be inserted with surgical needles, only a few centimeters of fiber are needed, so in these cases the temperature should not present a problem.

To face the problem posed by bending the fiber, we reduced the number of acquisitions needed during the calibration in order to perform imaging. This is studied in **Chapter 6**.

In [2] it was shown that a coherent beacon source can be used for real-time recalibration of a bending multimode fiber, allowing the focusing of light to a single location in front of the fiber. Although very powerful, the focusing remained limited to the specific location of the virtual source.

In multicore fibers, a single calibration hologram is needed to focus light in one location (as in multimode fibers), but we noticed tilting the phase conjugated beam at the entrance of the fiber results in a transverse shift of the phase conjugated focus spot. Using this memory effect, we showed that we could form images using only one calibration hologram and project complex pattern.

With use of the memory effect, two main aspects could be exploited in the future in order to improve endoscopy using multicore fibers and digital phase conjugation. The real-time recalibration studied in [2] in this case, even if working for a single location, would be sufficient to perform imaging. Moreover, since the steering of the spot is obtained by tilting the phase conjugated beam, the tilting operation could be performed by utilizing a galvo-mirror scanner instead of the spatial light modulator, thus increasing the imaging speed capable with the slow frame rate of a liquid-crystal based spatial light modulator.

Finally, in **Chapter 7**, we exploited the memory effect in a multicore fiber to implement speckle scanning microscopy. We noticed that, as we could raster scan a focus spot tilting the input of the multicore fiber, we could shift a speckle pattern in the same way. We demonstrated that by shifting an unknown speckle pattern, collecting fluorescence for every scanning position, and running a reconstruction algorithm, we could obtain an image with a resolution better than the core-to-core spacing of the multicore fiber. This method did not require any calibration with the only requirement being fiber stability during each scan. For convenience in this chapter we used a spatial light modulator to tilt the plane waves at the input of the fiber, the stability of the fiber was required for about 100 seconds. A future implementation using galvo-mirrors or a digital micromirror device in the setup would allow fast high resolution imaging through ultrathin multicore fiber, where stability would only be required for millisecond periods.

In summary, we demonstrated that a variety of imaging techniques can be implemented in optical fiber based endoscopy, maximizing the amount of information that can be collected through a probe only a few hundreds of micrometers thick. The minimal invasiveness of the developed probes gives access to areas normally inaccessible to microscope objectives.

Using digital phase conjugation we were able to perform linear and non-linear fluorescence microscopy through multimode optical fibers, demonstrating improved resolution compared to previous works and the introduction of optical sectioning capabilities. We have shown that, by exploiting their double guidance properties (optical and acoustic), water-filled capillary waveguide can be used to perform fluorescence and photoacoustic imaging. Finally, we have demonstrated imaging and pattern projection through multicore fibers at resolutions finer than the core-to-core spacing. The fast calibration operation and their double imaging modality could simplify imaging through optical fibers based on wavefront shaping.

In the future this kind of probe could also perform material ablation, or multi-photon photo-polymerization, enabling procedures in areas difficult to reach, not strictly related to imaging.

Bibliography

- [1] B. Redding, S. M. Popoff, and H. Cao, “All-fiber spectrometer based on speckle pattern reconstruction,” *Opt. Express*, vol. 21, no. 5, p. 6584, Mar. 2013.
- [2] S. Farahi, D. Ziegler, I. N. Papadopoulos, D. Psaltis, and C. Moser, “Dynamic bending compensation while focusing through a multimode fiber,” *Opt. Express*, vol. 21, no. 19, p. 22504, Sep. 2013.

Nicolino STASIO

PERSONAL INFORMATION

Born in Napoli, Italy, 12 March 1986

email

nicolino.stasio@epfl.ch

phone

(W) +41 21 69 35180 (M) +41 76 613 62 70

STRENGTHS

- ❖ PhD in Photonics at EPFL + Biomedical Engineer *cum laude*
- ❖ 4 years hands-on experience in complex optical systems, automation using Matlab and/or LabView
- ❖ Digital holography, interferometry, simulation of optical waves propagation
- ❖ Optical microscopy and endoscopy, wavefront shaping techniques

RESEARCH EXPERIENCE

- **PhD Candidate – Optical Scientist**

Jan 2013 - Present

École Polytechnique Fédérale de Lausanne, Optics Laboratory, Lausanne, Switzerland

Advisor: Prof. Demetri Psaltis

- Improved resolution and footprint size of optical fiber based endomicroscopes combining wavefront shaping and advanced imaging techniques (linear fluorescence, multi-photon fluorescence, photoacoustic imaging, SAX microscopy etc.).
- Complex optical setup design, interface and synchronization of different modules (Matlab and/or Labview), image acquisition and characterization of the optical setup performances, wavefront shaping using spatial light modulators, optical simulations using beam propagation method.

- **Optoelectronic R&D engineer** Jan 2012 - Dec 2012

Sapienza University, Electrical Engineering Department, Rome, Italy

Supervisor: Prof. Domenico Caputo

- Implementation on a single Lab-on-Chip device for electrowetting, microfluidics and optical sensing using amorphous silicon p-i-n photodiodes.

- **Master Thesis Intern** Jul 2011 - Dec 2011

INESC MN, Lisbon, Portugal

Advisors: Prof. Domenico Caputo, Prof. João Pedro Conde, Dr. Virginia Chu

- Theoretical study and microfabrication of a Lab-on-Chip to detect in vivo cellular intrinsic fluorescence.
- Fabrication and optoelectronic characterization of p-i-n amorphous silicon photodiodes and integrated optical filters.

- **Bachelor Thesis Intern** Jul 2009 - Dec 2009

Sapienza University, Computer and Control Engineering Department, Rome, Italy

Advisor: Prof. Daniela Iacoviello

- Working on a mathematical model to describe how influenza virus A spreads through a population over time.
- Developed optimal control for influenza A virus for SIRC epidemiological model.

EDUCATION

- **PhD – Photonics** Jan 2013 - Mar 2017

École Polytechnique Fédérale de Lausanne, Lausanne, Switzerland

Thesis: “Multimode fiber optical imaging using wavefront control”.

- **MSc cum laude – Biomedical Engineering** Jan 2010 - Jan 2012

Sapienza University, Rome, Italy

Thesis: “Cell-chips: integrated detection of intrinsic fluorescence”.

- **BSc – Clinical Engineering** Oct 2006 - Dec 2009

Sapienza University, Rome, Italy

Thesis: “Study on SIRC epidemiological model and control of Influenza A”.

TECHNICAL SKILLS

- **Optical systems design:** endoscopy, digital holography, interferometry, adaptive optics, wavefront shaping, spatial light modulators, beam propagation method.
- **High resolution microscopy:** two-photon microscopy, structured illumination microscopy.
- **Microfabrication and characterization:** photolithography, cleanrooms, wet and dry etching, soft lithography for microfluidic PDMS chips fabrication. Optoelectronic devices characterization.

LANGUAGE AND IT SKILLS

- **Languages:** *Italian* Mother tongue, *English* Excellent Proficiency (C1), *French* Extensive coursework, easily improvable (B1).
- **IT skills:** Matlab, Labview, Comsol, Illustrator, MS Office, Mac OSX.

AWARDS

- *Best Poster Award* at EPFL Photonics Day 2016 for the contribution "*Imaging and pattern projection through multicore fibers using the memory effect*," November 2016.

COMPLETE LIST OF PUBLICATIONS

- **Scientific journals**

- J1. **N. Stasio**, C. Moser, and D. Psaltis, "Calibration-free imaging through a multicore fiber using speckle scanning g microscopy," *Opt. Letters* **41**, 3078-3081 (2016).
- J2. D. B. Conkey*, **N. Stasio***, M. Romito, E.E. Morales-Delgado, C. Moser, and D. Psaltis, "Lensless two-photon imaging through a multi-core fiber with coherence-gated digital phase conjugation," *Journal of Biomedical Optics* **21**, 045002 (2016).
- J3. **N. Stasio**, D. B. Conkey, C. Moser, and D. Psaltis, "Light control in a multicore fiber using the memory effect," *Opt. Express* **23**, 30532 (2015).
- J4. **N. Stasio***, A. Shibukawa*, I. N. Papadopoulos, S. Farahi, O. Simandoux, J. P. Huignard, E. Bossy, C. Moser, and D. Psaltis, "Towards new applications using capillary waveguides," *Biomed. Opt. Express* **6**, 4619-4631 (2015).
- J5. G. P. J. Laporte*, **N. Stasio***, C. Moser, and D. Psaltis, "Enhanced resolution in a multimode fiber imaging system," *Opt. Express* **23**, 27484-27493 (2015).
- J6. O. Simandoux, **N. Stasio**, J. Gateau, J.-P. Huignard, C. Moser, D. Psaltis, and E. Bossy, "Optical-resolution photoacoustic imaging through thick tissue with a thin capillary as a dual optical-in acoustic-out waveguide," *Appl. Phys. Lett.* **106**, 094102 (2015).

- J7. G. P. J. Laporte*, **N. Stasio***, C. J. R. Sheppard, and D. Psaltis, "Resolution enhancement in nonlinear scanning microscopy through post-detection digital computation," *Optica* **1**, 455–460 (2014).
- J8. D. Iacoviello and **N. Stasio**, "Optimal control for SIRC epidemic outbreak," *Comput. Methods Programs Biomed.* **110**, 333–342 (2013).
- J9. A. Jóskowiak, **N. Stasio**, V. Chu, D. M. F. Prazeres, and J. P. Conde, "Integrated detection of intrinsic fluorophores in live microbial cells using an array of thin film amorphous silicon photodetectors," *Biosens. Bioelectron.* **36**, 242–249 (2012).

*Equally contributing

- **Invention disclosures**

- PI. E. Bossy, J.-P. Huignard, O. Simandoux, C. Moser, D. Psaltis, I. N. Papadopoulos, **N. Stasio** and S. Farahi "Minimally invasive optical photoacoustic endoscopy with a single waveguide for light and sound," US Patent 2016/0143542 A1, (May 26, 2016).

- **Conference papers and Proceedings**

- C1. **N. Stasio**, D. B. Conkey, C. Moser, and D. Psaltis, "The memory effect in multicore fibers," in *Imaging Systems and Applications*, Optical Society of America, (2016).
- C2. **N. Stasio**, A. Shibukawa, I. N. Papadopoulos, S. Farahi, O. Simandoux, J.-P. Huignard, E. Bossy, C. Moser, and D. Psaltis, "Fluorescence and optical-resolution photoacoustic imaging through a capillary waveguide," in *Adaptive Optics and Wavefront Control for Biological Systems II*, Proceeding of SPIE BIOS Photonics West, (2016).
- C3. **N. Stasio**, D. B. Conkey, C. Moser, and D. Psaltis, "Two-photon fluorescence imaging through multicore fiber with digital phase conjugation," in *Adaptive Optics and Wavefront Control for Biological Systems II*, Proceeding of SPIE BIOS Photonics West, (2016).
- C4. D. Caputo, G. de Cesare, A. D. Pastina, P. Romano, R. Scipinotti, **N. Stasio**, and A. Nascetti, "Thermally Actuated Microfluidic System for Polymerase Chain Reaction Applications," in *Sensors and Microsystems*, C. D. Natale, V. Ferrari, A. Ponzoni, G. Sberveglieri, and M. Ferrari, eds., Lecture Notes in Electrical Engineering No. 268 (Springer International Publishing), (2014)
- C5. D. Caputo, G. de Cesare, R. Scipinotti, **N. Stasio**, F. Costantini, C. Manetti, and A. Nascetti, "On-Chip Diagnosis of Celiac Disease by an Amorphous Silicon Chemiluminescence Detector," in *Sensors and Microsystems*, C. D. Natale, V. Ferrari, A. Ponzoni, G. Sberveglieri, and M. Ferrari, eds., Lecture Notes in Electrical Engineering No. 268 (Springer International Publishing), (2014)

- **Talks in international conferences**

- T1. **N. Stasio**, D. B. Conkey, C. Moser, and D. Psaltis, "The memory effect in multicore fibers," in *Imaging and Applied Optics*, Heidelberg - July 2016

- T2. **N. Stasio**, A. Shibukawa, I. N. Papadopoulos, S. Farahi, O. Simandoux, J.-P. Huignard, E. Bossy, C. Moser, and D. Psaltis, "Fluorescence and optical-resolution photoacoustic imaging through a capillary waveguide," in *Adaptive Optics and Wavefront Control for Biological Systems II*, SPIE BIOS Photonics West, San Francisco - February 2016
- T3. **N. Stasio**, D. B. Conkey, M. Romito, E.E. Morales-Delgado, C. Moser, and D. Psaltis, "Two-photon fluorescence imaging through multicore fiber with digital phase conjugation," in *Adaptive Optics and Wavefront Control for Biological Systems II*, SPIE BIOS Photonics West, San Francisco - February 2016
- T4. **N. Stasio**, A. Shibukawa, I. N. Papadopoulos, S. Farahi, O. Simandoux, J.-P. Huignard, E. Bossy, C. Moser, and D. Psaltis, "Multimodal imaging through a capillary waveguide using digital phase conjugation," in *Adaptive Optics and Wavefront Control in Microscopy and Ophthalmology*, Paris - October 2015

REFERENCES

Prof. Demetri Psaltis

Full Professor, Laboratory of Optics, EPFL

Dean of the School of Engineering, EPFL

email

demetri.pslatis@epfl.ch

address

EPFL STI IMT LO, BM4102, Station 17, 1015, Lausanne Switzerland

phone

(W) +41 21 69 37795